The Binary Rare Earth Oxides

Gin-ya Adachi* and Nobuhito Imanaka

Department of Applied Chemistry, Faculty of Engineering, Osaka University, 2-1 Yamadaoka, Suita, Osaka 565-0871 Japan

Received September 8, 1997 (Revised Manuscript Received February 18, 1998)

Contents

Gin-ya Adachi was born in Osaka, Japan, in 1938. He received his Bachelor degree in chemistry at Kobe University. He then obtained his M.E. (1964) and Ph.D. (1967) in Applied Chemistry from Osaka University. He then joined the faculty at Osaka University in 1967, where he is now Professor. He has broad interests in the domain of rare earth chemistry and materials and has been the recipient of The Shiokawa Award, The Rare Earth Society of Japan (1990), and The Award of The Chemical Society of Japan(1996). He is presently President of The Rare Earth Society of Japan.

Nobuhito Imanaka was born in Kawanishi, Hyogo, in 1958. He earned his B.E. (1981) and M.E. (1983) degrees in Applied Chemistry from Osaka University. He then obtained a Ph.D. degree from Osaka University in 1986. He has been a member of the the faculty at Osaka University since 1988. His main research fields include rare earths and functional materials such as solid electrolytes and chemical sensors. He received The Adachi Award, The Rare Earth Society of Japan (1996).

I. Introduction

Many review articles describing rare earth oxides have appeared up to 1990, and several intensive articles dealing with the properties such as preparation, structure and transformation were been published during the early 1990s, e.g., the preparation methods and the characterization of lanthanide oxides were reviewed by Eyring;[1] the structures and transformations of the rare earth oxides were published by Schweda;[2] thermodynamic properties were also re-

S0009-2665(94)00055-5 CCC: $30.00
Published on Web 04/28/1998

viewed by Morss.[3] In addition, a review of the "Seltenerdelemente" which appeared in *Gmelin Handbuch der Anorganischen Chemie*[4] is very useful. Recently, there has been much progress in the characterization of rare earth oxides from high-resolution electron microscopy (HREM), as well as in the preparation of ultrafine particles and in some aspects of theoretical calculation, especially for band structure. It is our purpose to introduce a comprehensive review of all these characteristics of binary rare earth oxides. In this review, R and Ln denote rare earths and lanthanoid, respectively.

Rare earth metals are, generally, very reactive with oxygen in the ambient atmosphere. Therefore, the most stable rare earth compounds are the oxides. It is known that the rare earth ions in rare earth oxides hold typically a trivalent state with the general formula, R_2O_3. However, some rare earths take a divalent or a tetravalent state, and in the case of Ce, Pr, and Tb, the intermediate phase also appears designated as R_nO_{2n-2m}. In this review, the polymorphism and the structure of the binary rare earth oxides are described together with additional information obtained at high pressure.

The in situ phase transformation among the R_nO_{2n-2m} phases is so complicated that it is quite difficult to define by the general elemental analytical methods. The HREM, which has been extensively utilized for the observation of the structure of the test sample in detail, was applied to clarify the phase transformation with the assistance of a video recording. Another recent advance in the research of binary rare earth oxides is the clarification of band structure of rare earth oxides by several calculation methods, and the development of sophisticated preparation techniques of ultrafine particles of the oxides. Both belong to a newly developed field in the binary rare earth oxides; the former gives us some insights for elucidating some other characteristics of the rare earth oxides and is greatly effective in identifying potentially new features of the oxides and the latter will contribute greatly to opening a door to the next stage of applications of rare earth oxides.

Typical characterizations of the oxides have been performed by measuring physical and chemical properties with electrical, magnetic, and optical techniques. These methods are also very useful in investigating the very small deviation in oxides from a stoichiometric ratio. Unusual characteristics are the ionic motion in the rare earth oxides. Oxide ions migrate in the oxides even at relatively low temperatures and this feature strongly influences the variation of the oxygen content in the oxides.

From the morphology point of view, a single crystal is an excellent form to use in the study of bulk characteristics of the oxide. However, the crystal growth of thermally unstable intermediate crystals and higher valent crystals is a very difficult task. Since the rare earth in the rare earth oxides can possess various valence states, a special technique is necessary to grow high-quality single crystals. In contrast, polycrystalline forms are predominantly used. Recently, much attention has been paid to the preparation of ultrafine particles. The fine particles exhibit unique features such as superplastic behavior for net shape forming, etc. The details of the preparation's progress in recent years are also mentioned in this article.

Thermodynamic properties are one of the most important features for the binary rare earth oxides. The most abundant products in the gas phase are rare earth monoxides with the polyatomic oxides approximately 2 or 3 orders of magnitude less abundant than monoxides. Therefore, the thermodynamic reports for the polyatomic oxides are very limited. Some data of the polyatomic oxides are also shown in addition to those of monoxides in this review.

II. Stability of Rare Earth Oxides

A. Oxidation of Rare Earth Metals

Rare earth metals react with oxygen vigorously and form oxides.[1] These oxides are thermally very stable and they are usually the final product when fired in the presence of oxygen. The final stoichiometry is closely dependent upon the temperatures and the oxygen pressure in the ambient atmosphere.[5,6]

As the oxygen pressure (P_{O_2}) increases in the range below about 10^{-100} atmospheres at 300 °C, the rare earth metals (including Sc and Y as well as lanthanoid) absorb oxygen successively until the solubility which is small but unknown in each metal, is satisfied. Except for europium, the sesquioxide forms first at an oxygen pressure between 10^{-100} and 10^{-80} atmospheres in the rare earth metals. If all of rare earth metals were left in the same atmosphere, the heavy rare earths with smaller ionic radius oxidize quickly from Lu to Dy, and the light members, such as Ce and Pr do so slowly. On the other hand, europium oxidizes initially to the NaCl-type monoxide and then to the spinel-type Eu_3O_4 at an oxygen pressure of 10^{-87} atm just before the sesquioxide is formed at an oxygen pressure, 10^{-86} atm. Pure Eu_3O_4 can be also obtained by the reaction described below.[7] Eu_3O_4 is prepared by reducing an equal molar mixture of Eu_2O_3, EuOCl, and LiH and then expels LiCl and H_2 at high temperatures. Another method to obtain Eu_3O_4 is to heat a mixture of EuO and Eu_2O_3 to 2050 °C in an iridium container and cool the system at the rate of 40 °C/h.[8] To prepare pure EuO, the reduction of the sequioxides in an excess of Eu metal is a recommended procedure.

For cerium, $Ce_{2.0}O_{3.0}$ would be formed at about 10^{-93} atmospheric pressure of oxygen. As the pressure is increased, $Ce_{2.0}O_{3.0}$ is oxidized to the homologous series Ce_nO_{2n-2m} in sequence until at approximately 10^{-40} atm, $CeO_{2.0}$ would begin to appear. After all the cerium is oxidized to $CeO_{2.0}$, the praseodymium sesquioxide starts to oxidize to $n = 7$, $m = 1(Pr_nO_{2n-2m})$ at 10^{-18} atm successively becoming $n = 9, 12, \infty$ at 10^{-10}, $10^{-3.8}$ and $10^{-0.76}$ atm, respectively. PrO_2 ($n = \infty$) is finally formed at 0.17 atm at 300 °C.

The praseodymium composition becomes almost $Pr_{40}O_{72}$ before the $Tb_{2.0}O_{3.0}$ starts to oxidize to Tb_7O_{12} at $10^{-9.6}$ atm. Tb_9O_{16} appears at $10^{-5.7}$ atm, but 10^3 atmospheric pressure is necessary to oxidize to the dioxide.

The recommended preparation method of the oxides for Ce, Pr, and Tb is by the decomposition of some compound precursor in air or in oxygen. $CeO_{2.0}$, Pr_6O_{11}, and approximately Tb_4O_7 are the compositions obtained in air. By decomposing terbium salts in air, the composition found is approximately Tb_4O_7. This is not a single phase but two-phase mixture of Tb_7O_{12} and $Tb_{11}O_{20}$. This is the origin of the almost universally incorrect statement in textbooks that Tb_4O_7 is believed to be a single-phased intermediate.

The most commonly used compounds are the oxalates and hydroxides. For example, pure cubic-La_2O_3 can be formed by the decomposition of lanthanum hydroxide or nitrate at a temperature in the range of 500−550 °C.[9] (A slight increase of either temperature or pressure brings a transformation from cubic to hexagonal A phase La_2O_3. A reversible C−B transformation occurs at a temperature of 800 °C for Gd_2O_3 to 2300 °C for Dy_2O_3. The detail of the A, B, and C phases are described in section III.C.2.a.)

In the case of rare earth dioxides, difficult-to-reduce $CeO_{2.0}$ is formed when its compounds are decomposed in oxygen at pressures in 10^{-3} atm range or higher. $PrO_{2.0}$ is formed slowly at temperatures around 300 °C and one atmosphere oxygen pressure, and more rapidly at higher temperatures and oxygen pressures. It requires oxygen pressures in the range of 1000 atm at 300 °C to form $TbO_{2.0}$. $PrO_{2.0}$ and $TbO_{2.0}$ can also be formed by disproportionation from the oxides obtained by the decomposition of precursors with O/Ln ratio between 1.5 and 2.0.

The high stability of the lanthanide oxides ensures that the metals are unstable in the presence of oxygen. The tarnishing of the metals is facile, in most cases with a rapid rate with satisfying a parabolic rate law during the formation of an oxide film. The composition of the oxide layer during the reaction is exactly dependent on the type and purity of the element involved in the oxide and the conditions of the measurements. A few scattered experiments have been done on the reaction of rare earth metals with oxygen. Some of these have considered determining the rate law, which is parabolic in the early stages of reaction and in nearly all cases is regarded as being from the diffusion of oxygen through the oxide film of increasing thickness.

B. Reactivity of Rare Earth Oxides

The rare earth sesquioxides become hydrated and carbonated if they are exposed to atmospheric carbon dioxide and water vapor at ambient temperature and pressure. Even in the case of the heaviest members of the oxides, this behavior can be observed. Oxides that belong to group I (La_2O_3, Nd_2O_3, and some Sm_2O_3), corresponding to the lighter rare earth series, transform partially to carbonated hydroxides. In contrast to the hydration, the carbonation process is limited to the outer layers of the oxides. For the sesquioxides of group II (some Sm_2O_3, Eu_2O_3), holding the cubic phase, the transformation is only partial. In the case of the heaviest sesquioxides, group III (Dy_2O_3, Ho_2O_3, Yb_2O_3), the transformation of the oxides is also only fractional. The reaction behavior of the rare earth oxides was systematically investigated in detail by X-ray powder diffraction, IR, thermogravimetry, and temperature-programmed decomposition methods by Bernal et al.[10]

With long exposure to air, higher oxides (i.e., Pr_6O_{11}) of praseodymium react and form $PrO_{2.0}$ and $Pr(OH)_3$. The reaction proceeds slowly at 20 °C and rapidly at 100 °C. (For the terbium oxides, the temperature required is 200 °C.) The pure dioxides of $PrO_{2.0}$ and $TbO_{2.0}$ can be obtained by treatment of the reacted products with suitable acids, such as acetic acid.[11] Subsequently, the disproportionation has been shown to occur commonly in both the praseodymium and terbium higher oxides.[11−13] The intermediate oxides have been found to be soluble in solvents such as acetic acid, to form trivalent metal ions into solution. Similar reactions have been known to occur in the case of the formation of PbO_2 from Pb_3O_4 or MnO_2 from Mn_2O_3 by leaching PbO and MnO, respectively, into the diluted nitric acid. By treatment with 10% acetic acid, the leaching out of $Pr(OH)_3$ occurs which results in leaving only $PrO_{2.0}$. $PrO_{2.0}$ crystals appear where no more $Pr(OH)_3$ is present. As the original Pr^{4+} ions are dispersed atomically in the crystals, the use atomic resolution electron microscopy is very useful in investigating the reaction relationships. The electron microscope clarifies the actual process of the reaction an imaging method, that is, easy reaction paths exist in the crystal and the paths are almost certainly dislocated. The $PrO_{2.0}$ formation reaction from Pr_7O_{12} could also occur with any of the intermediate ordered oxides between $Pr_{2.0}O_{3.0}$ and $PrO_{2.0}$.

C. Melting Points

The melting points of the sesquioxides are shown in Figure 1.[14] The solidification temperature has been determined by Coutures et al.[14] The list of freezing and boiling points of the lanthanide sesquioxides are also tabulated in Table 1.[15] In the relation between the solidification point and the atomic number of the corresponding lanthanoid element, an

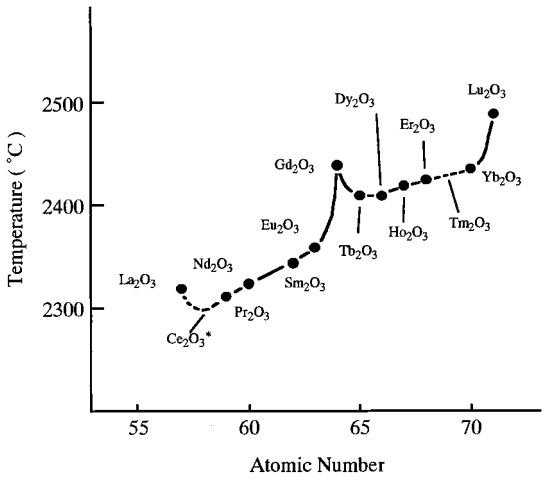

Figure 1. The relation between the solidification point and the atomic number of lanthanoid sesquioxides. Ce_2O_3 which is a nonstoichiometric oxide such as $CeO_{1.53-1.50}$, is designated as Ce_2O_3*. (Reproduced with permission from ref 14. Copyright 1975 Revue Internationale des Hautes Temperatures et des Refractaires.)

Table 1. The Freezing and Boiling Points of the Lanthanoid Sesquioxides[a] (Reprinted with permission from ref 15. Copyright 1994 Elsevier Science B. V.)

lanthanoid oxide	freezing point (°C)	boiling point (°C)
La_2O_3	2256	3620
	2304 ± 5	
Ce_2O_3*	2210 ± 10	3730
Pr_2O_3	2183	3760
Nd_2O_3	2233	3760
Pm_2O_3	2320	
Sm_2O_3	2269	3780
Eu_2O_3	2291	3790
Gd_2O_3	2339	3900
Tb_2O_3	2303	
Dy_2O_3	2228	3900
Ho_2O_3	2330	3900
Er_2O_3	2344	3920
Tm_2O_3	2341	3945
Yb_2O_3	2355	4070
Lu_2O_3	2427	3980

[a] Ce_2O_3 which is a nonstoichiometric oxide such as $CeO_{1.53-1.50}$, is designated as Ce_2O_3*.

anomaly for the gadolinium sesquioxide was observed. This curve is divided into two groups: The first one (ceric group) is from La_2O_3 to Gd_2O_3 with an increasing of the solidification point. The second one is yttric group in which the temperature of solidification also rises from Dy_2O_3 to the end of the family of Lu_2O_3. The typical explanation for the Gd_2O_3 anomaly is ascribed to the result of the Gd^{3+} electronic state with the half-filled 4f subshell ($4f^7$).

All the sesquioxides transform to high-temperature forms (two phases in some cases) above 2000 °C, irrespective of atomic size. All the sesquioxides melt in the range from 2300 to 2500 °C. (See Figure 1.)

Generally, the effect of the melting atmosphere on the refractory character of the sesquioxides is poor. But the exception is for praseodymium and cerium oxide, where a reducing condition is required, and small amounts of oxygen give a decrease in the solidification temperature. For Eu_2O_3, an oxidizing condition is necessary.

III. Structural Properties of Rare Earth Oxides

A. General Aspects of Rare Earth Oxide Series

At moderate temperatures, any compound of oxygen with rare earth is a solid. The solid-state chemistry of individual atoms in combination with oxygen is primarily dependent upon its electronic configuration and ionic size. In the lanthanoid series of elements, the increasing nuclear charge, as electrons are added to the 4f orbitals, is effectively shielded by the outer $5d^1$ and $6s^2$ valence electrons. This makes the valency hold favorably in a trivalent state for all the lanthanides whose energy varies gradually across the series. The ionic size of the rare earth atom in combination with oxygen to form oxides contracts smoothly across the series. Figure 2 presents the principle of this main sequence of the oxides.[6]

The data are cited from Eyring and Holmberg,[16] Templeton and Dauben,[17] Barbezat and Loriers,[18] and Stecura and Campbell.[19] Templeton and Dauben

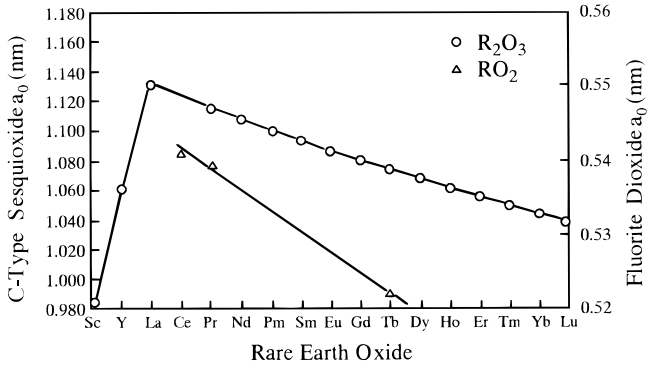

Figure 2. Lattice parameter for the cubic rare earth oxides. (Reproduced with permission from ref 6. Copyright 1979 North-Holland Publishing Company.)

obtained the data from Sm_2O_3 to Lu_2O_3 for the oxides with mineral bixbyite. The data were for the oxides whose purity is higher than 99.9%. Barbezat and Loriers reported the data for La_2O_3 and $Pr_{2.0}O_{3.0}$.

From the combination of electronic configuration and the size of the lanthanoid atoms, their oxides become the most thermally stable of all known substances. However, the nature of the chemical bond changes over each series. It has been reported that there is a considerable degree of covalency with the predominant ionic character.[20−23]

Although electrons in the f orbitals are not strongly concerned with the formation of compounds, they definitely have a second-order effect on the chemical properties. They facilitate the valence state change other than three which appear in, for instance, divalent samarium, europium, and ytterbium, and tetravalent cerium, praseodymium, and terbium. As Hund observed, near the zero, half, and completely filled f condition, the energy of the f electronic states changes considerably.

The presence of widely varying numbers of unpaired electron spins is caused by the filling of the f orbitals according to Hund's rule, and as a result the oxides possess progressive and varied magnetic properties. Indeed, the proving ground for the elaboration of the theory of magnetism is obtained from the lanthanide elements and their compounds.

B. Lattice Parameters of the Sesquioxides

The lattice parameters for each of sesquioxides are listed in Table 2[1] which are derived from *Gmelin Handbuch*.[4] (Besides the original publications cited in this review, the review article of the *Gmelin Handbuch der Anorganischen Chemie* has been very useful.)

Three of the lanthanides, Ce, Pr, and Tb also hold higher oxides. The most oxidized phase is the dioxide with a fluorite structure, namely $CeO_{2.0}$, $PrO_{2.0}$, and $TbO_{2.0}$. The phases between Ln_2O_3 and $LnO_{2.0}$ are oxygen-deficient and fluorite-related. At lower temperatures, ordered intermediate phases of narrow composition range most of which can be described as Ln_nO_{2n-2m}, where $4(Ln_2O_3) < n < \infty(LnO_{2.0})$ and $1 < m < 8$, exist. In contrast, wide composition ranges, LnO_x ($1.50 < x < 1.70$) for σ phase and LnO_x ($1.72 < x < 2.00$) for α phase are stable at higher temperatures.

Table 2. Lattice Parameter of the Rare Earth Sesquioxides[a] (Reprinted with permission from ref 1. Copyright 1991 Kluwer Academic Publishers)

A-type oxide	*a* (nm)	*c* (nm)	A-type oxide	*a* (nm)	*c* (nm)
La_2O_3	0.39372	0.61295	Nd_2O_3	0.38293	0.59970
Ce_2O_3	0.389	0.607	Pm_2O_3	0.3802	0.5954
Pr_2O_3	0.3857	0.6016			

B-type oxide	*a* (nm)	*b* (nm)	*c* (nm)	*β*
Pm_2O_3	1.425	0.366	0.893	100°31′
Sm_2O_3	1.418 ± 0.001	0.3636 ± 0.0003	0.8841 ± 0.0008	99.92° ± 0.05°
Eu_2O_3	1.4110 ± 0.0007	0.3603 ± 0.0001	0.8805 ± 0.0004	100.05 ° ± 0.05°
Gd_2O_3	1.4061 ± 0.0013	0.3566 ± 0.0006	0.8760 ± 0.0007	100.10 ° ± 0.08°
Tb_2O_3	1.404 ± 0.001	0.3541 ± 0.0003	0.8725 ± 0.0008	100.06° ± 0.05°
Dy_2O_3	1.397 ± 0.001	0.3519 ± 0.0003	0.8661 ± 0.0008	100.00° ± 0.05°
Ho_2O_3	1.390 ± 0.001	0.3492 ± 0.0003	0.8592 ± 0.0008	99.98° ± 0.05°
Er_2O_3	1.387 ± 0.001	0.3470 ± 0.0003	0.8555 ± 0.0008	100.17° ± 0.05°
Tm_2O_3	1.381 ± 0.001	0.3447 ± 0.0003	0.8505 ± 0.0008	100.20° ± 0.05°
Yb_2O_3	1.373 ± 0.001	0.3425 ± 0.0003	0.8452 ± 0.0008	100.17° ± 0.05°
Lu_2O_3	1.370 ± 0.001	0.3410 ± 0.0003	0.8425 ± 0.0008	100.22° ± 0.05°

C-type oxide	*a* (nm)	C-type oxide	*a* (nm)	C-type oxide	*a* (nm)
La_2O_3	1.136 ± 0.002	Sm_2O_3	1.0932 ± 0.0009	Ho_2O_3	1.0607 ± 0.0005
Ce_2O_3*	1.116	Eu_2O_3	1.0866 ± 0.0005	Er_2O_3	1.0547 ± 0.0003
Pr_2O_3	1.1152 ± 0.0002	Gd_2O_3	1.0813 ± 0.0005	Tm_2O_3	1.0488 ± 0.0006
Nd_2O_3	1.1077	Tb_2O_3	1.0730 ± 0.0001	Yb_2O_3	1.0439 ± 0.0007
Pm_2O_3	1.099 ± 0.001	Dy_2O_3	1.0667 ± 0.0006	Lu_2O_3	1.0391 ± 0.0005

[a] Ce_2O_3 which is a nonstoichiometric oxide such as $CeO_{1.53-1.50}$, is designated as Ce_2O_3*.

The conditions for adjusting the composition of single crystals depend on the crystallite size and whether equilibrium has been attained or not. It is essential for both powder and crystal samples to confirm the composition by a weighing method and X-ray analysis. The variation is small in the ordered regions, while it is large in the high temperature α and *σ* regions.

C. Stable Phases in the Rare Earth Oxides and Their Structures

1. The Lower Oxides

The monoxides, LnO, can be obtained in the gas phase at high temperatures under vacuum for all members of the series.[1] A summary of thermodynamic properties and vaporization characteristics are described in the previous review.[3] At low temperatures, an NaCl-type solid LnO phase is thermodynamically stable. EuO exists as apparently does YbO. Both EuO and YbO crystallize in the NaCl-type structure. The stability of divalent ytterbium is lower than that of europium and the preparation of condensed ytterbium monoxide seems to be unfavored by a high-temperature technique.[24] From calculations based on the third law of thermodynamics, it is shown that a lower oxide of ytterbium might become stable when prepared at low temperatures. At elevated temperatures, YbO is not stable and dispropornates to the metal and sesquioxide.[25]

LnO has been prepared by the high-pressure reaction of the lanthanoid metals with the corresponding sesquioxides. Mixtures were heated in the temperature range 500−1200 °C at (1.5−8.0) × 10^4 atm. The monoxides of La, Ce, Pr, Nd, and Sm are obtained in the NaCl form with a golden yellow metallic luster. The lanthanoid ion is generally in a trivalent state, while the lanthanide in EuO and YbO is in the divalent state. Samarium monoxide shows metallic behavior with the intermediate valency state of Sm close to three.[26]

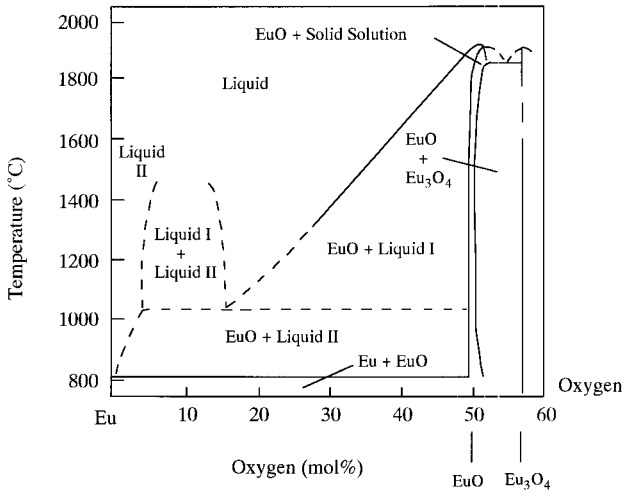

Figure 3. A phase diagram in the Eu−Eu_3O_4 region. (Reproduced with permission from ref 27. Copyright 1972 Pergamon Press.)

In the rare earth monoxides, EuO is well-established. Its preparation and the range of phase stability is described by Shafer et al.,[27] and its properties are described in the review.[28] From the phase diagram[27] as shown in Figure 3, EuO does not melt congruently. Here, more than 30 single crystals grown under various conditions, and many quenched samples were analyzed to obtain the phase diagram. The phase boundary between the EuO phase and the liquid plus crystal region changes with temperature and the liquidus curve between EuO and Eu metal has been precisely determined. Several important features obtained are as follows:

1. Stoichiometric EuO does not exist at high temperatures.

2. In the EuO phase, appreciable composition variation was recognized.

3. EuO single crystals can be obtained from the liquid phase at temperatures lower than that thought earlier to be possible.

4. By selecting the appropriate growth temperature, the stoichiometry of EuO can be controlled.

The maximum melting point is obtained at 1965 ± 10 °C for the oxygen-rich region. In the region for temperatures higher than 1800 °C, the Eu−O phase becomes oxygen rich. In this case, trivalent europium and also europium vacancies in the crystal samples were obtained. At temperatures lower than around 1965 °C, europium loss becomes less in the EuO phase. The liquid−stoichiometric EuO equilibrium exists at around 1825 °C. The eutectic temperature between Eu metal and EuO is ca. 825 ± 3 °C and this temperature is almost the same as the melting temperature (826 °C) of Eu metal. This means that the decrease of the freezing temperature is negligible when europium monoxide exists with Eu metal. The crystals obtained at lower temperatures are rich in europium content with the additional formation of oxygen vacancies.[27]

Eu_3O_4 is orthorhombic[29,30] with space group *Pnam*. The coordination is 6-fold for oxygens around the trivalent europium ion, forming a distorted octahedron around each Eu^{3+} ion. The coordination is 8-fold around the divalent europium ion and each Eu^{2+} ion exists at the center of a triangular prism of six oxygen atoms. Two oxygen atoms complete the coordination by lying out from the centers of two of the prism faces. A discussion of the lower oxide preparation has been reported by Brauer[9] and by McCarthy and White.[31] Bedford and Catalano[8] have shown that both EuO and Eu_3O_4 have a very narrow composition limit. EuO is a red compound, and Eu_3O_4, a black compound. Corresponding monoxides of Sm and other lanthanide elements have been reported to contain probably nitrogen or some other stabilizing impurity.[32]

The investigation of EuO has been studied extensively, since EuO has a potential for use in electronic devices. The highest purity of EuO samples can be obtained by adding approximately 5% less than the theoretical oxygen amount and distilling off any slight excess of europium metal. The second new method to prepare EuO is to precipitate the hydroxide $Eu(OH)_2 \cdot H_2O$ from an aqueous Eu^{2+} containing solution and to decompose this compound at 450 °C in a high vacuum.[9] The stability ranges of the established europium oxides are shown in Figure 4 where the logarithm of the fugacity of oxygen is shown against temperature.[31] By choosing the suitable temperature and oxygen pressure, it can be easily understood that any of the europium oxides can be obtained. EuO crystals can be classified into five categories (Figure 5).[27] The temperature of 1355 °C is significant since it is the lowest temperature where EuO and liquid oxide can be in equilibrium with europium vapor at its own pressure. From the figure, the stoichiometry in Eu−O crystals is determined by the temperature at which the EuO crystallizes. The phase boundary between the EuO phase

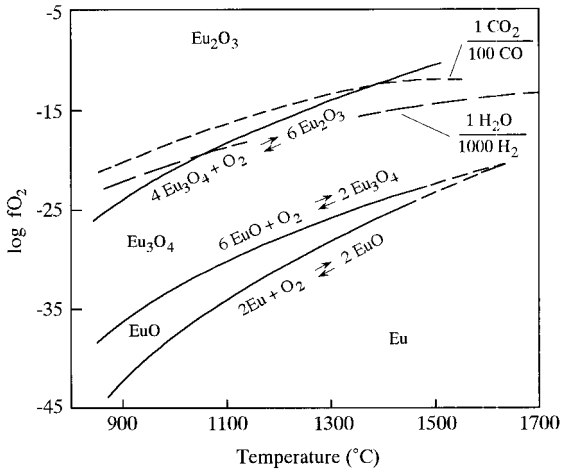

Figure 4. Conditions for interactions of the lower oxides of europium. (Reproduced with permission from ref 31. Copyright 1970 Elsevier Sequoia S. A.)

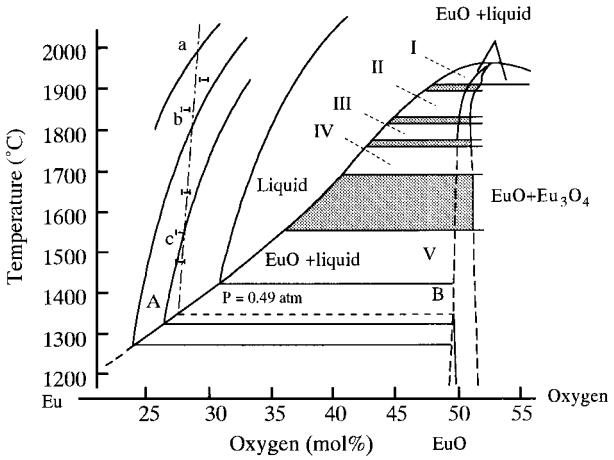

Figure 5. The EuO region of the Eu−O phase diagram. (Reproduced with permission from ref 27. Copyright 1972 Pergamon Press.)

and the liquid plus crystal region varies with temperature and, in addition, the liquidus curve between EuO and Eu metal was determined. The error limits on the liquidus curve in Figure 5 is within 15 °C. From the analyses of more than 30 single crystals, which were grown under different condition and many quenched samples as described in section III.C.1, it was also possible to construct the phase diagram of Figure 5.

Detailed correlations have been made between crystals grown from various regions of the diagram and their physical properties. A summary of the characteristic properties of typical crystals grown from each of the five regions are listed in Table 3.[27]

Region I: Crystals grown between the EuO melting point (1965 °C) and approximately 1890 °C is classified as region I. No single crystal was successfully grown, since the EuO phase crystallizing from this region is deficient by several percent in Eu content.

Region II: Single crystals were grown and single phase successfully quenched. The existence of Eu^{3+} is identified from IR absorption spectra.

Region III: This is the region where stoichiometric EuO is grown. This is the area where crystals grown from one particular region near a boundary of an

Table 3. Physical Properties of EuO Crystals (Reprinted with permission from ref 27. Copyright 1972 Pergamon Press)

class or growth region	initial composition mol% oxygen	crystallization temp (°C)	conductivity	characterization IR	stoichiometry
I	50−47	>1890	insulating, 0.45−0.75 eV activation energy	shows spectrum of Eu_3O_4	contains Eu_3O_4 as second phase
II	47−44	1825−1890	insulating, 0.45−0.7 eV activation energy	Eu^{3+} absorption lines	single phase EuO with Eu vacancy
III	44−42	1780−1825		low absorption $\alpha < 3\ cm^{-1}$	stoichiometric EuO
IV	42−35	1680−1780	insulator−metal transitions, 0.3 eV activation energy	oxygen vacancy absorption	contains oxygen vacancies
V	<35	below ~1680	metallic conductivity	free carrier absorption	many oxygen vacancies

adjacent region is not the same with those of typical crystals grown from the region. Therefore, it is impossible to define the boundaries between adjacent regions precisely, and hence they are shown as wide gray areas in Figure 5.

Region IV: The EuO composition becomes Eu rich when the crystallization temperature is below around 1780 °C. The phase field expands to the Eu-rich side of the stoichiometric composition in Figure 5.

Region V: Region V is defined as the temperature decreases below 1600 °C. There is no abrupt difference in composition between regions IV and V and only by a continuous increase in the number of oxygen vacancies.

No significant variation was observed in the lattice constant of all five regions. The lattice constant variation was smaller than 0.1 pm going from oxygen-rich to stoichiometric to Eu-rich range. Physical properties such as IR and electrical conductivity measurements and Curie temperature are mentioned in detail by Shafer.[27]

Under YAG laser ablation and under ultrahigh vacuum (UHV) conditions, oxygen is preferentially vaporized because the lightest element is the one which vaporizes at first. The phenomenon becomes more intense with the increase of the number of laser shots. The diffusion observed above seems to be directly related to the nonstoichiometry in yttrium sesquioxide.

By heating under a vacuum of 10^{-8} or 10^{-9} atm, the transition of the cubic phase into a cubic phase of the same space group with larger cell parameters than the C phase appears at 1670 K, then at 1870 K into the monoclinic phase of $YO_{1.495}$, at 1970 K into the monoclinic phase of $YO_{1.455}$ and finally into the hexagonal phase of $YO_{1.335}$ at 2170 K.[33] Almost the same results are also reported by Husson and Proust.[34]

2. The Sesquioxides

a. Polymorphism. All the rare earth elements form a sesquioxide. In the polymorphism, five distinct crystalline types have been identified. At temperatures lower than approximately 2000 °C, three types designated as A, B, and C are commonly found. In the temperatures above 2000 °C, the types designated as H or X are formed.[35,36] The crystal chemistry of the rare earth sesquioxides was first studied in a systematic manner by Goldschmidt et al.[37]

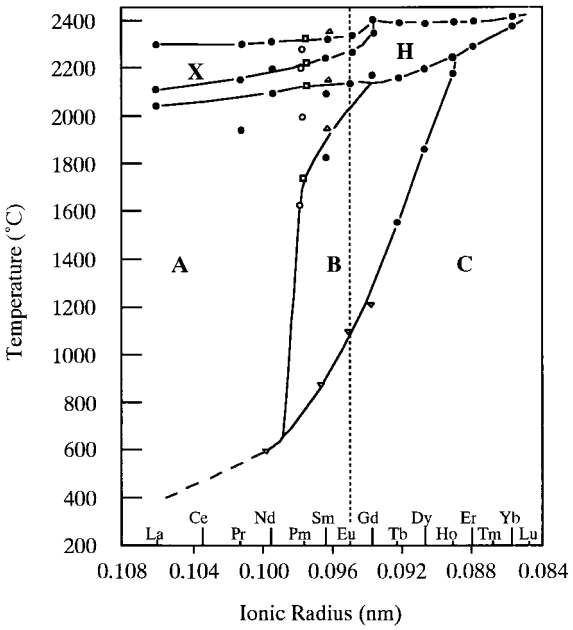

Figure 6. Polymorphic transformation for the lanthanoid sesquioxides. (Reproduced with permission from ref 35. Copyright 1966 Revue Internationale des Hautes Temperatures et des Refractaires.)

Figure 6[35] presents the temperature ranges of stability of the five polymorphic forms. Only in the middle range of ionic radius can all five polymorphic phases be formed by each oxide. With increasing temperature, the order of transition is C → B → A for these rare earth oxides. C-type Eu_2O_3, for example, transforms to the B form at about 1100 °C and then to the A form at ~2040 °C. By further heating, the A form transforms to the H form at about 2140 °C and then finally to the X form at about 2280 °C just below the melting point at ~2340 °C. The C to B transition has also been directly observed by X-ray diffraction in the case of Eu_2O_3.[38] By grinding on an abrasive paper, the transformation occurred on the surfaces of the pellets of cubic phase Eu_2O_3. The observed polymorphic transition seems to be caused by the localized temperature transients and stresses caused by grinding. Therefore, great care should be taken when preparing a powder or surface for X-ray diffraction by grinding or abrasion. For the lighter rare earth oxides from

La_2O_3 to Nd_2O_3, the C form oxide might be metastable.

Weigel and Scherer[39] detected promethium sesquioxide, Pm_2O_3. This is the first case where all the three polymorphs, A, B, and C, of a single-phase oxide were prepared and then studied at room temperature. Coral red C-type Pm_2O_3 was obtained when promethium(III) oxalate decahydrate was ignited in a vacuum at temperatures from 600 to 950 °C. Its lattice constant is cubic $a = 1.099$ nm and its density has been calculated to be 6.84 g cm^{-3}. Purplish pink B-type Pm_2O_3 has been formed when the oxalate decahydrate was pyrolized in air at temperatures higher than 950 °C. Its monoclinic lattice constants are $a = 1.425$ nm, $b = 0.366$ nm, $c = 0.893$ nm, $\beta = 100.50°$. The density calculated from these data is 7.43 g cm^{-3}. Deep lavender A-type Pm_2O_3 could be also synthesized by igniting freshly precipitated and dried $Pm(OH)_3$ using a platinum or alumina crucible in air or in an argon atmosphere for several hours above 1600 °C. The lattice constants of the hexagonal phase are $a = 0.3802$ nm and $c = 0.5954$ nm and the calculated density is 7.62 g cm^{-3}. With increasing temperature, the range of stable existence changes in the sequence C → B → A in these three modifications. The density monotonically increases with the C → B → A transformations.

As the A form transforms to H, an abrupt decrease in the c/a ratio is observed as does the density. Both a and c increase sharply but the lattice a increase is more rapid, and reduces the ratio c/a. The temperature region of stability of each polymorph except the C form becomes narrower as radius of the rare earth decreases. Finally lutetium (and scandium) directly makes a transition from C-type solid to the molten state.

b. Structure of the Sesquioxides. Studies of polymorphism have yielded markedly varying results over the years. There have been difficulties in preparing high-quality starting materials, their occasionally having adsorbed water or purity differences in the parent rare earths and sometimes errors in the identification of a product.

The A form of hexagonal sesquioxides is of space group $P32/m$ with one formula per unit cell.[40,41] The metal atoms are in a seven coordination[16] with four oxygens closer than the other three. The four oxygens are bonded to five metals and the other three to four metal atoms. The A-type structure has been found from La_2O_3 to Nd_2O_3.[42,43]

The B form sesquioxide is a monoclinic distortion of the A form. The B-type sesquioxide has the space group $C2/m$ with six formulas units per cell.[44,45] The metal atoms in the B-type polymorph are seven- and six-coordinate.

The C form structure is of the cubic bixbyite type, cubic space group, $Ia3$, containing 32 metal atoms and 48 oxygen atoms per unit cell[46] related to a doubled-edge fluorite structure with one-forth of the oxygen sites vacant and regularly ordered. Bixbyite is the mineral of $(Fe,Mn)_2O_3$. The metal atoms are six-coordinate. The C-type La sesquioxide has not been reported and that of Ce is not well-known. The

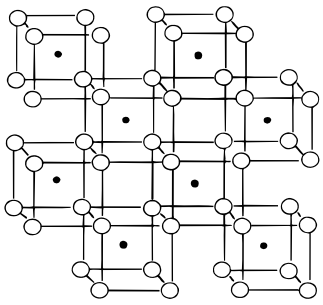

Figure 7. Representative of fluorite-type RO_2. The solid dots indicate the metal atoms. (Reproduced with permission from ref 6. Copyright 1979 North-Holland Publishing Company.)

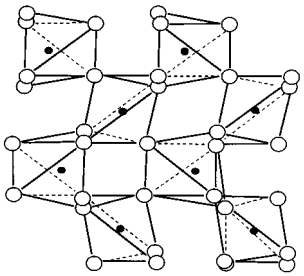

Figure 8. Representative of C-type R_2O_3. The solid dots indicate the metal atoms. (Reproduced with permission from ref 6. Copyright 1979 North-Holland Publishing Company.)

C-type Sm oxide is stable at low-temperature and at ordinary pressures. For the oxides above Tb, the C type is the most stable at all temperature for ordinary pressures. Both A and C forms of Pr are well-established. For Nd, the A type is the most common but the C type has also been appeared. The intermediate member of the series can be obtained in any of the three forms. (See the reference by Boulesteix[47] for a detailed description of the stabilities and transformations in these three types.)

To consider the relationships between the RO_2 dioxide on one hand and the A, B and C form sesquioxides on the other is very beneficial.[16] In the dioxide, the metal atoms are eight-coordinate with cubic coordination polyhedra sharing all edges to form a three-dimensional network (Figure 7[6]). In the case where one-fourth of the oxygen atoms of this network are removed along nonintersecting strings in the four ⟨111⟩ directions, this results in the situation where every atom is six-coordinate, and the C type is obtained. In this case, one-fourth of the atoms have oxygens missing across the body-diagonal and three-fourths have oxygens missing across the face-diagonal (Figure 8[6]).

On the other hand, if the oxygen substructure of the fluorite RO_2 is preserved completely and the metal atoms are moved into interstitial sites in such a manner that slabs of RO_2 two atom-layers wide are sustained, shearing occurs at these regular intervals and the A type with seven-coordination is formed (Figure 9[6]). The B form is very alike to the A type with six- and seven-coordination (Figure 10[6]).

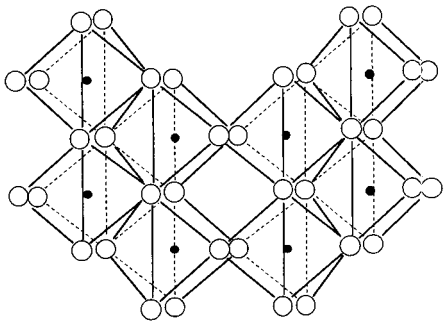

Figure 9. Representative of A-type R_2O_3. The solid dots indicate the metal atoms. (Reproduced with permission from ref 6. Copyright 1979 North-Holland Publishing Company.)

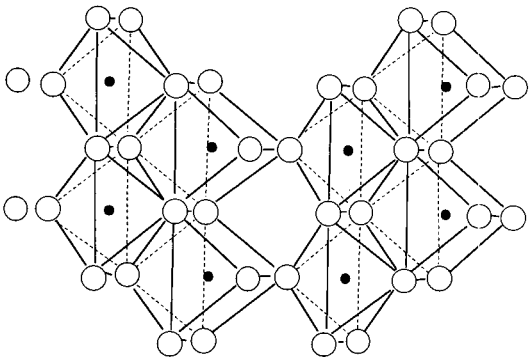

Figure 10. Representative of B-type R_2O_3. The solid dots indicate the metal atoms. (Reproduced with permission from ref 6. Copyright 1979 North-Holland Publishing Company.)

3. Intermediate Oxides

The composition of the sesquioxide phase is closely related to the polymorphic form and its chemical environment. Among the three forms of the sesquioxides obtained at low temperatures, the C type is most likely to vary in composition. Partially reduced C-type rare earth oxides were produced by codistilling and comelting the sesquioxides with their respective metals, and the composition of the separated oxide phase was determined by reoxidation to the sesquioxide.[48] For example, the compositions observed were $GdO_{1.495}$, $YO_{1.491}$, $ErO_{1.489}$, and $LuO_{1.485}$. From the density and X-ray diffraction studies, these oxides were found to be nonstoichiometric by loss of oxygen from normal oxygen sites. The oxides are deeply colored presumably as a result of the function of the oxygen vacancies as trapping sites. The vacancies are Schottky defects in the anion lattice. These defects function as effective positive ion sites and they can trap the electrons released at the time the oxide ion leaves from the surface as neutral oxygen. At high temperatures in the presence of Yb metal, oxygen loss from Yb_2O_3 was observed to yield $YbO_{1.495}$. The reduced sesquioxide apparently disproportionates to Yb + $YbO_{1.50}$ when it is cooled below 1800 °C. A variable composition in the $EuO_{1.5}$ phase down to $EuO_{1.45}$ was also reported at 1500 °C.[8]

In the rare earths series, the sesquioxide is well-known. Of the sesquioxides, least is known about Ce_2O_3. Unless it is completely stoichiometric with the A form, it can be pyrophoric and preparation under anaerobic conditions is essential. However, "Ce_2O_3" has been reported to be prepared.[49] The "Ce_2O_3" is a nonstoichiometric $CeO_{1.53-1.50}$ phase and hereafter such a cerium oxide is designated as Ce_2O_3*. By the reduction, the color becomes dark. $CeO_{2.0}$ was found to start reducing appreciably at temperatures higher than 600 °C in hydrogen. In the process of reduction, lattice parameters of the intermediate phase increased gradually up to the C type by a maximum of 2.7%.

The thermal expansion of Ce_2O_3* was found to be linear and no discontinuity induced by the phase transformation appeared. The experimentally determined linear expansion coefficient was 1.2×10^{-5} deg^{-1} at room temperature and 1.48×10^{-5} deg^{-1} at 1350 °C.[50] Ce_2O_3* is very unstable and oxidizes to cerium dioxide even at room temperature in air. The oxidation process is a very exothermic process and spontaneous ignition often occurs. The melting point of Ce_2O_3* is ~2210 °C, which is similar to the values of other rare earth oxides (see Figure 1). Ce_2O_3* is stable until the melting point without decomposition in a hydrogen atmosphere. CeO_3 decomposes only slowly; CeO_4 is explosively unstable. Cerium dioxide can be reduced only with a great difficulty. The reduced oxides are pyrophoric and react spontaneously and vigorously with air at room temperature. As a result, the dioxide is again formed. Ce_2O_3* can be obtained after reducing CeO_2* in H_2 at 1000 °C.[51] The CeO_2* hereafter indicates the CeO_2 in which the O/Ce ratio seems to be almost 2 but not identical to 2.0. A yellowish olive color of Ce_2O_3* is obtained by a reaction time of 85 h. The color is highly dependent upon the stoichiometry and impurities. Pure stoichiometric $Ce_{2.0}O_{3.0}$ is believed to be white. C-type Ce_2O_3* can appear on the surface of Ce metal left at room temperature in air for a only few hours.[18]

The intermediate oxides have oxygen-deficient, fluorite-related structures.[15] Ce, Pr, and Tb form intermediate compounds in narrow composition ranges with the generic formula Ln_nO_{2n-2m} (n is an integer or infinity and m is between 1 and 8). Among the cerium oxides, only the iota (ι) phase ($n = 7$, $m = 1$) structure has been determined,[52] although it is likely that the structure of the $n = 11$ phase is isostructural with $Tb_{11}O_{20}$. More structures have been determined in the praseodymium−oxygen system than in the other two.

The phase diagram of the higher-oxide phase relationships and particularly those of the cerium−oxygen system was clarified by Ricken et al.[53] and by Riess et al.[54] by the method of heat capacity measurement and confirmed by Körner et al.[55] from thermal expansion measurements. The detail of the phase diagram for Ce−O system is described in section III.C.5.b. Two of the intermediate phases belonging to the homologous series, $Ce_{19}O_{34}$ ($n = 19$, $m = 2$) and $Ce_{62}O_{112}$ ($n = 62$, $m = 6$), were observed independently from HREM observations by Knappe and Eyring[56] and HREM is a useful tool to study in an atomic level in situ researches.[57,58] More work must be done on $n = 9$ in order to map out its obvious

complexity. One striking feature is that the CeO_x intermediate phases are structurally much more similar to the TbO_x system than that of PrO_x which should have more closely the same metal−nonmetal radius ratio. The subvalence electron orbital configuration of Ce and Tb, each with one electron beyond the empty or one-half-filled f orbitals, is at least as important as the radius ratio in determining the structure of these intermediate phases.

4. Pressure Effects on Polymorphism

Pressure effects on the polymorphism of the sesquioxides have been also studied.[59−61] Each of the polymorphilic forms is composed of either a single type of coordination polyhedron (e.g., RO_6 in the cubic C type and RO_7 in the hexagonal A form) or from a mixture of RO_6 and RO_7 polyhedra as in the case in the monoclinic B form. The variation of the molar volumes of the polymorphs suggests a profound pressure dependence on the stability regions. It is very easy to speculate that high pressure should result in a preference to the A form in favor of the B form, and the A and B forms in favor of the C form. In reality, the A and B forms, would be stabilized with respect to the C form.[59−61] For example, at the pressures higher than 3.5×10^4 atm and at 1000 °C, the B form is the preferential phase for all the C-type rare earth from Sm to Lu and Y. Similar behavior also appears in the B → A transition but the effect is much less defined than that observed in the case for the B−C transition. The densities of these three type are appreciably different, with the order $\rho_A > \rho_B > \rho_C$ as shown in Figure 11.[60] Therefore, by applying pressure, the rare earth oxides prefer to form A rather than B and C and B than C. From the figure, it is clear that the observed lanthanide contraction in A is similar to B, while the C form shows a larger decrease in volume with cation radius decrease (Figure 11). In addition, it is possible to obtain the B form for the heavier rare earth oxides such as Tb−Lu (as shown in the break line in Figure 11). Figure 12 presents the location of the B−C transition line as a function of pressure and cation radius at 1000 °C.[61] By comparing Figures 6 and 12, we can see the resemblance of the shape between the temperature−ionic radius and the pressure−ionic radius. This indicates that both high temperature and high pressure have a tendency to stabilize the monoclinic B phase relative to the cubic C phase. However, the effect of ionic radius is appreciably larger than that of temperature or pressure for shifting the transition boundary.[61] The C to B transformation occurs with a substantial volume decrease. In contrast, the transition from the B to A form results in just a minor decrease. By heating C-type Ho_2O_3 up to its melting point at atmospheric pressure, it is observed that about 20% conversion to the B occurs by the effect of high pressure.[59] The ionic radii of Ho^{3+} and Y^{3+} are very similar, but no transformation from C to B was apparent in the case of Y_2O_3. Since the lattice constant of C type yttria (1.06021 nm) is slightly smaller than that of holumia (1.06065 nm), the pressure obtained during impact seems not to be large enough to result in the C−B conversion in yttria. However, for yttrium sesquioxide, the B−C phase transformation occurs at a pressure around 5×10^3 atm higher than that expected from its ionic radius, as shown in Figure 12.[61]

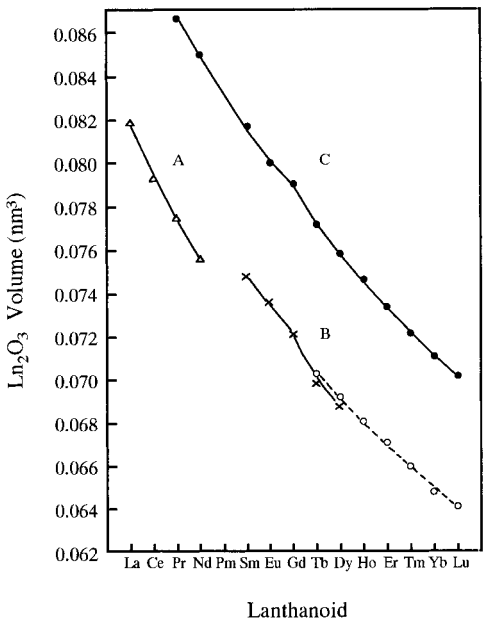

Figure 11. Molecular volume of lanthanoid sesquioxide crystal modifications. Solid line, atmospheric pressure; broken line, high pressure, $(2-4) \times 10^4$ atm. (Reproduced with permission from ref 60. Copyright 1964 American Association for the Advancement of Science.)

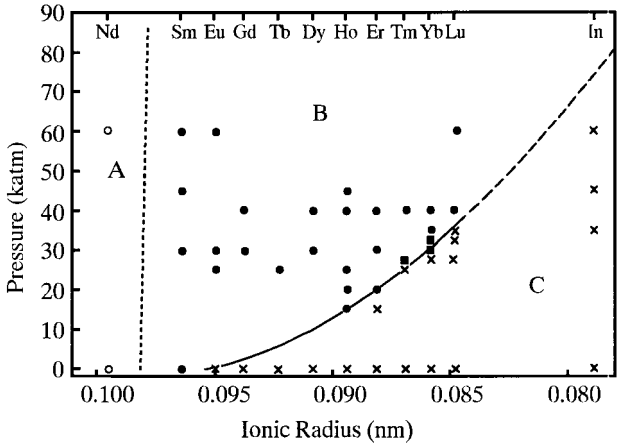

Figure 12. Lanthanoid sesquioxides: 1000 °C isotherm. (Reprinted with permission from ref 61. Copyright 1966 American Chemical Society.)

The high-pressure reactions seem to be universally reversible when the specimens are annealed at higher temperatures for a few hours after the pressure is reduced. The C−B transformation was found to be easily reversible for terbium through lutetium oxide and yttrium oxide. By heating these oxides in air at 1000 °C for several hours, the C forms are reestablished. The C−B equilibrium curves as a function of pressure (at 2×10^4 atm and at 4×10^4 atm), in a diagram with temperature and ionic radius are shown in Figure 13.[61] The equilibrium temperature shifts are significantly larger for the pressure interval from 1 atm to 2×10^4 atm than that from 2×10^4 atm to 4×10^4 atm. The conversion from the monoclinic B form to the cubic C form was confirmed

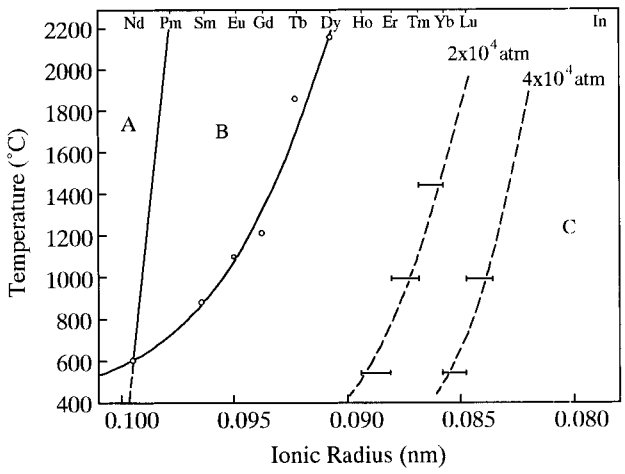

Figure 13. Pressure effect on sesquioxide phase equilibria. (Reprinted with permission from ref 61. Copyright 1966 American Chemical Society.)

Table 4. Pressure-Temperature Conditions Necessary for the Preparation of B-Type Sesquioxides (Reprinted with permission from ref 60. Copyright 1964 The American Association for the Advancement of Science)

sesquioxide	P ($\times 10^4$ atm)	T (°C)
yttrium	2.5	1000
samarium	3.0	1020
europium	2.5	905
gadolinium	3.0	1020
terbium	2.5	905
dysprosium	3.0	1020
holmium	2.5	1000
erbium	3.0	1020
thulium	4.0	1005
ytterbium	4.0	1000
lutetium	4.0	1005

by annealing the B phase in air at ambient pressure at 900 °C for several hours. By the annealing Gd_2O_3, Eu_2O_3, and Sm_2O_3 for 3 weeks at 950 °C, partial conversion from the B to the C phase occurs for the gadolinium and europium monoclinic B phases. For Sm, the transition can be expected to be sluggish because the equilibrium temperature is 875 °C and close to the annealing temperature. The reversibility of the B−C transition has been demonstrated. Only a few studies have been made of the kinetics of phase transitions without composition change. The rate of the C → B transition for Nd_2O_3, Sm_2O_3, Eu_2O_3, and Gd_2O_3 was studied and the rate of transition for Eu_2O_3 was calculated by Ainscough et al. to be zero at 1074 ± 5 °C.[62]

The sesquioxides of yttrium, holmium, erbium, thulium, ytterbium, and lutetium exist only in the C-type form. At considerably lower temperatures and at high pressure, the B form of europium, gadolinium, terbium, and dysprosium sesquioxides is obtained. The conditions under which the B form are obtained are listed in Table 4.[60] By comparing the data in Figure 13 and Table 4, it can be easily shown that high pressure decreases the transformation temperature of the sesquioxide, while a decrease of ionic radius of the rare earth component of the sesquioxide requires the transformation pressure increase.[60]

5. The Dioxides

a. The Structures of Ce, Pr, and Tb Oxides. For those rare earth elements which have an oxidation state higher than three, higher oxides of the composition range LnO_x ($1.5 \leq x \leq 2.0$) are formed in the presence of oxygen. The composition of these oxides is dependent on the temperature and oxygen fugacity and also on the physical state and history of preparation. Such oxide systems are found only with Ce, Pr, and Tb.

When oxygen is removed from this structure the crystalline form obtained is either the fluorite-related homologous series of the intermediate oxides or phases of a functionally wider stoichiometric range. The former types are the intermediate oxides with the generic formula Ln_nO_{2n-2m} and the latter types are the phases $Ln_2O_{3+\delta}$ (σ phase) or $LnO_{2-\delta}$ (α phase) (as described in section III.B). The C-type sesquioxide with bixbyite structure is fluorite-related and is the compositional end-member of the higher oxides. Two widely nonstoichiometric phases, denoted as σ and α, which appear at higher temperatures and oxygen pressures are related to the C-type and the fluorite-type structures, respectively. At high temperatures, the C-type oxide ($LnO_{1.50}$) absorbs oxygen to around $LnO_{1.70}$. There exists a narrow miscibility gap to approximately $LnO_{1.72}$, and then a fluorite-type oxide of wide composition variability oxidizes smoothly to the dioxide. There is a close similarity in the oxide systems of Ce, Pr, and Tb. Of these three, terbium oxide would be likely to show similar behavior when higher oxygen pressures are applied. The fluorite-related α phases order at lower temperatures and oxygen pressures and form the series of ordered intermediate oxides. From the C-type related σ phase, no such complex was found at lower temperatures.

Recently, the compositional and structural characteristics for the anion-deficient, fluorite-related oxide systems have been determined.[63−65]

The probability is equal for the removal of any one of the eight oxygen atoms in the fluorite-type module. Further, any module with more than two vacant oxygen sites is unstable from the repulsive energy point of view. Therefore, the type is restricted to one having the following structural characteristics (Figure 14[66]): (1) no vacant oxygen sites designated as F; (2) one oxygen vacant site which has the apex pointing up designated as U^i (four orientational variations; U^1, U^2, U^3, and U^4); (3) one oxygen vacant site which has the apex pointing down designated as D_j (four orientational variations; D_1, D_2, D_3, and D_4); and (4) two vacancies which exist as a pair along the body diagonal of the cube designated W^i_j (four orientational variations; W^3_1, W^4_2, W^1_3, and W^2_4).

Shown in Figure 15[63] are 10 of the 14 possible modular types, together with the modular orientation, and the choice of numbering the corners and faces. (In these drawings, the cubic module is depicted in the [112] zone. The three types W^3_1, W^4_2, and W^2_4 are omitted here.) Every superstructure possesses exactly some multiple of the same eight types of oxygen vacancies with periodic repetition. This indicates that equal numbers of tetrahedrally

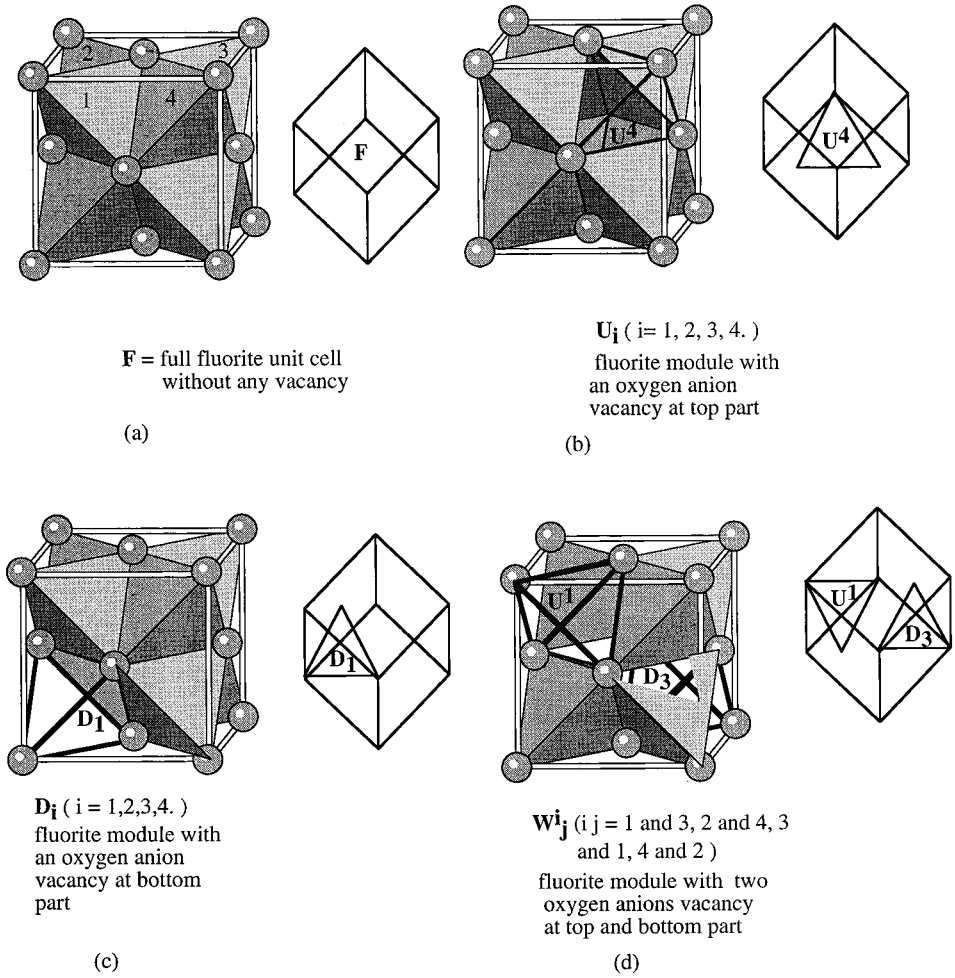

Figure 14. The four varieties of fluorite-type modules, F, U^i, D_j, and W_j^i, and their projection along $[112]_F$. (To appear in ref 66.)

coordinated vacancies pointing up and down exist with their vectors in opposition (for example, $m[U^1U^2U^3U^4D_1D_2D_3D_4]$) or if a W module exists, the corresponding vacant sites involved must be eliminated from the U and D content. The F module is necessary to adjust the composition of series members.

Each modular unit volume consists of $4n$ metal atoms with $8n - 8m$ oxygen atoms. Thus, the modular unit cell formula is described as $R_{4n}O_{8n-8m}$ which is four times the contents of the superstructure unit cell. Therefore, the generic formula of the unit cell contents is R_nO_{2n-2m} with $2m$ vacant oxygen sites per unit cell. If the composition is written as RO_x, m can be obtained from; $m = n - (nx)/2$. The established higher oxides, the value of n and m, the modular content, the atomic content of the unit cell, and the oxygen/metal atom ratio of the oxide is tabulated in Table 5.[63,67] The packing of the modules determines the charge distribution. The region of the U, D, and W modules are relatively positive, while the F module is relatively negative. The charge distribution of the oxides is determined by the minimum free-energy configuration.

For example, the first member of the series, Pr_7O_{12} must have the modular composition, W3U3D. The modular order seen in the [112] direction with the W unit in the center, is $U^2U^1D_2W^3{}_1U^4D_3D_4$ along [010], and $D_2U^2D_3W^3{}_1U^1D_4U^4$ along [100]. The projection and crossing of the above-mentioned sequences with the unit cell marked is presented in Figure 16a.[63] To form the full unit cell, three layers are necessary. The layers immediately above and below the $W^3{}_1$ module are juxtaposed to create the full unit cell as shown in Figure 16b.[63]

Terbium oxide can be obtained as Tb_2O_3, $TbO_{2.0}$, and a homologous intermediate oxides series, Tb_2O_{2n-2m}. The $Tb_{62}O_{112}$ ($n = 62$, $m = 6$) phase appears only in the reduction process from Tb_7O_{12} ($n = 7$, $m = 1$). The phase variation appearing in terbium oxides is very similar to the examples shown by cerium and praseodymium oxides. Single phases of the polymorphs $Tb_{24}O_{44}(\beta(2))$ or $Tb_{48}O_{88}(\beta(3))$ cannot be obtained in the bulk but exist only as intergrowths in small size domains. The known higher oxide phases of the above-mentioned three systems, together with preparative and structural information are reported in ref 1.

b. The Cerium−Oxygen System. A phase diagram for the Ce−O system is shown in Figure 17.[1,68] At lower temperatures, $CeO_{2.0}$ loses oxygen to form certain members of the homologous series Ln_nO_{2n-2m} depending upon the oxygen pressure. Each of the intermediate phases decomposes peritectoidally to form a nonstoichiometric phase and an adjacent ordered phase except for the ι (iota) phase ($n = 7$, m

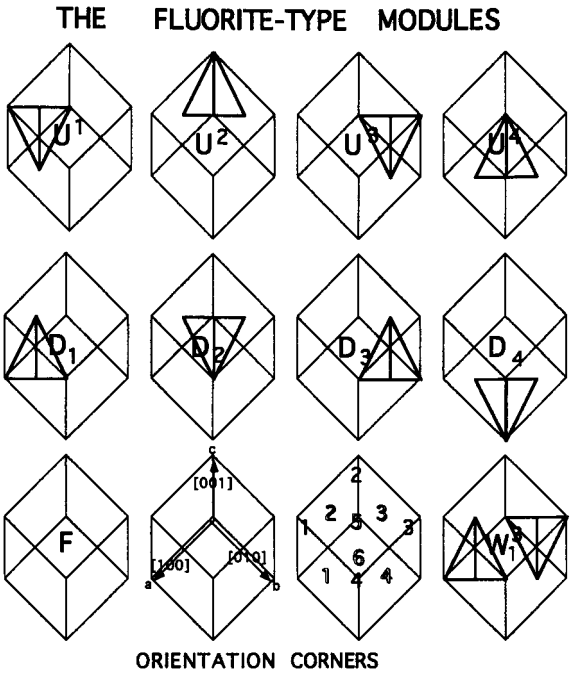

Figure 15. The convention showing 10 of the 14 possible modules for modeling all the higher oxide structures. The directions of [001], [100], and [010] and the *a*, *b*, and *c* axes in the [112] zone and the numbering of the faces and corners of the cubic module are shown. (Reproduced with permission from ref 63. Copyright 1997 Elsevier Science S. A.)

Table 5. The Unit Cell Content of the Members for the R_nO_{2n-2m} Series (Reprinted with permission from ref 63. Copyright 1997 Elsevier Science Publishers S. A.)

phase designation, and representatives	*n*	*m*	modular content	formula/unit cell content	*Q*/*R*
ι (Ce, Pr, Tb)	7	1	**W**3**U**3**D**	R_7O_{12}	1.714
ζ (Ce?, Pr)	9	1	**F**4**U**4**D**	R_9O_{16}	1.778
δ(1) (Ce, Tb)	11	1	3**F**4**U**4**D**	$R_{11}O_{20}$	1.818
β(0) (Pr)	12	1	4**F**4**U**4**D**	$R_{12}O_{22}$	1.833
π (Ce?, Pr, Tb)	16	1	8**F**4**U**4**D**	$R_{16}O_{30}$	1.875
M19 (Ce)	19	2	3**F**8**U**8**D**	$R_{19}O_{34}$	1.789
β(1) (Pr)	24	2	8**F**8**U**8**D**	$R_{24}O_{44}$	1.833
β(2) (Tb)	24	2	8**F**8**U**8**D**	$R_{24}O_{44}$	1.833
M29 (Ce)	29	3	5**F**12**U**12**D**	$R_{29}O_{52}$	1.793
M39 (Ce)	39	4	7**F**16**U**16**D**	$R_{39}O_{70}$	1.795
ϵ (Ce?, Pr)	40	4	8**F**16**U**16**D**	$R_{40}O_{72}$	1.800
β(3) (Tb)	48	4	16**F**16**U**16**D**	$R_{48}O_{88}$	1.833
δ′ (Ce, Pr, Tb)	62	6	14**F**24**U**24**D**	$R_{62}O_{112}$	1.806
δ(2) (Pr)	88	8	24**F**32**U**32**D**	$R_{88}O_{160}$	1.818

= 1) which decomposes to two definite nonstoichiometric phases. The peritectoidal decomposition temperatures were observed to be 1025 ± 5 °C for *ι* (*n* = 7, *m* = 1), 625 ± 10 °C for *ζ* (*n* = 9, *m* = 1), 585 ± 10 °C for *ϵ* (*n* = 40, *m* = 4), 445 ± 10 °C for *δ* (*n* = 11, *m* = 1), and the *δ* + α eutectoid occurs at 435 ± 10 °C.

At higher temperatures, two nonstoichiometric phases of *σ*($Ce_2O_{3+\delta}$) and α($CeO_{2-\delta}$), dominate the phase diagram. By a high-temperature X-ray analysis, the above-mentioned high-temperature phases are shown to be bixbyite-related and fluorite-related phases with widely varying their lattice parameters.

By neutron diffraction measurements of powders and single crystals, the structure of Ce_7O_{12} (*ι* phase)

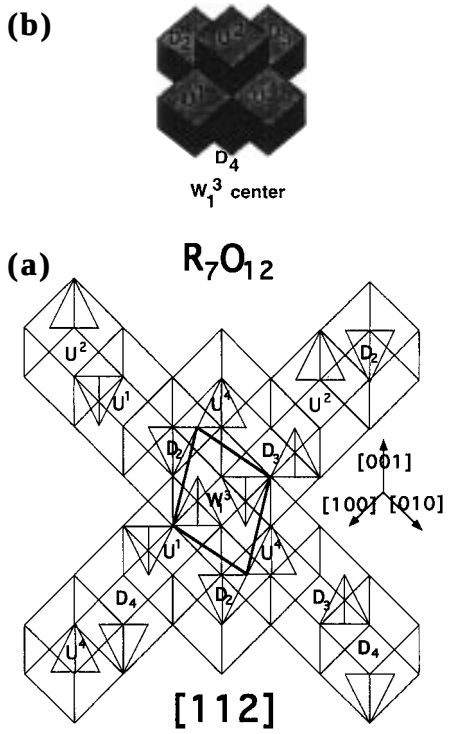

Figure 16. (a) The arrangement of face-sharing modules in a (112) plane of the compound with *n* = 7 (*ι* phase). The unit cell projection is highlighted. (b) The layers immediately above and below the W_1^3 module. (Reproduced with permission from ref 63. Copyright 1997 Elsevier Science S. A.)

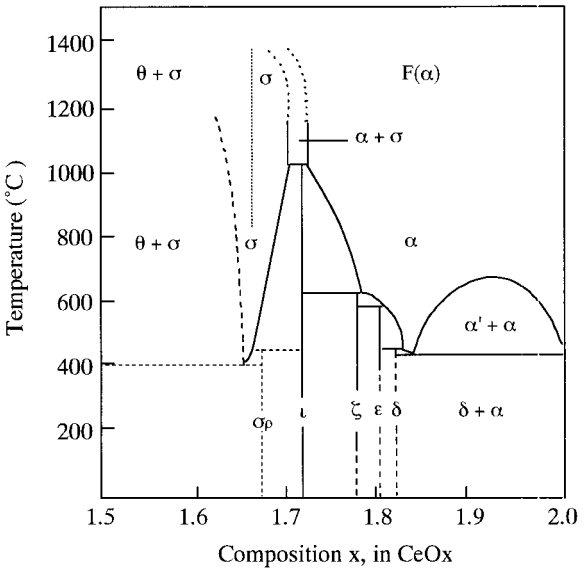

Figure 17. A phase diagram for the CeO_x−O_2 system. (Reproduced with permission from ref 1. Copyright 1991 Kluwer Academic Publishers.)

was determined.[52] The compound was identified to be isostructural with Pr_7O_{12} (see section III.C.3.). The space group of Ce_7O_{12} is $R\bar{3}$ with a hexagonal unit cell dimensions *a* = 1.037 nm and *c* = 0.967 nm (rhombohedral cell *a* = 0.679 nm and α = 99.40°). The hexagonal cell is composed of three formula units of Ce_7O_{12}. From a neutron diffraction study of the single crystal, the structure was identified as a rhombohedral defect fluorite-type structure where

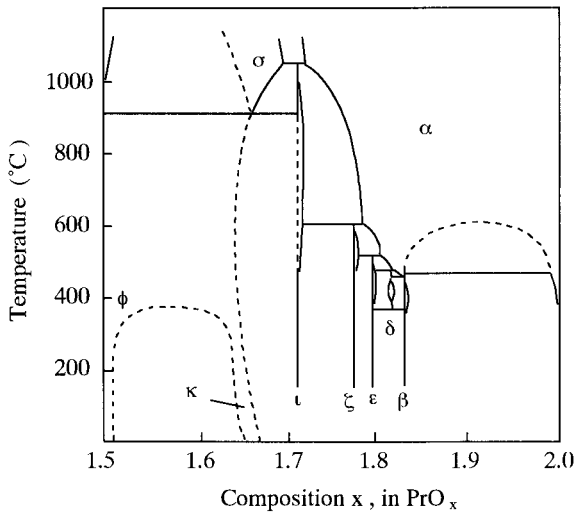

Figure 18. A phase diagram for the PrO_x-O_2 system. (Reproduced with permission from ref 1. Copyright 1991 Kluwer Academic Publishers.)

Table 6. Phase Nomenclature in the $PrO_x + O_2$ System[a] (Reprinted with permission from ref 71. Copyright 1966 The Royal Society)

phase composition, x in PrO_x		designation
disordered, nonstoichiometric phase, $2.00 \geq x \geq 1.72$		α, α^m
1.833 (ordered)	($n = 12$, $m = 1$)	β
1.818	($n = 11$, $m = 1$)	δ
1.800	($n = 40$, $m = 4$)	ϵ
1.778	($n = 9$, $m = 1$)	ζ
1.714	($n = 7$, $m = 1$)	ι
wide-range, disordered, nonstoichiometric phase, $1.7 \geq x \geq 1.6$		σ, σ^m
1.500 (C type)		ϕ

[a] The superscript "m" indicates metastable existence of a phase, σ^m and α^m are particularly liable to occur.

pairs of oxygen vacancies are ordered along the [111] direction.

c. The Praseodymium−Oxygen System. The system of the praseodymium oxides has been the most thoroughly studied among the systems of Ce, Pr, and Tb oxides. When some praseodymium salts which decompose to the oxide are gradually cooled in air, the final composition is shown as Pr_6O_{11}. Actually the composition of the unit cell should be written as $Pr_{24}O_{44}$. The phase diagram is shown in Figure 18.[1,68−72]

Table 6 lists the stoichiometric formula and its phase designation.[71] The C-type sesquioxide ϕ, is regarded as a fluorite type in which 25% of the anion sites are vacant and ordered. β, δ, ϵ, ζ, and ι are similar. PrO_2 and α are face-centered cubic, and ϕ and σ are body-centered cubic.[71] When $^1/_{12}$ of the oxygen atoms are missing, this gives a unit cell composition of $R_{24}O_{44}$ of the β phase. When one oxygen atom in 11 is removed from the RO_2 structure, $R_{11}O_{20}$ (δ phase) is formed. $Pr_{40}O_{72}$ (ϵ phase) and Pr_9O_{16} (ζ phase) also exist in the Pr−O system. The crystal structures of Pr_9O_{16}[73] (ζ phase), $Pr_{40}O_{72}$[74] (ϵ phase), and $Pr_{12}O_{22}$[75] (β phase)are clarified by Kang et al.

In the β phase ($n = 12$), four polymorphs are known. The $\beta(1)$ structure was only identified in the Pr−O system and $\beta(1)$ can be frequently observed. The primitive $\beta(0)$ phase is rarely observed. It is very interesting to see the existence of the phase believed to be the $n = 16$ member of the homologous series. The $n = 16$ phase is designated as π since π is the 16th letter in the Greek alphabet. The π phase also belongs to the homologous series of Ln_nO_{2n-2m} and possesses common **a** and **c** axes with $Pr_{40}O_{72}$, $Pr_{11}O_{20}$, and $Pr_{12}O_{22}$ [$\beta(1)$].

The advance in structural analysis and other observations of intrinsic properties can be obtained with single crystals of the higher oxides of praseodymium and terbium prepared by hydrothermal growth.[76] This detail will be discussed in section V.E.

All phases of the oxides higher than the sesquioxide exhibit the fluorite-related structure. Several ordered and disordered intermediate phases are found between $Pr_{2.0}O_{3.0}$ and $PrO_{2.0}$. A single-phase PrO_x can be obtained for all x between 1.50 and 2.00 except for a narrow miscibility gap around $PrO_{1.71}$. However, only one intermediate phase which has been structurally identified in the binary higher oxides is the Pr_7O_{12}, ι phase, with space group, $R\bar{3}$. The structure has been investigated by using a total profile analysis of neutron powder diffraction data.[77] Pr_7O_{12} can be drawn from the RO_2 fluorite structure and a pair of vacancies exists in the oxygen array along the rhombohedral [111] direction. Both the cation and anion arrays relax around the vacancies. All the metal atoms in the fluorite-related Pr_7O_{12} structure, are either six- or seven-coordinated.[78] The six-coordinated metal atoms all exist in {135} planes, and each atom is surrounded by two oxygen vacancies and six seven-coordinated metal atoms along [111]. The structure is isomorphous with UY_6O_{12} (Figure 19[79] determined by Bartram[80] in which strings of oxygen vacancies exist in the [111] direction of an hexagonal array of third nearest metal neighbors). The Pr_7O_{12} structure is closely related to the fluorite PrO_2 when one-seventh of the oxygen atoms were orderly removed.

In Figure 20, the isobaric information on the PrO_x-O_2 system is presented.[1] The regions of oxygen pressure and temperature where the various intermediate phases exist have been clarified. Metastable and uncertain boundaries are indicated as dashed lines.[71] Metastable phases α, σ, and ι, are denoted as α^m, σ^m, and ι^m in the composition range $1.68 < x < 1.72$ of the PrO_x system. The lines indicating $\alpha_1-\alpha_4$ show regions of the phase ranges with some kind of thermodynamic and probably structural anormalies.[81] This phenomenon has been reported in more detail elsewhere.[82]

d. The Terbium−Oxygen System. The phase diagram of the Tb−O system is presented in Figure 21.[1,83−89] (By treating the lower oxides of Tb and Pr at 2.82×10^2 atm of oxygen at 400 °C, $TbO_{1.85}$ and $PrO_{2.00}$ can be obtained.[84] A composition of $TbO_{1.75}$ could not be isolated because a slow oxidation of a lower oxide occurs when it is cooled in oxygen or air.[85] The phase diagram of the Tb−O system is much more simple than that of the Pr−O system.[86] A tensimetric[87] and high-temperature X-ray diffraction[88] study of terbia were done.) By using the combined methods

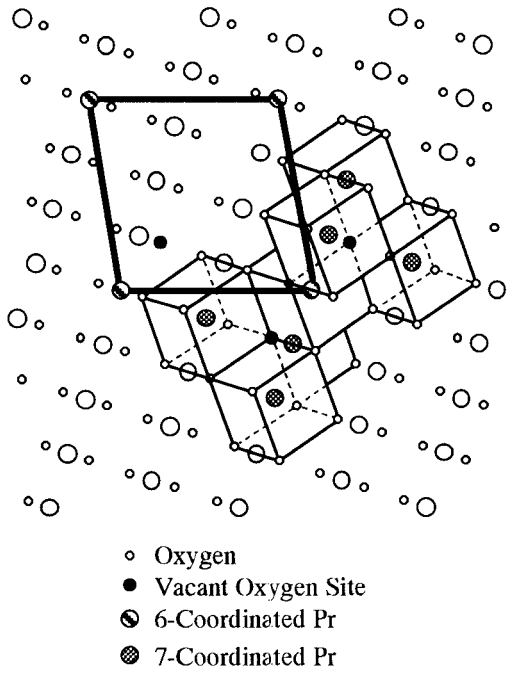

Figure 19. The unit cell of Pr_7O_{12} along ⟨211⟩ (heavy solid lines). All the praseodymium atoms are coordinated cubically with oxygen in the fluorite structure as shown by the cubes drawn about the metal atoms. There are two vacant oxygen sites (•) along the body diagonal of the fluorite unit cell in Pr_7O_{12}. The atoms at the corners of the unit cell drawn are six-coordinated and all others are seven-coordinated. (Reproduced with permission from ref 79. Copyright 1988 Academic Press, Inc.)

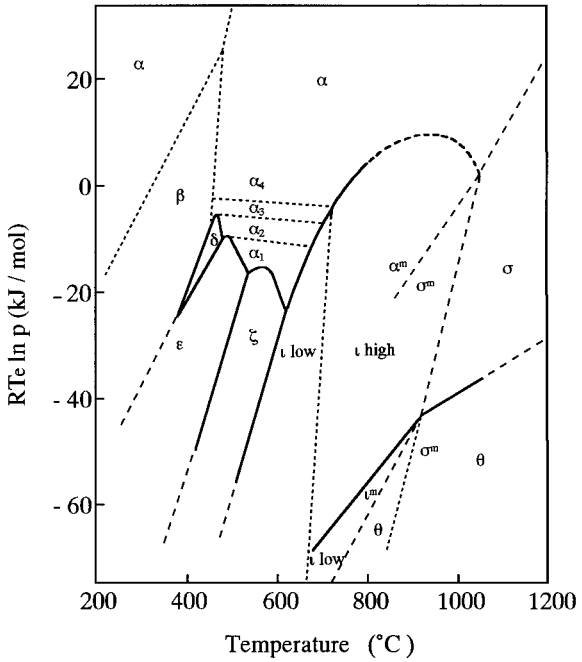

Figure 20. A phase diagram for the range required to prepare the intermediate Pr_nO_{2n-2m} phase. (Reproduced with permission from ref 1. Copyright 1991 Kluwer Academic Publishers.)

of electrical resistance as a function of temperature and pressure and by high-temperature X-ray diffraction, TbO_x in the region where $1.5 < x < 1.714$ was investigated.[89] Similar features as obtained for CeO_x and PrO_x at low temperatures and pressures, were also observed for TbO_x. The ι-Tb_7O_{12} phase is an extremely stable phase similar to those for CeO_x and PrO_x.

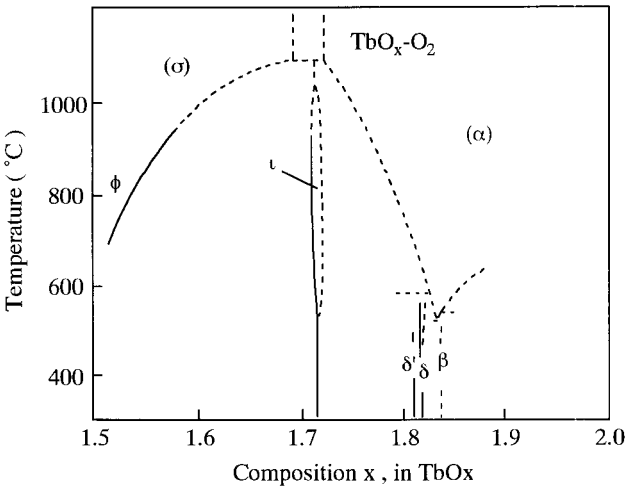

Figure 21. A phase diagram for the TbO_x-O_2 system. (Reproduced with permission from ref 1. Copyright 1991 Kluwer Academic Publishers.)

As in the cases of the cerium and praseodymium oxides, terbium oxide can be also synthesized as Tb_2O_3, TbO_2, and a homologous series of intermediate oxides, Tb_nO_{2n-2m}. In the higher rare earth oxides, that is, Ce, Pr, or Tb oxides, delta (δ) ($n = 11$, $m = 1$), epsilon (ϵ) ($n = 40$, $m = 4$), zeta (ζ) ($n = 9$, $m = 1$), and iota (ι) ($n = 7$, $m = 1$) are intermediate phases with definite stoichiometry and are expected to have crystal lattices with well-ordered deficiencies. The reaction path either goes from a disordered phase to an ordered phase or vice versa. In general, the path from a disordered to an ordered phase is hindered and slow; metastable conditions of equilibrium often occur. In contrast, the path from an ordered to a disordered phase, or even to another ordered and structurally similar phase, is usually fast. Phase transformations involving an ordering process are sluggish while transitions from an ordered to a disordered phase are relatively fast.

Tb_7O_{12} (ι phase) was found to be isostructural with Pr_7O_{12} from the Rietveld analysis of neutron diffraction data. In Tb_7O_{12}, two types of cations exist. One is the six-coordinated Tb(1) with a +4 formal charge and the other, Tb(2), possesses a formal state of +3.33. The six seven-coordinated Tb cations might be, indeed, two +4 and four +3 ions. In contrast, the charge distribution in $Tb_{11}O_{20}$(δ phase) is different. The two eight-coordinated Tb cations (Tb(1) and Tb(2)) are in a +3 state. Of the other four Tb atoms, Tb(5) and Tb(6) are thought to be +4 and the remaining Tb cations, Tb(3) and Tb(4), are estimated from calculation of electrical neutrality to hold an average charge of +3.75.[90]

Tb_7O_{12} (rhombohedral ι phase), which is isomorphous to that of Ln_7O_{12} for Ce and Pr is composed of strings of oxygen vacancies in the ⟨111⟩ direction. The intermediate phase of $Tb_{11}O_{20}$ possesses a triclinic structure. $Tb_{12}O_{22}$ (β phase) is monoclinic and the cell volume is twice as large as that of the β phase in Pr−O due to a doubling of the **b** axis. From electron diffraction analysis, two $n = 12$ polymorphs are found in Tb−O system. The polymorph of $Tb_{48}O_{88}$, which

is referred to as $\beta(3)$, has twice the unit cell volume of both $Pr_{24}O_{44}$ ($\beta(1)$ phase) and $Tb_{24}O_{44}$, which has the $\beta(2)$ phase. A metastable phase of $Tb_{16}O_{30}$ (π phase) has been identified by electron optical techniques. The $n = 16$ phase is the most highly ordered intermediate phase in the Ln_nO_{2n-2m} series in the binary rare earth oxides. By heating the $Tb_{16}O_{30}$ phase by a selected area diffraction, a reduction occurred and results in a mixture of $Tb_{24}O_{44}$ ($\beta(2)$) and $Tb_{11}O_{20}$ (δ phase). Since no $n = 16$ homologue was found by extensive tensimetric investigations and given its infrequency of occurrence in electron microscopic observations, the $Tb_{16}O_{30}$ phase is thought to be metastable.

6. The High Temperature Phases

The existence of two new structure types of rare earth sesquioxides appearing at higher temperatures just below the melting points are reported.[9,91] The high-temperature phases are not quenchable down to room temperature. The H form is expected to possess a crystal structure of hexagonal symmetry and closely related to the well-known A from. From the neutron diffraction analysis, H and X phase are found to be hexagonal ($P6_3/mmc$) and cubic ($Im3m$), respectively.[92] The difference in the X-ray powder patterns of the modifications between A and H is very slight, and is shown in the relative position of the diffraction lines. The number and relative intensity of the lines are, however, the same. The transformation between A and H is detectable by a break in the slope of the curve in the temperature vs the lattice parameter dependencies (hexagonal **a** or **c** constant.). The transformation is clearly indicated by a sudden but small change in the **c/a** ratio.

Figure 22 shows the corresponding curves for La_2O_3.[93] Similar behavior is observed for the A−H transformations of both Pr_2O_3 and Nd_2O_3. The oxides from La_2O_3 through Gd_2O_3 show a phase transition from the H to the X form at very high temperatures. It seems to be probable that the H form has a lower density than the X form. This conclusion has been drawn from the phenomenon that a concave top surface giving the X form was obtained from the beads of the molten oxides from La_2O_3 through Gd_2O_3, while the molten oxides from Tb_2O_3 to Yb_2O_3 solidify in the H form with a convex top surface.

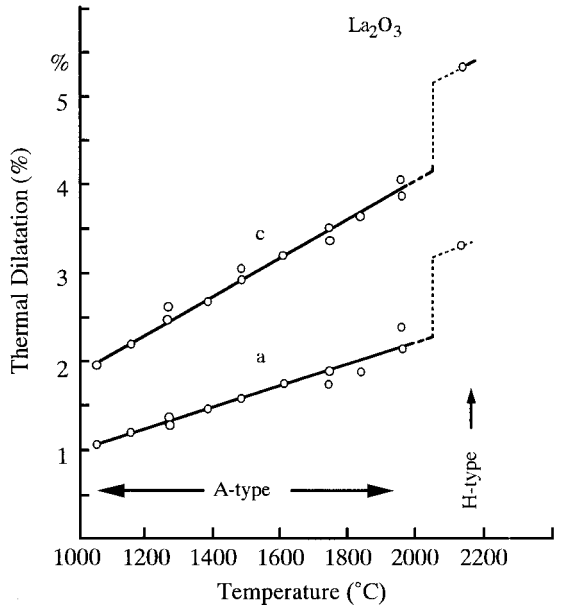

Figure 22. Lattice constants of hexagonal La_2O_3 at high temperatures, demonstrating the transformation from the A type to the H type structure by plotting the thermal dilatation (%) of the lattice constants *a* and *c*. (Reproduced with permission from ref 93. Copyright 1968 Pergamon Press.)

7. Kinetics

The information of the kinetics of heterogeneous reactions with lanthanide oxides has been obtained mainly for the C-type sesquioxides or the fluorite-related higher oxides. In these materials, oxygen moves very smoothly, while metal atom migration is extremely limited at temperatures lower than 1200 °C. The oxidation and reduction process have been described in the following reactions:[94−97]

$$PrO_{1.714}(Pr_7O_{12})\ (\iota) + 0.032O_2 \rightarrow PrO_{1.778}(Pr_9O_{16})\ (\zeta)^{94} \quad \text{(I)}$$

$$(^1/_7)Pr_7O_{12}\ (\iota) + (^1/_7 - x/2)O_2 \rightarrow PrO_{2-x}\ (\alpha)^{95} \quad \text{(II)}$$

$$(^{10}/_9)Pr_9O_{16}\ (\zeta) + (^1/_9)O_2 \rightarrow Pr_{40}O_{72}\ (\epsilon)^{96} \quad \text{(III)}$$

$$(^7/_2)Tb_2O_{3+a}\ (\phi) + (^3/_4 - 7a/4)O_2 \rightarrow Tb_7O_{12}\ (\iota)^{97} \quad \text{(IV)}$$

For reactions II and IV, the mechanisms to consider involved coherently intergrown crystals, and this mechanism was clarified by calorimetric measurements.[15] The ordered intermediate phases (Pr_nO_{2n-2m}) are coherently intergrown at the unit cell level, while for the disordered α phase (PrO_{2-x}) this is not the case. The sharp change in the partial molar enthalpy around Pr_9O_{16} is thought to result from the phase variation of the coherently intergrown ordered phases and the disordered α phase. The difference between the partial molar entropy on reduction and on oxidation is accounted for both by the regular solution model and the usual thermodynamic treatment.[98]

From a consideration of the partial molar enthalpy, the Tb−O system for reaction IV can be divided into four compositional regions. The first is the $TbO_{1.5+x}$ region which can be described by a point defect model and strong interaction among excess oxygen atoms. The second is the region between $TbO_{1.54}$ and $TbO_{1.61}$. This region is described as the intrinsic hysteresis region and covered by the regular solution model. The region between $TbO_{1.61}$ and $TbO_{1.70}$ is the third and is identified as a pseudophase region. The region of ι phase is the fourth, and the partial thermodynamic quantities can be compared with those of the ι phase for Ce, Pr, and Tb.[99] In the case of the oxidation kinetics in solid−gas reactions, either a diffusion or a phase boundary reaction process is generally a controlling factor. At temperatures lower than 500 °C, the dominant component in the $\zeta-\epsilon$ reaction is

the phase boundary reaction. In contrast, at higher temperatures around 800 °C, the diffusion process cannot be neglected similar to the case of the reaction IV. This means that the activation energy of the diffusion process should be smaller than that of the phase boundary reaction one.

At the beginning of the reaction IV, a nucleation process occurs extremely rapidly on the crystal surface, which is immediately covered by a product. The rate of the reaction is then controlled by the progression of the resulting interface to the direction of the center of the crystal where the rate is governed by both diffusion and a phase boundary reaction. The reaction of IV goes along the oxidation branch according to the following pathway:

$$Tb_2O_{3+a} \rightarrow Tb_7O_{12-d\ (\text{pseudophase of } \iota)} \rightarrow Tb_7O_{12}$$

The final stages of the reaction are determined by the conversion rate of the transition from the pseudophase of ι to the well-ordered ι phase.

The kinetic curves of the solid−gas reaction do not fit well enough to the usual models of phase reaction, such as diffusion, moving boundary or nucleation and growth control, but are more closely matched by a phenomenological model which takes the hysteresis curve into account. The phenomenological treatment of the phase reaction of I points to environmental factors that influence the mechanism of reaction. Hence, the reaction rate is determined by several of these factors. The macroscopic characteristics of these systems have been studied.

For the reaction II, a reproducible hysteresis loop that depends on both the temperature and pressure, is observed. An inflection point exists around a composition of $PrO_{1.75}$. The inflection point is regarded as a phase, Pr_8O_{14} (η) which is coherently intergrown to give an average composition, $PrO_{1.75}$. Pr_8O_{14} (η) phase is not listed in Table 5, and the existence of the phase is not well-determined yet.

By plotting the temperature dependence of the observed rate constants, the activation energy for oxidation and reduction was obtained (314.3 and 255.2 kJ/mol, respectively). However, the values are significantly higher than those for the reaction I. The reason is not clear, but, could be explained as follows. If the oxygen-vacancy pair movement from its position in ι to that in ζ or η is the rate-determining step, the movement from ι to ζ would need less energy in comparison with that from ι to η, since there is a structural difference between the odd members of the homologous series and the even ones.

At the other extreme, the structures of the ordered intermediate phases have been clarified by HRTEM methods at the atomic level. By electron microscopy, structures of the two-phase reaction zones have also been imaged, and intergrowths, which indicate the cause for the intrinsic hysteresis observed in the thermodynamic studies, have been revealed. Attempts to explain hysteresis by invoking metastable states, via regular solution theory, have been done.[100] Inaba et al. have indicated that if the configurational entropy of the reacting system is higher the fit would become much more realistic and would explain the observed fine texture of the intergrowth structures.[5]

D. High Resolution Electron Microscopy(HREM)

It is difficult to determine either the unit cells or structural forms of the Ln_nO_{2n-2m} series by either X-ray or neutron diffraction studies. However, electron microscopy can provide structural and analytical information for regions of limited size.[101,102] When the scanning is completed, the beam pattern can be varied from a diameter equivalent to the sample to the resolution limit of the microscope. From HRTEM, the unit cells of the homologous series can be obtained together with their structural form. It is very difficult for high-resolution analyses to see rapid reactions at very low illumination levels. However, by successively imaging the same area, it is possible sometimes, to identify the reaction path.[78] A few amperes per square centimeter of high-energy electrons are necessary for high-resolution imaging in a modern electron microscope. The beam impact causes the knock-on of lighter atoms and a radiolysis reaction. The reactions are divided into two types: One is the reaction directly induced by reaction with the electron, the other is that induced thermally.[58]

Real crystals are full of defects. To study such a defect structure, one useful technique is HREM. The electron diffraction method was used to obtain many unit cells of the Pr and Tb oxides homologous series and the imaging of the structures of the odd members of the series was suggested. The technique was then used to correlate calculated and observed images, and a structure for the even series member, $Pr_{12}O_{22}$ ($\beta(0)$), was derived as described below. The resolution method is a useful tool to indicate the nature of the defects in such higher oxides and is also an advantageous way in which to directly observe the reaction process. The extended defects and texture of real solids can also be described in detail at the several unit cells level by means of HREM and by a selected-area electron diffraction. Such structural details will contribute appreciably to defining the next level of description of the mechanism and the dynamics of phase transformations and chemical reactions in solids. The disproportionation process was also clarified by Kang and Eyring with the HREM technique.[79,103] The leaching process propagated from defects at the surfaces (e.g., emergence of dislocations) and progressed inward. For instance, the single-phase Pr_7O_{12}, which loses Pr^{3+} ions into the solution and then $PrO_{2.0}$ is obtained without a reconstruction step. From electron microscopy, it was shown that extended crystal defects, probably dislocations, occur with the dissolution of the oxide and its removal in the reaction path.

By comparing the solvolytic reaction between Pr and Tb oxides, the ratio of oxygen transport in the bulk to that along defects in the leaching process is shown to be smaller in PrO_x compared with that in TbO_x. An explanation is that the pits in the TbO_x are relatively broad while in PrO_x they are deeper

and narrower. The conditions of the solvolytic attack is also different. The leaching of PrO_x was conducted at room temperature. In contrast, the leaching of TbO_x was at around 100 °C to get reasonable reaction time. This is because the more basic characteristics of PrO_x to water and acids results in a higher reactivity. The solvolytic disproportionation is the only method that can produce $TbO_{2.0}$ in substantial amounts.

The oxides of Ce, Pr, and Tb, which are grouped into higher oxides, have been intensively investigated by the electron microscopic method.[104] Oxidation and reduction of the oxides were controlled by adjusting the oxygen pressure and the temperature of the sample. Small fragments of the crystalline oxides were prepared. The degree of reduction by the electron beam was larger than that expected from equilibrium tensimetric investigations without the beam bombardment. The reoxidation process also seems to be more sluggish and to an extent which is less than that observed in oxides reacting in an ambient environment outside the microscope chamber. In situ high-resolution electron microscopic studies provide some insight at the atomic level on structures and defects which exist on surfaces and in thin films but only for the stable intermediate phases which exist. As the rare earth oxides are used as catalyst and catalyst supports, it is of great interest to know their surface structure. The reconstruction of the surface, which is related to the subsurface superstructures and defects, has been frequently studied.[105,106] Under the influence of an electron beam, a specimen of $PrO_{2.0}$ was observed to lose oxygen in situ. In this process, $Pr_{12}O_{22}$ merged with a concomitant distortion of the cubic structure and accommodated the vacant oxygen sites resulting in a shift in atomic positions. This phase possesses a well-ordered superstructure. The $Pr_{12}O_{22}$ ($\beta(0)$ phase) appears at an early stage in the electron beam reduction in HREM for $PrO_{2.0}$. A further reduction occurs with the more oxygen-deficient ordered phase of $Pr_{40}O_{72}$ (ϵ phase). Between the two phases, one can see a disordered stacking of vacancy planes with variable width.[107]

A HREM study[56] and a thermodynamic study[53] indicate the occurrence of $Ce_{62}O_{112}$ ($n = 62$, $m = 6$) and $Ce_{88}O_{160}$ ($n = 88$, $m = 8$) rather than Ce_9O_{16} and $Ce_{10}O_{18}$. Both $Ce_{62}O_{112}$ and $Ce_{88}O_{160}$ possess a fluorite-related structure and belong to the members of the homologous series of Ce_nO_{2n-2m}.

High-resolution electron microscopy is, practically, very useful for imaging thin solid specimens at the atomic level.[108] By combining HREM with real-time video recording and subsequent image processing, the microscope system becomes a useful nanochemical tool to study the dynamics of solid-state chemical systems. Since many real crystal bulk crystals are full of defects, it is necessary to study their defect structures. HREM is, really, an advantageous tool to ascertain the real structures of rare earth oxides.

The formation of the B phase of Pr_2O_3 and Nd_2O_3 can be observed by quenching inside the microscope, where the high temperature was attained by heating the oxides with the electron beam itself. The B phase was obtained as epitaxial layers on the A form. The B layers are not stable and transform to the A form in a few minutes. The B layers are obtained as a result of the stress occurring during quenching and not by the quenching process itself. From the electron microscopy measurements of the Ce−O film samples, the formation of various known CeO_x (such as Ce_7O_{12}) and recent clarified structures (such as $Ce_{62}O_{112}$) in the bulk state were revealed. The clarified phase appearance can be understood by considering the far-from-equilibrium thermodynamic conditions.[109]

With the high-resolution transmission electron microscope (HRTEM), selected area electron diffraction and structure can be imaged by two-dimensional representation. The resolution of dynamic reactions is around 0.1−0.35 nm and provides a more intimate way of examining occurrences at the atomic level. During the course of the reaction from Pr_9O_{16} (ζ phase) to $Pr_{2.0}O_{3.0}$ (ϕ phase), the reaction did not advance very far.[110] Well-crystallized Pr_9O_{16} (ζ phase) exists in the thicker regions, while a substantial amount of the $Pr_{2.0}O_{3.0}$ (ϕ phase) appears only in the thinner parts. Structural data on highly defective and intergrown crystals can be effectively obtained by HRTEM. The defect crystal structures for Pr_9O_{16} (ζ phase) and for $Pr_{40}O_{72}$ (ϵ phase) were indicated by HRTEM. During the electron microscopic observation of the ϵ phase, the beam energy was controlled as low as possible to prevent structural change, because the ϵ phase is less stable than the ζ phase under these conditions. The primitive triclinic unit cell of the δ phase is well identified in the Tb−O system. Dynamic atomic-level changes were observed in situ in HREM for a 1200 atm $TbO_{2.0}$ promontory. From the video recording, the disordering that occurs prior to the recrystallization and accretion was shown.[111] The surface topography of oxygen-deficient, and nominally stoichiometric terbium oxides, was investigated at the atomic level by HREM.[112] The transformation from $Tb_{24}O_{44}$ ($\beta(2)$) to $Tb_{48}O_{88}$ ($\beta(3)$),via a partially ordered intermediate form, was also characterized (Figure 23).[113] The transformation occurs through a partially disordered intermediate characterized by wavy fringes. At the thin crystal edge, wavy fringes of narrower spacing continued, indicating further reaction to more reduced compositions.

The decomposition of $Nd(OH)_3$ to the corresponding oxide was studied by HREM by collecting atomic-level video images with a time-resolution of 30 images per second. The video recording has high potential to provide a frame-by-frame analysis at the rate of the dynamic atomic-level procedures.[114] The application of the HREM technique was also done to visualize the sintering process of the decomposition oxide obtained from colloidal particles of rare earth hydroxycarbonate.[115] HREM was also applied to identify the steps in the evolution of colloidal gels in the course of drying, aging, and crystallization into oxides.[116]

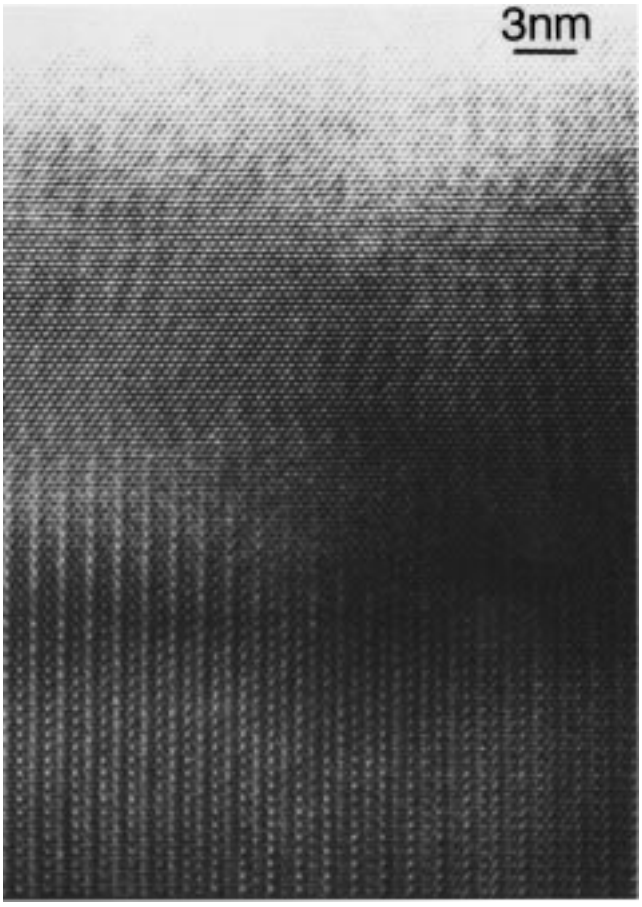

Figure 23. A $\langle 011 \rangle_F$ zone high-resolution image of a crystal beginning to transform from $Tb_{24}O_{44}$ ($\beta(2)$) to $Tb_{48}O_{88}$ ($\beta(3)$). See the development of wavy fringes at the thin edge. (Reproduced with permission from ref 113. Copyright 1989 Academic Press, Inc.)

IV. Calculation Approach to Rare Earth Oxides

A. Electronic Structure

In 1987, Pyykko[117] published a brief review of f-element molecules studied by relativistic electronic structure calculations. However, the theoretical information for lanthanide compounds is extremely limited. Much more work has been done for actinides, such as uranium, because of their applications, and these have more pronounced relativistic effects than lanthanides.[118] The electronic structure methods are limited to those that have been frequently applied to the lanthanide systems, such as the pseudopotential method, the semiempirical intermediate neglect of differential overlap method, and the relativistic Hartree−Fock (HF) self-consistent field. A review of relativistic effects and the electronic structure of lanthanide monoxides has been published by Balasubramanian.[119]

The monoxides of the lanthanide elements are the most extensively studied of the diatomic molecules both theoretically and experimentally. Recently, results obtained by QR-DFT (quasi-relativistic density-functional theory) became available. Furthermore, many LFT (ligand field theory) model calculations have been reported.[120] Bonding in the lanthanide monoxides can be considered to be significantly ionic and the limiting form is a $R^{2+}O^{2-}$ ion pair. By investigating the ground-state properties of all the diatomic monoxides of the lanthanide series, the SCF/CISD (self-consistent field/configuration interaction with single and double substitutions) level with PPs (pseudo-potentials) that contributes the open 4f shell to the core, was determined. The nonmonotonic behavior in the experimental binding energies is considerably well reproduced by the theoretical results and the vibrational frequencies are in reasonable accord with the experimental values available. However, the calculated bond lengths were found to be too long at the beginning of the series. For LaO, the bond length and a binding energy are 0.1952 nm and 6.42 eV by f PP calculations. The experimental values are 0.1826 nm and 8.24 eV. Accord between theoretical and experimental data is appreciably better at the end of the series than at the beginning. For instance, for LuO, the theoretical values of 0.18 nm and 6.12 eV are closer to the experimental values of 0.179 nm and 6.99 eV. The 4f orbitals of the lighter lanthanide elements contribute to chemical bonding, whereas the orbitals possess a core-like character as suggested by the super configuration (SC) model for the heavier lanthanide elements by Field.[121] This is a simple model for the electronic structure of the rare earth monoxides LnO (Ln = La−Lu) and is very useful for interpreting the rather complicated electronic spectra of LnO. All configurations occurring by a specific combination of a valence subconfiguration and a 4f subconfiguration are dealed as so-called SC. The SC model is qualitative and quite useful in practice in order to reduce the necessary computational effort for quantum chemical studies of lanthanide compounds. It needs some improvement for quantitative work when using PPs that include the 4f shell in the core.

The application of the SC model in the density functional approach was applied to the rare earth monoxides. The approximation scheme is the density functional (DF) approach with correlation corrections, relativistic first-order perturbation corrections, and nonlocal gradient exchange corrections.[122,123] The molecular constants obtained from the calculation was in reasonable accord with the experimental data. The lanthanide contraction by the calculation was 5 pm for LnO.

From Mulliken population analysis, it is shown that the ionic character is enhanced in passing from LaO to LuO. From the f occupation numbers, a small f-orbital participation in bonding is present for LaO, whereas the 4f shell in LuO has core character. Ab initio pseudopotential study was conducted for Yb and YbO.[124]

The electronic structure of La_2O_3 was calculated to utilize the charges on atoms found in quantum chemical calculations. The calculation of the electronic structure was simplified by using the CNDO (complete neglect of the differential overlap) semiemprical scheme, which is derived from the LCAO approximation. The La_2O_3 was found to be a wide-gap insulator with a forbidden gap from 5.4 to 6.0 eV. The energy gap of La_2O_3 between the O2s and

O2p subbands is ~16.5−17 eV. The center of the O2p subbands is 4 eV under the Fermi level. The lower valence band in the La_2O_3 crystal is found to be formed by 2s O states, while the upper valence band is formed dominantly by 2p O states. The calculated density of states (DOS) for La_2O_3 shows a good agreement with the X-ray emission spectra. From the analysis of atomic charges, bond orders, and full atomic valencies in La_2O_3, the oxide was determined to possess mixed ionic−covalent bonding.[125]

The analyses of the spectra of 3d photoemission, valence photoemission, and BIS (bremsstrahlung isochromat spectroscopy) in Ce_2O_3* were carried out by a theoretical method; the filled band Anderson model provided information about the difference in the various spectra between Ce_2O_3* and CeO_{2-x}. Ce in Ce_2O_3* in the ground state is in the almost trivalent state. However, CeO_{2-x} is in the 3+ and 4+ mixed-valence state with 4f electron occupation around 0.4−0.5. 3d-XPS shows two peaks in the mixed states between the $4f^1$ and $4f^2$ configurations for Ce_2O_3* and three peaks, that is, one is from $4f^0$ configuration and the other two are by the mixed states of $4f^1$ and $4f^2$ configurations. From v-XPS, two peaks corresponding to the valence band photoemission and the 4f electron are obtained for Ce_2O_3* while a broad structure which is the result of the photoemission of the valence band appears in CeO_{2-x}. In BIS, one peak is obtained for Ce_2O_3* and two peaks for CeO_{2-x}. The former is made up of the $4f^2$ final state, the latter pair are due to the $4f^1$ and $4f^2$ final state.[126]

By analyzing 3d-XPS for Ln_2O_3 (R = La, Ce, Yb) and LnO_2 (R = Ce, Pr, Tb) with the impurity Anderson model, the covalent strength of the hybridization between rare earth 4f and oxygen 2p state was estimated. The splitting of the 3d-XPS was observed and two possible mechanisms were suggested. One is the initial-state hybridization for lighter rare earths such as La, Ce, Pr, and Nd, and the other is the final-state hybridization for Eu and Yb. Both of the initial- and final-state hybridizations are inevitable for the explanation of the 3d-XPS spectra for LnO_2 (R = Ce, Pr, Tb). The intraatomic multiplet coupling effect on 3d and 4d XPS was also carried out for La_2O_3, Ce_2O_3, Pr_2O_3, Nd_2O_3, Yb_2O_3, and CeO_2. Strictly, Ce_2O_3 and CeO_2 should be written as Ce_2O_3* and CeO_{2-x}. The theoretical study of X-ray absorption spectra (XAS) was done for rare earth sesquioxides and rare-earth dioxides.[127]

An all-electron, nonrelativistic computational study of bulk $CeO_{2.0}$ was done using the restricted Hartree−Fock periodic program CRYSTAL. The electronic characteristics were investigated for the ground state of $CeO_{2.0}$. From Mulliken electron populations, a charge transfer of 2.35e from cerium to the oxygen was identified. The value is smaller than the formal value of 4.0e. The nature is still considerably ionic. The insulating properties of $CeO_{2.0}$ indicate that four electrons from Ce fill the two O 2p orbitals. The HF (Hartree−Fock) band structure for CeO_2 is presented in Figure 24.[128] The O 2p symmetry dominates in the HF UV band with metal d character in the bottom UV band(s). The presence of f character in the bands does not apparently influence most ground-state properties, such as the lattice parameter. In the lower part of the valence band, metal 5p character is predominant. Partially covalent bonding is obvious between cations, also between cations and anions. The interaction between anion and anion is evident sufficient to be highly ionic.[128] The electronic structure was studied for the bcc heavy rare earth sesquioxides by the single site solutions within the renormalized atom model (RAM). This RAM is a valuable method to determine certain aspects of the electronic structure of semiconductors with narrow-band gap, when it is not simple to conduct a full band structure calculation.[129]

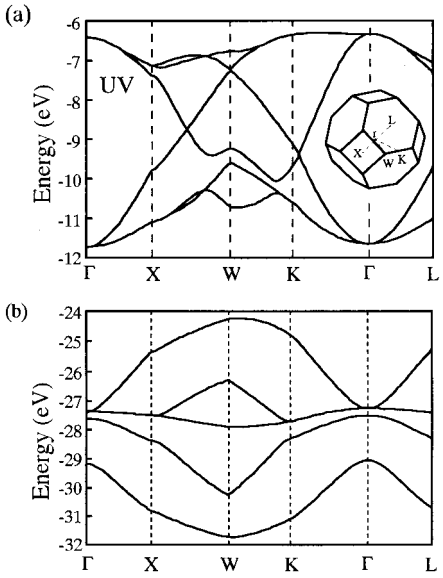

Figure 24. HF band structure for ceria. (a) Upper valence band for selected directions in reciprocal space. Inset denotes special symmetry points of the first Brillouin zone for an fcc lattice. (b) Lower valence band. The widths of the LV and UV bands are 8.86 and 5.80 eV, respectively. The intravalence gap is 11.25 eV, and the optical band gap (not shown) is about 16 eV. Bandwidths and band gaps are expected to be overestimated in the one-electron HF approximation. (Reproduced with permission from ref 128. Copyright 1993 Pergamon Press.)

The fully self-consistent band structure of CeO was investigated by using the linearized augmented plane-wave (LAPW) method. The band structures for the lattice constants a_1 for normal pressure and a_4 for high pressure, along with the major symmetry axes in the Brillouin zone were obtained (Figures 25[130] and 26[130]). The band structure is composed of the occupied O 2p band, a partially occupied f band, and the unoccupied s and d bands of Ce. The f bands, with the $\Delta_{2'}$ singlet lying lowest, are approximately 5 eV higher than the 2p-derived valence oxygen band. Both d and s bands form broad conduction ones. Therefore, the f bands are dipped in a sea of s−d conduction ones. The details are mentioned in ref 130.

The ionic and covalent characteristics of $CeO_{2.0}$ has been investigated from relativistic DV-Xα calculation.[131] The electron-deficient Ce 4f bands lie above the electron-occupied O 2p and this results in the stronger covalent bonding. Ce 5d orbital is located

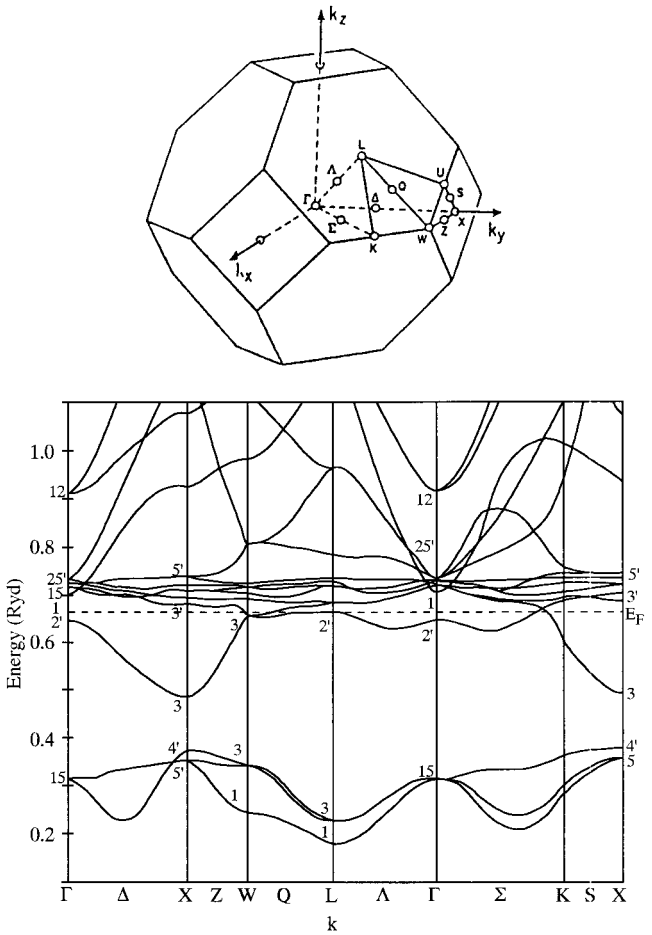

Figure 25. Band structure of CeO for the lattice constant a_1, along the symmetry points and axes. E_F is the Fermi energy. (Reproduced with permission from ref 130. Copyright 1989 IOP Publishing Ltd.)

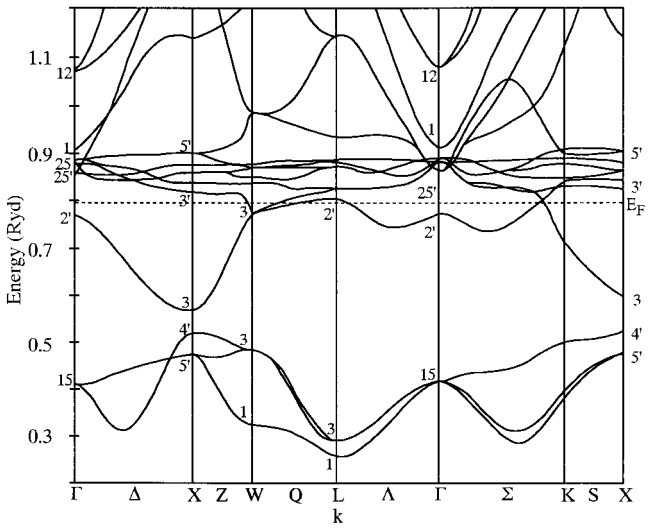

Figure 26. Band structure of CeO for the lattice constant a_4, along the symmetry points and axes. E_F is the Fermi energy. (Reproduced with permission from ref 130. Copyright 1989 IOP Publishing Ltd.)

higher than Ce 4f orbital. The space distribution of 4f orbital slightly bulges from 4f orbital and overlaps with O 2p and shows a covalent character. However, electrons fully occupy 5s and 5p orbitals and the Ce−O bonding becomes relatively ionic.

B. Band Gap

To investigate the dependencies of the lanthanides properties on the atomic number (Z) a suitable method is required to study the f specialty effect of the lanthanides. The band gap (E_g) is obtained from the vacant 5d (6s) conduction band and that which is the highest and fully occupied.

The optical E_g measurements were done for single crystals. The data for band gaps of oxides are listed in Table 7.[132] The tabulated values for the stoichiometric Ln_2O_3 are presently the most reliable. The variation of the band gap E_g with Ln in Ln_2O_3 is shown in Figure 27.[132] The most remarkable feature is the minimum exhibited by cerium. La, Gd, and Lu oxides show a maximum value of $E_g = 5.5$ eV. The E_g values for Ho, Er, and Tm oxides also exhibit similar values. Eu_2O_3 and Yb_2O_3 show less pronounced minima. The anomalous behavior is observed at the beginning for Ce and Tb, and at the end for Eu and Yb in the two halves of the lanthanoid series. The W-shaped curve with each V-shape composed of eight lanthanides with Gd, clearly shows the periodicity in the change of E_g. When the f band

Table 7. Band Gaps of Oxides[a] (Reprinted with permission from ref 132. Copyright 1966 Elsevier Science S. A.)

oxides	E_g (eV)
Ce_2O_3*	2.4
Pr_2O_3*	3.9
Nd_2O_3	4.7
Gd_2O_3	5.4
Tb_2O_3*	3.8
Dy_2O_3	4.9
Ho_2O_3	5.3
Er_2O_3	5.3
Tm_2O_3	5.4
Yb_2O_3	4.9
Lu_2O_3	5.5

[a] In Ln_2O_3*, the O/Ln ratio is thought to be almost equal to 1.5.

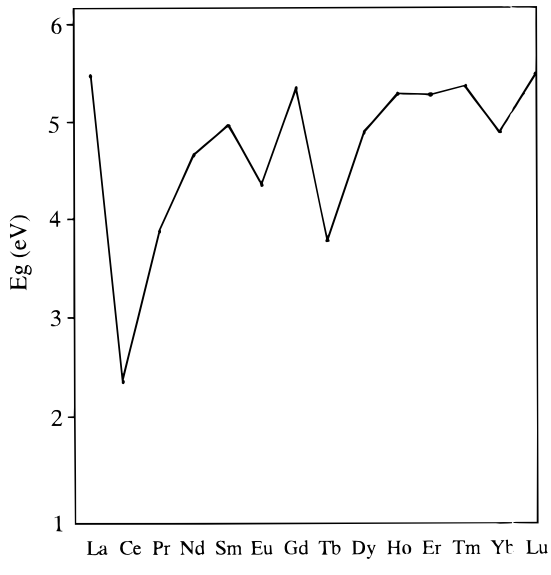

Figure 27. Variation of the band gap E_g of Ln_2O_3 in the lanthanoid series. (Reproduced with permission from ref 132. Copyright 1996 Elsevier Science S. A.)

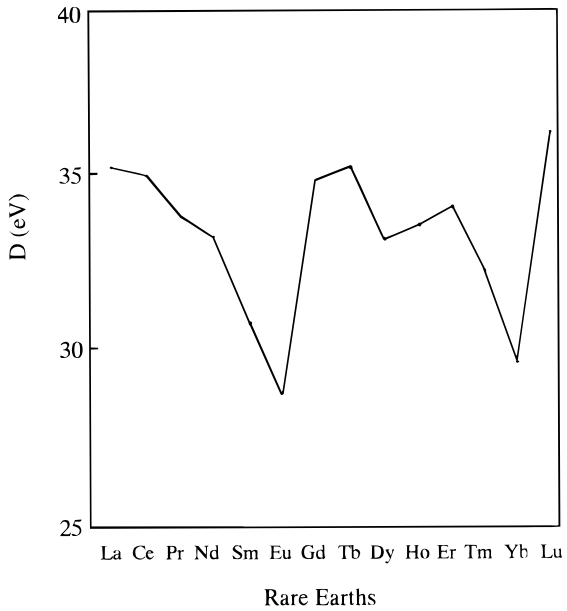

Figure 28. The dissociation (atomization) energy (D) variation of Ln_2O_3 in the lanthanoid series. (Reproduced with permission from ref 132. Copyright 1996 Elsevier Science S. A.)

lies in the forbidden gap, E_g is obtained by the f−d gap. If the f band drops down to the valence band and below it, E_g is obtained by the gap between the conduction and the valence bands. These two factors determine the periodic variation of E_g. The E_g for La, Gd, and Lu oxides shows maxima. In La^{3+}, the 4f level is empty and exists at a much higher level than the bottom of the 5d band. Since high stability is conferred by a half and fully filled 4f shell, the 4f-band position in the spectra of Gd and Lu oxides is more important than the 5d band. The 4f band for these oxides seems to exist deep in the valence band. The similar E_g value for the three La, Gd, and Lu oxides means that E_g is obtained from the same band gap between the conduction band and the valence band which is formed by 2p(O) states. The energy of 4f−5d transition is smaller than that for the rest of the series Ce, Pr, and Tb. The transition determines the absorption edge E_g of the Ce, Pr, and Tb oxides. E_g is strongly related with the energetic features of the chemical bond in crystals. The optical transition from the valence band (2p(O)) to the conduction band (5d6s(Ln)) possesses an interatomic character and can be regarded as a partial break in the Ln−O bond. In contrast, the transition from 4f to 5d (6s) is intraatomic. The former is greatly influenced by the bond energies and correlated with the dissociation (atomization) energy D. On the other hand, no correlation is observed in the relation E_g(Z) and D(Z) in which the band gap is obtained by the transition from 4f to the conduction band. However, there still remains a problem in the calculation of 4f energy level, since any discussion from relativistic quantum mechanics has not been taken into accounts.

The variation of the dissociation energy D of Ln_2O_3 in the lanthanide series is presented in Figure 28.[132] Both E_g(Z) and D(Z) show minima only for Eu and Yb. Therefore, it is concluded that the lower E_g for Eu and Yb oxides is determined by the narrower band gap between the 2p(O) and the conduction bands. The lower D value might be expected to occur as a result of the valency in the oxides decreasing from 3. No correlation was found for the minima of E_g(Z) and D(Z) for Ce and Tb. This strongly indicates that the 2p−5d transition is not the E_g determining factor, but that the 4f−5d transition is.

V. Physical and Chemical Properties

A. Electrical Properties

The conductivities of the rare earth sesquioxides become lower as the atomic number (Z) increase as presented in Table 8(oxygen pressure 0.2 atm)[133] and the oxides show p-type conduction. The exception is for Y_2O_3, which lies between Ho_2O_3 and Yb_2O_3. A break appears around 550−600 °C in the $\log \sigma - 1/T$ relation for most of the rare earth oxides. In contrast, the enhancement in the activation energy with an increase in Z was observed with an accompanying decrease in conductivity. Rare earth oxides show a considerable increase in ionic conductivity at higher temperature. The increase is expected to appear around, the inflection point mentioned above. For example, the ionic transference number (t_i) is estimated to be 0.5 for Gd_2O_3 at 1100 °C and a P_{O_2} of 10^{-3} atm, 0.5 for Dy_2O_3 at 1100 °C and 6.3×10^{-5} atm. The t_i value approaches 0.9 at 1200 °C and 10^{-7} atm. For Nd_2O_3, the electronic and ionic contributions to electrical conductivity were investigated. The dependency upon oxygen pressure was also studied, and it was concluded that the ionic conduction is due to oxygen vacancies.

The electrical conductivity of some of rare earth oxides is also presented in Figure 29 (oxygen pressure 0.2 atm).[133] The conductivity of rare earth oxides is, in general, low and especially low for the oxides of heavier rare earths. The conductivity decreases with the increase of atomic number of rare earths for Sm, Eu, and Yb, while the activation energy above the break temperature (T_B) increases. The onset of ionic conductivity causes the change in the slope of the conductivity−temperature plot at T_B. Rare earth sesquioxides are most probable to be mixed conductors in which major conducting species is electron with some contribution from ion. The conductivities

Table 8. Electrical Conductivity Data of Rare Earth Sesquioxides (R_2O_3) (Reprinted with permission from ref 133. Copyright 1970 Academic Press)

R	T_B[a] (°C)	E_1 (eV) ($T < T_B$)	E_2 (eV) ($T > T_B$)	$\sigma_{400°C}$ ($\times 10^{+9}$ Ω^{-1} cm^{-1})	$\sigma_{650°C}$ ($\times 10^{+9}$ Ω^{-1} cm^{-1})
La	270	0.7	1.05	230	1700
Pr	320	0.4	0.95	300	3450
Nd	−	−	1.15	25	1450
Sm	560	0.6	1.28	20	880
Eu	570	0.6	1.35	5	150
Gd	560	0.5	1.57	5	130
Tb	280	0.4	0.95	3	200
Ho	575	0.7	1.61	5	160
Yb	605	0.5	1.61	3	50
Y	−	−	1.10	−	55

[a] T_B is the break temperature in $\log \sigma - 1/T$ plots.

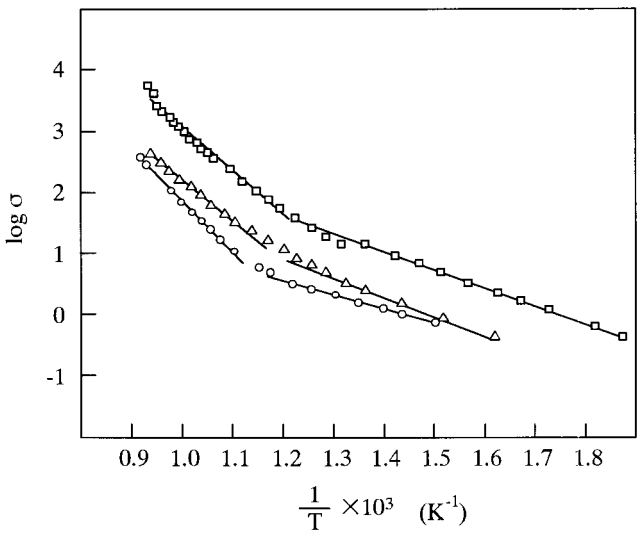

Figure 29. Plots of electrical conductivity (m Ω^{-1} cm^{-1}) against the reciprocal of absolute temperature ($p_{O_2} = 0.2$ atm) squares, Sm_2O_3; triangles, Eu_2O_3; and circles, Yb_2O_3. (Reproduced with permission from ref 133. Copyright 1970 Academic Press.)

of the rare earth oxides are reported to be in the range from 10^{-9} to 10^{-1} Ω^{-1} cm^{-1}.[133] Rare earth oxides with the composition of LnO_x ($1.50 < x < 1.75$) show p-type conducting characteristics. Except for praseodymium, rare earth oxides are found to be p-type semiconductors in the temperature range from 400 to 800 °C by Seebeck coefficient measurements. In contrast, the conduction becomes n-type above that composition and up to LnO_2. For LnO_x ($x > 1.5$), the extra oxygen occupies a lattice site and as a result holes (p-type) appear. On the contrary, for compositions close to LnO_2, most of the cations are Ln^{4+} with small amount of Ln^{3+} existing, the charge carriers are electron showing n-type conduction. As the oxygen content increases in Pr−O system, a change from p- to n-type conducting characteristics is observed at a composition of $PrO_{1.72}$. This is confirmed by the fact that a positive to negative change was recognized in the sign of Seebeck coefficient at $PrO_{1.72}$.[134]

The electrical conductivity in both Pr and Tb oxides becomes highest and the activation energy for conduction becomes lowest at $x = 1.75$, irrespective of whether phase is ordered of narrow homogeneity or disordered. The main reason for the maximum conductivity at $x = 1.75$ is ascribed to the stoichiometry (Ln^{3+} and Ln^{4+} concentrations) and not to the defect structure. From a consideration of the nonstoichiometric rare earth oxides to be electron hopping, the phenomenon that the conductivity in LnO_x becomes the highest about $x = 1.75$ can be calculated as is obtained experimentally.[133] Among LnO_x systems, the composition of $LnO_{1.75}$ seems to hold a random distribution of both Ln^{3+} and Ln^{4+} ions in such a manner to show a maximum electronic disorder. The mechanism of the conduction has been interpreted in terms of the hopping process[135] and of intermediate polaron theory.[136] In the rare earth sesquioxide series, the predominant defects seem to be fully ionized cation vacancies.

For the higher rare earth oxides, the compounds are complex and very sensitive to ambient conditions. Hopping-type electron conduction is predominant for the mixed-valence higher oxides. The minimum resistivity is obtained for R_7O_{12} (ι phase) which phase is well-known to form over a narrow composition region. The conductivity of the Pr_7O_{12} phase shows less dependence on oxygen pressure, because the oxide is compositionally stable in a much wider temperature region.

Since EuO has both intrinsic scientific interest and has potential commercial value, this lower oxide has been studied the most extensively among rare earth compounds. Electrical conductivity of EuO (regions I, II, and III in Figure 5) possesses similar insulating behavior. The most spectacular effect of the oxygen vacancies occurs between 69 and 49 K where the conductivity increases by 13 orders of magnitude. This insulator−metal transition is a characteristic property of samples obtained from region IV (Figure 5). In region V, the conductivity of EuO becomes metallic not only at high temperatures but also at low temperatures.

The electrical conductivity of Ce_2O_3* was measured and a clear break was observed at ~950 °C in the relation of $\log \sigma - 1/T$. The conduction mechanism is expected to be similar to that obtained for mixed-valence oxides by a kind of hopping-type conduction in the lower temperature range. In contrast, the conduction in Ce_2O_3* seems to be similar to other stable rare earth oxides in the higher temperature region.

Electrical properties of thin-film rare earth oxides have also been reported. The conductivity of praseodymium thin-film oxide was studied as a function of temperature and oxygen pressure.[137] The oxide film was shown to have p-type conduction above 630 °C and acted as a n-type semiconductor at the temperatures 400−630 °C. Thermally evaporated Eu_2O_3 thin film on a glass substrate is in an amorphous state. The predominant mechanism for ac conductance could be shown to be the result of a hopping type from the measurement of frequency dependence of the ac conductance.

The ac conductivity measurements were conducted for thin film Sc_2O_3 at temperatures from 4 to 295 K.[138] The conductivity was found to follow the relationship as $\sigma_1(\omega) = A\omega^s$, which is dependent on frequency and s depends on temperature and is a little smaller than unity. A model was proposed using a classical hop mechanism between randomly distributed localized states. The model was applied to scandium oxide with the assumption that the localized states are caused by lattice vacancies. In addition, the model seems to be applicable for situations where site potentials are similarly distributed. The characteristics of thin films of rare earth sesquioxides were reported by Gasgnier.[139]

In general, vacant site density is high in the deposited films. This facilitates the migration via atoms into vacancies, and results in a low activation energy. In Eu_2O_3 the conduction is explained by both oxide ionic conduction and electron hopping from Eu^{2+} to Eu^{3+} ions.[140] The rare earth oxide films of

scandium, yttrium, and lanthanum to lutetium were prepared by vacuum evaporation of the rare earth metal as a film followed by oxidation. The oxide films show insulating properties. The electrical resistivity was more than 10^{12} Ω·cm.[141] A similar deposition technique was also done for Er_2O_3 and the resistivity was approximately 10^{10} Ω·cm which was estimated from the ohmic region.[142] The conducting characteristics of Gd_2O_3, Dy_2O_3, Sm_2O_3, and Y_2O_3 between electronic and ionic has also been investigated by Tare and Schmalzried.[143] The electrical measurements were carried out for the oxides, and it was found that praseodymium and terbium oxides show semiconducting characteristics and that Ce, Nd, Eu, Gd, Dy, Ho, Er, Tm, Yb, and Lu oxides were dielectrics.[144] Considerable oxide ion conductivity has also appeared in these oxides. Dielectric properties of Dy_2O_3,[145−147] Yb_2O_3,[148] Dy_2O_3 and Yb_2O_3,[149] Er_2O_3,[150] and Nd_2O_3[151] have also been reported.

B. Magnetic Properties

Magnetic susceptibility measurements have been made extensively on the lanthanide oxides, mainly for the sesquioxides, such as Eu_2O_3, Gd_2O_3, and Dy_2O_3 over temperature from 300 to 1300 K and found to show a satisfactory accordance with Van Vleck's theory. For Eu_2O_3, good agreement was assured with Judds' energy levels for free Eu^{3+}. From the magnetic susceptibility measurements of single-crystal Dy_2O_3, Er_2O_3, and Yb_2O_3, the Néel temperatures becoming antiferromagnetic onset are found to be 1.2, 3.4, and 2.3 K, respectively. In the C-type rare earth sesquioxide, two sets of metal atom positions exist.[6] The coordination is in such a manner that each is coordinated by six oxygens instead of the eight for the corner cube in fluorite. Two of them are vacant across the face diagonal and this results in a C_2 site. For the other set of eight, the two oxygen vacancies exist at opposite ends of the body diagonal to yield a C_{3i} site. The magnetic structure of Er_2O_3 and Yb_2O_3 was determined. For Er_2O_3, the moments on the C_2 and C_{3i} sites are 5.36 ± 0.08 and 6.06 ± 0.23 μ_B, respectively. For Yb_2O_3, the moments corresponding to the C_2 and C_{3i} sites are 1.86 ± 0.06 and 1.05 ± 0.06 μ_B, respectively. The magnetic susceptibility of Ce_2O_3* was studied and found that the $1/\chi - T$ relationship followed the Curie−Weiss law. The results ($\theta_p = -90$ K, $\mu_{eff} = 2.44\ \mu_B$) are comparable to both theoretical and experimental data in the literatures.[50]

Some magnetic properties of the Sm, Nd, and Pr monoxides, produced at high pressures and temperatures, have been measured.[152] From the thermal variation of the susceptibilities and the lattice parameters for both NdO and PrO, a trivalent state of their metal atoms is identified. From the crystallographic and X-ray absorption data, on the other hand, Sm ion in SmO is expected to hold a nearly trivalent state.

EuO has an unusual characteristic of being ferromagnetic, with a Curie temperature of 77 ± 1 K.[153] Europium in EuO holds a divalent state contrary to other rare earth monoxides. Eu_3O_4, prepared by the solid-state reaction between Eu and Eu_2O_3, is ferrimagnetic, with a Curie point of 77 K.[154] Each mole of Eu_3O_4 possesses one Eu^{2+} ion and two Eu^{3+} ions. The praseodymium oxides with the compositions of $PrO_{1.50}$, $PrO_{1.72}$, $PrO_{1.83}$, and $PrO_{2.00}$[155] have been reported to be paramagnetic at higher temperatures and obey the Curie−Weiss law. The magnetic moments obtained were in good accord with the predicted theoretical value for the free ion. For $PrO_{2.0}$, prepared under 200 atm of oxygen pressure, antiferromagnetic ordering is reported to be observed with a Néel temperature of 14 K,[156] contradictory to the report by Kern.[155]

Terbium oxides of the composition of $Tb_{2.0}O_{3.0}$ (the B and the C forms), $TbO_{1.715}$, $TbO_{1.809}$, $TbO_{1.823}$, and $TbO_{2.0}$ have been studied from 1.4 to 330 K.[157] Predominant characteristics are their antiferromagnetic ordering, with Néel temperature of 2 and 7 K, respectively, for the B- and C-type sesquioxides and 7, 6, and 3 K for $TbO_{1.715}$, $TbO_{1.823}$, and $TbO_{2.0}$ while $TbO_{1.809}$ did not order above 1.4 K. At temperatures much higher than the ordering temperatures, the paramagnetic moment of the terbium is almost equal to the expected value from the free ion for abovementioned six kinds of terbium oxides. Terbium in $TbO_{2.0}$ has a magnetic moment of 6.25 ± 0.10 μ_B at 1.5 K. However, at 1.5 K, the total moment of Tb in $Tb_{2.0}O_{3.0}$ is 4.2 μ_B, appreciably lower than for the free ion. Neutron diffraction analysis has also been used to determine the magnetic structures of the rare earth sesqioxides.[158,159]

C. Spectroscopic Properties

All the stoichiometric oxides exhibit white or light pastel color except for $PrO_{2.0}$ and $TbO_{2.0}$ which are black or reddish-brown. The nonstoichiometric oxides of CeO_x, PrO_x, and TbO_x are dark bluish, black, and dark brown, respectively. The color of the oxides changes distinctly with a deviation from stoichiometry except for $PrO_{2.0}$ and $TbO_{2.0}$. The colors of the substoichiometric sesquioxides are all dark. Some optical properties have been reviewed by Eyring[6] and Röhler.[160] Absorption from the UV down to the near-IR has been measured for some praseodymium oxides (Pr_2O_3*−PrO_2*).[161] The spectra of the oxides varied in a regular way with an increase of the oxygen content which is in accord with the proposed phase relationship. The oxygen-rich EuO samples were characterized from infrared spectra and it becomes clear that it contains Eu_3O_4 as a secondary phase and Eu^{3+} existence in the solid solution.[27] The IR absorption reduced and then increased by increasing the Eu metal in the starting composition. The minimum point in the IR absorption is expected to be from the stoichiometric EuO. However, because of the excess Eu, oxygen vacancies were formed and a new absorption peak appeared.

The diffuse reflectance spectra of 11 rare earth sesquioxides have also been used for identification purpose.[162] Nondestructive qualitative analysis of trivalent rare earth ions can be done with the spectra in the near-infrared region. Since there is no partially filled f shells in La_2O_3(f^0 electronic configuration) and Lu_2O_3(f^{14} configuration), no absorption is expected in the region examined.

For EuO single crystals, a marked change was recognized in the position and sharpness of the transmission edge in the transmission (0.9−2.7 μm in wavelength) as each condition was varied in the temperature region (30−293 K) and magnetic fields up to 2.7 kOe. Optical absorption was observed for cerium oxide and praseodymium oxide by Haensel et al.[163] in the extreme ultraviolet range by using synchrotron radiation (light source the 7.5 GeV electron synchrotron DESY). The main part of the absorption is ascribed to the transitions from the 4d level of the rare earths. The absorption spectra of Ce and Ce oxide indicate a distinctly different character, while the absorption spectra of Pr and Nd are very close to those metals and their oxides.

The films of Pr oxides show transparent characteristics irrespective of the temperature deposited at room or higher temperatures. The transmittance of the Pr−O films was high around 90% and sometimes as high as 97% in the red region. The transparent nature indicates that the absorption edge lies in the UV region. The optical energy band gap (E_{opt}) was determined to be 3.4 eV from the relation between absorption coefficient and incident energy. The value was in good agreement with the approximate value obtained by the resistance change with temperature.[164]

Photoacoustic spectroscopy (PAS) technique was reported to be effective for investigating the kinetics and thermodynamics of intermediate phases of rare earth oxides and photochemical reactions of the surface of rare earth oxides.[165] Some information on the lattice structure of powder grains can be obtained from the spectra. Raman and resonance Raman spectroscopy was also studied on rare earth oxides such as Eu_2O_3, Dy_2O_3, and Tm_2O_3.[166]

Physical properties such as electrical, magnetic, or optical provide information for detecting small deviations from stoichiometric composition. The physical property measurements mentioned above are used not only with rare earth oxides but also with many other systems where variations in stoichiometry occur in compounds.

D. Atomic Transport Properties

The fluorite-related lanthanide oxides show unusual diffusion properties. Until one-half of the melting point temperature (the Tammann temperature) is achieved, atomic mobility in a solid does not become significant. In these oxides of rare earths, this value is about 1200 °C.[15] At the Tammann temperature, the metal atoms in lanthanide oxides just start to migrate in the solid as confirmed by the temperatures required for solid-state reactions. In the rare earth oxides, the metal substructure is rigid up to the melting point, and temperatures of 1200−1400 °C are necessary to obtain a reasonable metal atom migration in the lattice. However, the oxygen substructure becomes mobile far below the Tammann temperature, and in some cases even at the temperatures below 300 °C.

In the fluorite-related oxide systems, the smooth mobility of oxygen has been reported and data have shown that the oxide ionic transference number is unity at 971 °C.[167] The oxygen movement is even higher than that in the fluorite structure related to calcia-stabilized zirconia. Despite the high oxygen mobility in rare earth oxides at temperatures as low as 300 °C, the oxides are mostly thermally stable compounds, with melting points lying in the range around 2500 °C (see Figure 1). A rapid decrease in oxygen transport occurs as the atomic number of the lanthanide in the oxide increases. For example, the drop between lanthanum and erbium is by a factor of 10^2. Oxygen transport properties of rare earth oxides such as Nd_2O_3, Sm_2O_3, and Er_2O_3 was also employed by Eyring.[168]

The fluorite-related oxides with anion deficiency possess relatively high oxygen mobility. Isomorphs of rare earth oxide of the iota (ι) phase (R_7O_{12}) are in this category.

E. Single Crystals

There exists special problems in the growth of single crystals of lanthanide oxides. The oxides are insoluble in liquid solvents at normal temperatures and pressures. They possess high melting points (~2500 °C) and their congruent melting composition depends strongly on both the temperature and oxygen activity. To find suitable vapor transport reactions is a very difficult subject because of their high thermodynamic stability. Frequently, they have polymorphic transformation problems and fragment on cooling. In addition, the growth of crystals of higher oxides presents additional problems.

For growing crystals of substances which melt congruently and the substances do not possess such reconstructive phase transformations between the melting point and the temperature of interest, the flame fusion technique, e.g., the Verneuil method, has been successful. The flame originally used is $H_2 + O_2$, and it can be sometimes substituted for an argon plasma with an oxidizing or reducing condition controlled by adding either small amounts of oxygen or hydrogen.

At high pressure and temperature the solubility of many oxides becomes very appreciable in water or water with small amount of a mineralizer.[169] The growth of oxide crystals is promoted by temperature gradients or slow-cooling programs with or without pressure cycling. This method is of great interest in the growth of thermally unstable intermediate crystals and higher oxides. To grow crystals of the fluorite-related higher rare earth oxides, it is necessary that growth should be initially in the fluorite phase under conditions of very high oxygen fugacity and modest temperature. For example, the single-crystal growth of $PrO_{2.0}$, $Tb_{11}O_{12}$, $TbO_{2.0}$, and $CeO_{2.0}$ by this hydrothermal method is done in highly oxidizing conditions such as in the presence of HNO_3.[170,171] The optimum PrO_x:HNO_3 ratio was reported to be 1.0:1.0 by weight ratio. Nitric acid functions as a mineralizer to promote solubility and also as a source of oxygen. The pressure cycling is very effective for obtaining large crystals. This method is relevant for the other systems whose component is highly and thermodynamically active. The flux growth method has also been applied to

Table 9. Growth of Rare Earths Oxide Single Crystals (Reprinted with permission from ref 6. Copyright 1979 North-Holland Publishing Company)

crystal	method
EuO	melt
Y_2O_3	gas laser
CeO_2* [a]	flux
$PrO_{2.0}$	hydrothermal growth
Sm_2O_3 (B type)	verneuil
Eu_2O_3	flux
R_2O_3	verneuil

[a] In CeO_2*, the O/Ce ratio is thought to be almost equal to 2.

CeO_2*.[172,173] In this case, temperatures frequently investigated are in the range of 1300 °C.

As mentioned above, there are, in general, special problems in the growth of single crystals of the higher oxides. $CeO_{2.0}$ crystals are grown by a wide variety of flux growth methods. $PrO_{2.0}$ is obtained hydrothermally and $TbO_{2.0}$ has been prepared hydrothermally using perchloric acid as the oxidant.[174] Single crystals of the intermediate oxides are grown by adjusting their composition with annealing at appropriate temperatures and oxygen pressures. The sesquioxides of these three elements do not form in cubic symmetry by high-temperature methods, and the grown crystals shatter in the case oxidized to the fluorite-related, higher oxides.

The sesquioxides of all the lanthanides except Ce, Pr, and Tb can be formed from the molten state in air. The structure of the product obtained varies over the series. La_2O_3 and Nd_2O_3 are usually found to be in the A form, while Sm_2O_3, Eu_2O_3, and Gd_2O_3 are in the B form, and the remainder in the C form (see Figure 6). Similar results are obtained by using the Verneuil or flame fusion techniques. In all these methods, severe fracture problems appeared during cooling if the crystal form passes through any phase transformation. Some examples of crystal growth are tabulated in Table 9.[6] Single crystals of EuO have been grown from a melt of Eu and Eu_2O_3.[175]

In addition to the single-crystal growth, efforts to fabricate transparent polycrystalline rare earth oxides have also been successful by hot pressing. Press forging (950 °C, 681−817 atm for 48 h) can produce transparent Y_2O_3;[176,177] lithium fluoride is necessary to obtain full transparent pellets. Lithium fluoride that initially appeared was eliminated during the sintering process. Hot pressing method was conducted to prepare transparent Sc_2O_3[178] and Y_2O_3.[179] The sintering characteristics of Sm_2O_3, Eu_2O_3, Gd_2O_3, and Dy_2O_3 were studied both under oxidizing and reducing conditions and by hot pressing.[180] Among the sintered four kind of compacts, Dy_2O_3 was the most resistant to boiling water. No visible change was observed in the pellets held in boiling water for a week.

VI. Particles

A. The Characteristics of Fine Particles

In recent years, particles of ultrafine nanometer size have attracted much attention because of their unique physical and chemical properties that are substantially different from those of bulk materials. However, they are liable to aggregation, and their handling is very difficult because of their high surface energy and reactivity.

The academic interest is to prepare ultrafine particles which are not found in the bulk state and the following: (1) lower sintering temperatures, (2) smaller defect sizes for improved mechanical performance, (3) superplastic behavior for net shape forming.

Furthermore, a unique application such as providing a catalytic support for use in automobiles system is strongly expected. Some recent research practically on the preparation of fine particles are described in detail.

B. Fine Particles from Colloidal Medium

Monodispersed colloidal particles of lanthanide compounds are one starting medium for the preparation of fine particles of rare earth oxides. Cerium(III) forms crystalline oxydicarbonate ($Ce_2O(CO_3)_2 \cdot H_2O$) solids of ellipsoidal shape, while the other rare earth elements yield sols of amorphous spherical particles of basic carbonates. Solids prepared by the described procedure appear to be more suitable precursors for the preparation of rare earth oxides, because of the amorphous nature and spherical shape. In addition, a high yield (close to 100%) is also achieved. The metal hydroxycarbonates were readily converted to the corresponding oxides by calcination at 600 °C without any variation in morphology.[181]

Uniform colloidal spheres of rare earth compounds which contains yttrium, cerium, etc. by using forced hydrolysis or a slow release of hydroxide ions were also obtained from the decomposition of certain organic compounds such as formamide. The main purpose of the method is to establish a low-temperature chemical route for the preparation of homogeneous mixed rare earth oxides with spherical-shaped particles. The product obtained at 95 °C is identified to be amorphous from electron diffraction analysis. Calcining a quasistable $NH_4Y(C_2O_4)_2 \cdot H_2O$ salt is another method of obtaining a fine powder of yttrium sesquioxide.[182,183]

Colloidal dispersions containing spherical cerium dioxide of narrow size distribution (a mean diameter of 0.24 μm with a standard deviation $\sigma = 0.04$ μm) can be also prepared by hydrolytic deprotonation of cerium (IV) ions in the presence of diluted sulfuric acid.[184] Spherical and rodlike particles of narrow size distribution containing only yttrium and spherical particles of varying yttrium(III)/cerium(III) ratios, were prepared. Urea was used in the aging solutions. The initial molar ratio of urea to yttrium ion in solution affects the mean particle size. That is, the size increases with increasing the ratio.[185]

C. Fine Particles by Gas Condensation

The gas condensation technique is another approach in obtaining oxides with suitable particle shape. A stoichiometric nanostructured ceramic of Y_2O_3 with average particle size of 7 nm was prepared by this technique. The control of the microstructure,

which is one of special characteristics of the method, has a large impact on the properties of the consolidated material. The nanostructured Y_2O_3 aggregates can be easily dispersed in a solvent such as methanol and water to form a stable colloidal suspension. Only a few grain boundaries are formed during oxidation. The agglomeration is very weak and the majority of the pores is in a narrow range between 1 and 10 nm. During compaction, the weak agglomerates can be easily broken up into the individual particles. A high transparent form of the consolidated sample can be obtained because of this narrow pore size distribution. It is evident from the measurements of particles, grain, and pore sizes that the size of these microstructures is so small that little light scattering occurs.[186]

The phase transformation of the high-pressure monoclinic phase of Y_2O_3 to the cubic phase was studied by means of transmission electron microscopy.[187] Nanostructured (n-) metal oxides with particles sizes less than 10 nm can be prepared readily by gas condensation of metal nanoparticles followed by the subsequent postoxidation. The particle size grows during the annealing process. New diffraction rings, which belong to the cubic structure are observed after annealing at 700 °C. The transformation is caused by microstructural changes such a shape or size of the particles. Additional particle coarsening and a complete transformation to the cubic structure occurs after annealing at 875 °C. The average diameter of the particles is about 4 nm with a narrow distribution from 2 to 8 nm.[187] n-Y_2O_3 was also prepared by a two-step process combining gas condensation and postoxidation of Y nanoparticles, the average grain size of the as-prepared powder is 8 nm which was determined by dark field transmission electron microscopy.[188] The modification described as monoclinic γ-Y_2O_3, clearly different from the cubic phase, is known to be obtained by application of a hydrostatic pressure of 2.5 GPa at 1000 °C as the high-pressure modification of yttria.[60] A particle average size of 8 nm was determined from line broadening by using the Scherrer formula. By the Gibbs−Thomson effect, the presence at ambient conditions of the denser γ-Y_2O_3 can be readily explained. The grain sizes after the sintering in air at 300, 600, and 900 °C are 9, 13, and 33 nm, respectively. A clear phase transformation was observed from monoclinic (as compacted at 300 °C) to cubic (900 °C) with the presence of mixed phases at 600 °C. The material gradually shows a transition from monoclinic to cubic during the sintering process.[189] It is shown by an X-ray diffraction refinement method that, grain growth, migration of grain boundary, and phase transformation in nanostructured Y_2O_3 (n-Y_2O_3) occurs with an increase in temperature.[189]

Nanocrystalline cerium oxide was also formed by inert gas condensation of a metallic cerium precursor, followed by oxidation using a magnetron sputtering method. For the catalytic reduction reaction of SO_2 by CO, a reduction at 100 °C for 100% conversion is realistic compared to conventional CeO_2* catalysts.[190]

D. Fine Particle by the Sol–Gel Method

Cerium oxide powders of narrow size distribution with submicron range have been prepared by the method of spray drying of a sol obtained from cerium nitrate. Cerium hydroxide in the Ce^{3+} state is at first carefully precipitated. A crystalline size as small as 10 nm could be obtained by this method. As the precipitation reactions are conducted in a basic medium, the preparation of cerium oxide (CeO_2*) powder by the sol−gel method, starting from cerium nitrate and also taking care to control the oxidation state of cerium by a method different from the use of H_2O_2, was performed. The as-sprayed powder is in an amorphous state. The spray-dried powder retain the spherical shape after heating at 600 and 1100 °C. The particles were decomposed to form cubic cerium oxide with a crystallite size estimated from the XRD data to be in the nanometer range.[191]

The sintering processes of sol−gel prepared monodispersed submicrometer CeO_2 spheres was investigated by examining the microstructural changes of single spherical particles after successive heat treatment in oxygen up to 850 °C using TEM. CeO_2* particles were highly porous until they collapse at 850 °C.[192]

E. Fine Particles by Combustion Method

Flash combustion synthesis of cerium oxide is a solid-state combustion process based on the principle of explosive decomposition of nitrate−urea mixtures in a low-temperature range such as 500 °C. The powder can be consolidated to higher than 50% green density and sintering can occur at 1450 °C. The usual nucleation and growth factors of solution-phase reactions do not affect the products in this case. The average particle size of the cerium oxide obtained by flash combustion is about 1 μm.[193]

The large surface area of 55 $m^2 \cdot g^{-1}$ could be attributed to the evolution of residual gases retained during the initial flash reaction and an average radius of micropores is 1 nm. The powder prepared at 800 °C was stable up to 1000 °C. Micrometer-sized cerium oxide powder could be prepared by a very simple and fast method from a mixture of cerium nitrate and urea. One of the possible applications of the powder is a catalyst support in automobiles.[194]

Another preparation of fine particle, large surface area ceria by the combustion process has been developed.[195] This is a rapid decomposition process of a saturated aqueous solution containing ceric ammonium nitrate and urea, carbohydrazide, oxalyl dihydrazide or tetraformal triazine redox mixtures. Approximately 80% of the particles are smaller than 10 μm. The average agglomerate size of CeO_2* is changing between 0.61 and 1.28 μm. The redox reaction is considerably exothermic with the evolution of gases such as nitrogen, H_2O, and CO_2. The gas evolution acts to disintegrate the product in addition to dispersing the heat of combustion. As a result, sintering is highly inhibited.

F. Fine Particles by the Spray-ICP Technique

In the spray-ICP technique the rare earth oxides are quenched at an early stage of crystal growth from

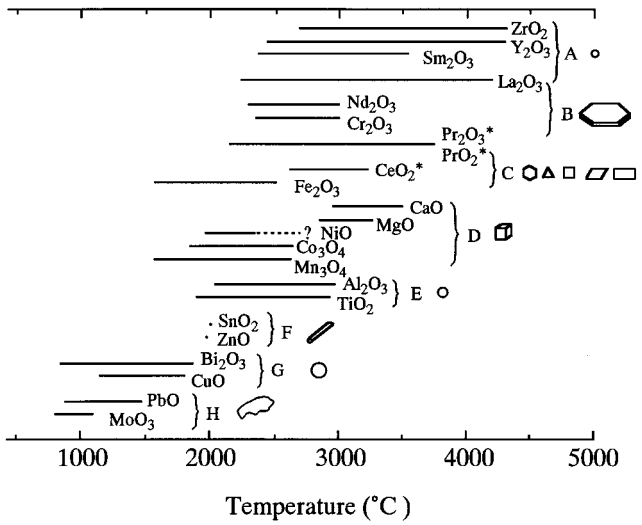

Figure 30. Particle morphology and temperature variations between boiling and melting points of oxides. (Reproduced with permission from ref 197. Copyright 1992 Chapman & Hall.)

the gas phase. Therefore, the mean diameters of the spherical particles ranged from 15 to 35 nm.[196] Because a high-temperature rf inductively coupled plasma (ICP) is electrodeless, it can be operated in reactive gases, such as oxygen and halogen, and also at high temperatures. Products, can also be obtained free from the contamination of electrode materials by this technique.

The particle morphology and temperature differences between bp and mp of the oxides including rare earth oxides are shown in Figure 30.[197] The La_2O_3 particles were prepared in a spherical shape, but a few anomalously large hexagonal plates were also present. The boiling point (bp) difference among rare earth oxides affects the particle morphology. La_2O_3 and Y_2O_3, having almost the same high bp (see Figure 30) can be obtained as spheres. Nd_2O_3 which shows a much lower bp produced mainly plates with a small amount of cubes. La_2O_3 deposits faster than Nd_2O_3, without forming the plates, because of its high bp.[197] The powder of the Pr−O system is obtained as two phases, i.e., Pr_2O_3* and PrO_2*. Pr_2O_3* and PrO_2* represents the praseodymium oxide with the Pr/O ratio almost equal to $^2/_3$ and $^1/_2$, respectively. From TEM analysis, it is shown that they were composed of both plates and polyhedra. The former was found to be Pr_2O_3* and the latter was PrO_2*. The oxides of A-type rare earths (hexagonal La_2O_3, Nd_2O_3, Pr_2O_3*) have a tendency to form plates, while those of the cubic fluorite type (CeO_2*, PrO_2*) grow to form polyhedra. However, further investigation is necessary to establish this criterion.

G. Fine Particles by Other Methods

Reactive CeO_2* powders have been prepared by the homogeneous precipitation method. CeO_2* powders have been synthesized by aging a cerium(III) nitrate solution with hexamethylenetetraamine. Oxidation of Ce^{3+} occurs in the precipitate and the wet precipitate is crystallized to CeO_2* before any heat treatment. The dried CeO_2* powders can be easily sintered, and a full density state can be obtained at temperatures below 1300 °C with or without calcination. Particle size does not affect the oxide sinterability. Direct CeO_2* formation by precipitation is believed to decrease the chance of forming solid−solid interaction between particles during calcination and reduce the sintering.[198] The surface chemistry of nanometric ceria particles in aqueous dispersions was studied by Nabavi et al.[199]

From TEM measurements, the ultrafine CeO_2* powder obtained by hydrothermal synthesis was found to possess a faceted polyhedral morphology. The particles are also uniform in size. The particle size distribution obtained by calculation of the measured maximum diameters of more than 100 particles in TEM micrographs was very narrow. The average particle size was calculated to be 14 ± 3 nm, which is close to being consistent with the average size (12 nm) obtained from X-ray line broadening. The rate of densification increases significantly with a reduction of powder particle size.[200]

Rare earth isopropoxides (La, Ce, Gd) were prepared by refluxing the corresponding chlorides in isopropyl alcohol. The solutions were dried by either the vacuum, spray, or freeze method, and the resulting hydroxides were heat treated to form the corresponding oxides. In these methods, relatively large, uniform, and spherical particles were, in general, obtained by spray drying. Pure and size-controlled oxide powders were formed by drying and subsequently calcining the rare earth hydroxides obtained by hydrolysis of the isopropoxides.[201]

In addition to the fine particles of CeO_2*, those for La_2O_3 and Er_2O_3 were also reported. La_2O_3 ultrafine particles were synthesized by a homogeneous precipitation method. La_2O_3 ultrafine particles with a size less than 0.04 μm were obtained by drying the precipitate in an oven, using urea as the hydrolytic agent.[202]

The ultrafine particles of Y_2O_3, whose average sizes were estimated to be approximately 60−70 nm, were prepared by using $YCl_3 \cdot 6H_2O$ (>99.9% purity) and urea for starting material and precipitant, respectively.[203]

Nanocrystalline erbium oxide was also prepared by a chemical method from the nitrate precursor.[204] The grains are monodisperse and about 20 nm in size. An important grain growth is observed between 1450 and 1475 °C. The sintering rate is higher for a fine grain powder than for a micrometric one as would be expected.

Among the rare earth oxides, $CeO_{2.0}$ is well-known as an abrasive, an ultraviolet absorbent, and an automotive exhaust catalyst. Some properties such as sinterability, specific surface area, and catalysis using the particles have been characterized. However, optical properties have not been examined, and it seems very important to characterize them in this way to identify any specificity based on ultrafine particle size.

The relaxative autodispersion (RAD) process is based on the thermal relaxation process of the Nylon 11 film prepared by vacuum deposition. When a cerium metal film, laminated by vacuum deposition

on a Nylon 11 film and in a thermodynamically metastable state, was heat treated at a temperature between glass transition point and the melting point, cerium metal was dispersed into the nylon matrix in the form of ultrafine metal particles.[205,206] The cerium metal ultrafine particles became oxidized to cerium oxide because rare earth metals in air are easily oxidized.

In the case of the sample containing 1.3 vol % cerium oxide, a particle size distribution between 1 and 8 nm and of mean particle size of 4.1 nm was estimated. For the sample containing 11.8 vol % cerium oxide the particles size distribution was between 2 and 20 nm and the mean particle size was 5.8 nm. The mean size of the particles in the composite film was dependent on the metal content. That is, the particle size became smaller when the content of cerium metal decreased.

The direct band gap value for the composite contained 4.1 nm particles was 3.42 eV and that with 5.8 nm particles was 3.37 eV. No size quantization effects seemed to appear in the spectral properties of CeO_2* fine particles. This may be due to the fact that the size distribution was relatively large and that the mean particle size was not small enough to develop the necessary change in its band structure.

During heat treatment of a metal−polymer laminated film, the upper metal layer is pulverized and finely divided into the ultrafine particles in the course of relaxation by the lower polymer layer. The affinity of the stationary metal phase on the film before the heat treatment will be proportional to the film thickness. The thin metal layer on the polymer matrix was dispersed much more easily than the thick one. As a result, the sizes of the ultrafine particles obtained by the RAD process become smaller as the thickness of the metal layer is reduced.

From the selected-area electron diffraction (SAED) patterns, the resultant material was completely indexed as those of $CeO_{2.0}$ with the cubic fluorite structure, and the lattice parameter calculated from the radii of Debye−Sherrer rings was 0.541 nm which is in good accord with that given in the literature.

In addition, a new wet process which utilizes reversed micelles as a reactor has succeeded in producing ultrafine and monodispersed nanoparticles. In water-in oil microemulsions, the aqueous phase such as water, aqueous solutions of metal salts, and ammonia water, can be soluble within reversed micelles. Since, these nanosize aqueous droplets surrounded with surfactant molecules can continuously exchange their content with one another when they collide,[207−210] several chemical reactions are possible within the reversed micelles.[211] The particles are very small and have a narrow size distribution because the reaction space is limited to within the reversed micelles. Once the particles grow to a critical size, the surfactant molecules surrounding them function to cease further growth. Monodispersed $CeO_{2.0}$ ultrafine particles with the mean size of 2.6 nm were synthesized by this method.[212]

VII. Thermodynamic Properties

A. Gaseous Rare Earth Oxide Species

Gaseous rare earth oxide species of the general formulas, RO, R_2O, RO_2, and R_2O_2 (where R denotes the rare earth atom), have been observed.[213] Of these, the monoxides (RO) are those which have been investigated most extensively.[214] The data for other oxide species were reported by Gingerich.[215]

The rare earth sesquioxides have been commonly assumed to vaporize congruently with a composition in almost stoichiometric ratio. One of the earliest systematic studies of the lanthanide monoxides was done by White et al.[216]

At high temperatures, in addition to monoxides, other gaseous species of the formulas, R_2O, RO_2 and R_2O_2, have also been observed as minor species in the rare earth−oxygen systems. They are ∼2−3 orders of magnitude less abundant than either the monoxide or the metal atom species. The most extensive study concerning these polyatomic oxides was reported by Kordis and Gingerich.[217]

The thermochemical and thermophysical properties of the rare earth sesquioxides were critically assessed in 1973[218] and a systematic comparison between rare earth and actinide sesquioxides was published by Morss.[219] Here, a systematic treatment of the thermochemical properties of the oxides were done. Figure 31 indicates the enthalpy of solution of Ln_2O_3 as a function of molar volume.[219] From the figure, the enthalpies of solution of Ln_2O_3 were found to become less exothermic in going from the light to the heavy rare earths as the molar volume reduces with the lanthanide contraction. From the electrode potential data for aqueous ions, the stability of Ln^{2+} ions (for the reaction $2Ln^{3+}(aq) + Ln(s) \rightarrow 3Ln^{2+}(aq)$) lowers in the sequence Eu (−475), Yb (−344), Sm (−212), Dy (−38), Tm (−12), Nd (+87), and Pm (+108), where $\Delta G_0°$ (in kJ/mol) is described in parentheses). The value for the reaction $Eu_2O_3(s) + Eu(s) \rightarrow 3EuO(s)$ is only −113 kJ/mol, for Yb^{2+} is 18 kJ/mol. Samarium and other rare earths in a divalent state should be even more difficult to produce.

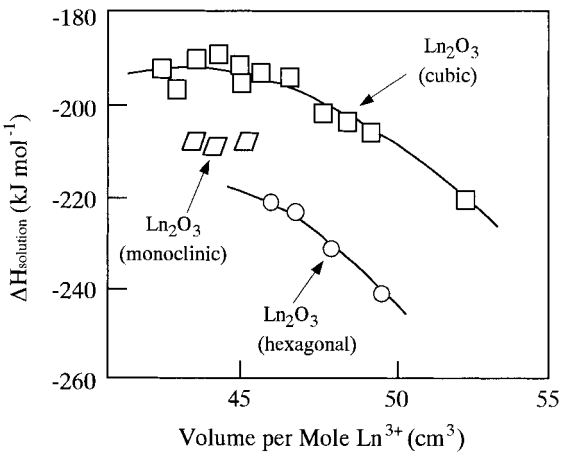

Figure 31. Enthalpy of solution of Ln_2O_3 as a function of molar volume. (Reproduced with permission from ref 219. Copyright 1983 Elsevier Sequoia.)

Table 10. The Standard Enthalpies of Formation ($\Delta H_f°$) of Gaseous Rare Earth Atoms and the Homonuclear Diatomic Molecules (kJ/mol) (Reprinted with permission from ref 213. Copyright 1989 Elsevier Science Publishers B. V.)

rare earth element, R	$\Delta H_f°$ (R, g, 298 K)	$\Delta H_f°$ (R, g, 0 K)	$D_0°$ (R_2)
La	431.0 ± 2.1	431.4 ± 2.1	243 ± 21
Ce	420.1 ± 2.1	420.7 ± 2.1	238 ± 21
Pr	356.9 ± 2.1	358.0 ± 2.1	126 ± 29
Nd	326.9 ± 2.1	327.8 ± 2.1	80 ± 29
Sm	206.7 ± 2.1	206.1 ± 2.1	50 ± 21
Eu	177.4 ± 2.1	177.4 ± 4.1	29 ± 17
Gd	397.5 ± 2.1	399.0 ± 2.1	172 ± 33
Tb	388.7 ± 2.1	390.7 ± 2.1	128 ± 25
Dy	290.4 ± 2.1	293.0 ± 4.1	67 ± 29
Ho	300.6 ± 2.1	302.0 ± 2.1	82 ± 30
Er	316.4 ± 2.1	317.6 ± 4.1	71 ± 29
Tm	232.2 ± 2.1	233.4 ± 4.1	50 ± 17
Yb	155.6 ± 2.1	156.1 ± 2.0	17 ± 17
Lu	427.6 ± 2.1	427.8 ± 4.1	138 ± 33
Y	421.3 ± 4.1	420.4 ± 2.1	156 ± 21
Sc	377.9 ± 4.1	376.0 ± 4.1	159 ± 21

The enthalpy change for the reaction (Ln(s) + $^1/_2O_2$(g) → LnO(g)) was calculated, and it was shown that the gaseous monoxides of the lighter lanthanides were considerably more stable than those of heavy lanthanides. The reason is that the gaseous atoms ($f^n s^2$) in the light lanthanide atoms are considerably more accessible than those in the heavy lanthanide atoms to bond effectively to oxygen, in other words, promotion to a bonding state. The thermodynamic properties of europium oxides were evaluated by Rard[220] and the enthalpy of Y_2O_3 formation was redetermined by combustion calorimetry[221] and also by solution calorimetry.[3]

The lanthanide monoxides have been most widely studied from the thermodynamic point of view. Most of the thermodynamic results have been obtained from investigation of high-temperature vaporization of the solid oxides. As the primary experimental method, high-temperature Knudsen effusion mass spectrometry had been used. Either pure sesquioxide (R_2O_3) or a mixture of sesquioxide and the corresponding metal (R_2O_3+R) had been used to produce a vapor source of the monoxide. The sesquioxides vaporize mainly according to the following reaction:

$$R_2O_3(s) = xRO(g) + (2-x)R(g) + (3-x)O(g) \quad (0 < x < 2.0)$$

The standard enthalpies of formation of gaseous atoms are given in Table 10,[213] and the corresponding values for the $\Delta H_f°(R_2O_3, s)$ are tabulated in Table 11.[213]

The Gibbs energy functions for the monoxides were recalculated by the model suggested by Murad and Hildenbrand[222] and the values are listed in Table 12.[213] The values reported by Murad and Hildenbrand are somewhat different from those given by Ames et al.,[223] but are in good accord with the values evaluated by Ackermann and Chandrasekharaiah.[224] The dissociation energies, $D_0°$(RO, g), and the standard enthalpies of formation, $\Delta H_f°$(RO, g, 0 K) of rare earth monoxides have been recalculated using the values in Tables 10 and 11.

Table 11. The Standard Enthalpies of Formation of Rare Earth Sesquioxides[a] (Reprinted with permission from ref 213. Copyright 1989 Elsevier Science Publishers B. V.)

R_2O_3(s)	$-\Delta H_f°$ (298 K)	R_2O_3(s)	$-\Delta H_f°$ (298 K)
La_2O_3	1794 ± 4.0	Dy_2O_3	1863 ± 12
Ce_2O_3*	1796 ± 4.0	Ho_2O_3	1881 ± 8
Pr_2O_3	1824 ± 2.5	Er_2O_3	1898 ± 4
Nd_2O_3	1808 ± 5.0	Tm_2O_3	1889 ± 10
Sm_2O_3	1828 ± 10	Yb_2O_3	1814 ± 6
Eu_2O_3	1652 ± 10	Lu_2O_3	1871 ± 20
Gd_2O_3	1816 ± 16	Y_2O_3	1905 ± 6
Tb_2O_3*	1846 ± 20	Sc_2O_3	1906 ± 6

[a] In Ln_2O_3*, the O/Ln ratio is thought to be almost equal to 1.5.

Table 12. The Gibbs Energy Functions and the Electronic Statistical Multiplicities for the Rare Earth Monoxides (Reprinted with permission from ref 213. Copyright 1989 Elsevier Science Publishers B. V.)

monoxide	electronic multiplicities	$-(G_T° - H_0°)/T$ (J K^{-1} mol^{-1}) 2000 K	2200 K	2400 K	2600 K
LaO	2	271.83	275.22	278.28	281.16
CeO	6	280.37	284.09	287.15	289.99
PrO	8	283.47	286.86	289.95	292.80
NdO	10	285.52	288.91	292.00	294.85
SmO	12	287.57	290.91	294.01	296.85
EuO	16	290.12	293.47	296.56	299.41
GdO	9	285.73	289.07	292.17	295.01
TbO	20	292.50	295.89	298.95	301.79
DyO	12	288.53	291.92	294.97	297.82
HoO	12	288.74	292.09	295.18	298.03
ErO	10	287.40	290.58	293.84	296.69
TmO	8	285.68	289.03	292.13	294.97
YbO	6	280.59	286.94	290.03	292.88
LuO	2	274.51	277.90	280.96	283.80
YO	2	265.89	269.24	272.34	275.18
ScO	2	260.58	263.54	266.28	268.85

Table 13. The Enthalpy of Formation ($\Delta H_{f,0}°$) and the Dissociation Enthalpies ($D_0°$) of Rare Earth Monoxides (kJ/mol) (Reprinted with permission from ref 213. Copyright 1989 Elsevier Science Publishers B. V.)

monoxide	$-\Delta H_{f,0}°$	dissociation enthalpy, $D_0°$
LaO	121.0 ± 10.0	795 ± 9.6
CeO	117.0 ± 20.9	790 ± 17
PrO	133.9 ± 12.5	745 ± 9.5
NdO	125.5 ± 12.5	706 ± 12.5
SmO	117.0 ± 12.5	569 ± 9.6
EuO	46.0 ± 12.5	465 ± 15
GdO	66.9 ± 12.5	711 ± 12.5
TbO	54.4 ± 20.9	693 ± 21
DyO	75.3 ± 20.9	607 ± 21
HoO	54.4 ± 12.5	613 ± 9.6
ErO	37.7 ± 12.5	607 ± 9.6
TmO	31.4 ± 20.9	508 ± 9.6
YbO	−2 ± 21	401 ± 21
LuO	−8.4 ± 12.5	663 ± 9.6
YO	46.0 ± 9.6	715 ± 10
ScO	54.4 ± 10	676 ± 10

These recalculated values with some of the previous data are also shown in Table 13.[213] The data of $D_0°$(RO) have been mainly obtained by Pedley and Marshall.[214] Bonding in these oxides has been described with a certain amount success in terms of the $R^{2+}O^{2-}$ ionic configuration. However, the nature of

the bonding in these monoxides is not fully characterized.

The dissociation energies of these monoxides, $D_0°$(RO, g), change rather nonmonotonically with atomic number increase from La to Lu (Figure 32[213]) showing the "double periodicity" similar to the enthalpy of formation of the gaseous metal atoms. Since the nonmonotonic $D_0°$ change closely parallels the variation in the promotional energy of the $4f^n \rightarrow 4f^{n-1}5d$ electronic transitions, the excitation energy of the transition plays an important part in determining the energetics of the lanthanide monoxide bonds. A close similarity of the ionization potentials of the lanthanide metals and their monoxides has been also observed.[225]

All of the gaseous monoxides except CeO(g) and most of the gaseous atoms were produced from the vaporization of the solid lanthanide sesquioxides. In most cases, both species were produced at comparable pressures. The variations in the first ionization potentials of the atoms and monoxides of Ba, La, the lanthanides, Ta, and Hf are presented in curves a and b in Figure 33.[225] For La and the light members of the Ln sequence the value of the monoxides are smaller than those of the metals. But the trend reverses for Eu and the members beyond Tb. A further understanding of this behavior can be attained from a consideration of the following thermodynamic cycle:

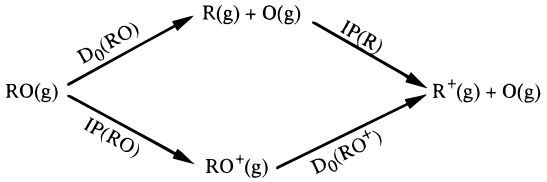

From which we can obtain the equation

$$D_0(\mathrm{RO}) - D_0(\mathrm{RO}^+) = \mathrm{IP(RO)} - \mathrm{IP(R)}$$

In the light lanthanides, the ionized monoxides are more strongly bonded than the neutral oxides and conversely for the heavier members of the sequence. The ionization potentials, IP(R) and IP(RO), lie generally within 0.5 eV of each other. For La and the early members of the lanthanide sequence, the IP value of the monoxides is smaller than that of the metals. However, for the europium and the rare earth oxides members beyond terbium, the trend becomes reversed. The dissociation energies of the monoxide ions are directly related to those of the neutral monoxides [$D_0(\mathrm{RO}^+) = D_0(\mathrm{RO}) + \mathrm{IP(R)} - \mathrm{IP(RO)}$]. Therefore, the values of $D_0(\mathrm{RO}^+)$ will also show a similar double periodicity. In the light lanthanides, the ionized monoxides are more strongly bonded than the neutral oxides.

Ames et al. carried out the first comprehensive thermochemical study of these monoxides using a combination of Knudsen effusion and mass spectrometric isomolecular oxygen-exchange reactions.[223]

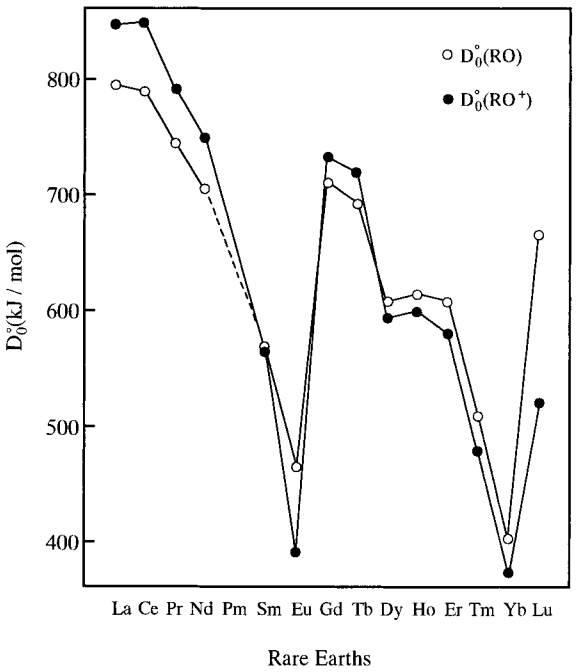

Figure 32. Dissociation enthalpies of lanthanoid oxides and ions. (Reproduced with permission from ref 213. Copyright 1989 North-Holland Publishing Company.)

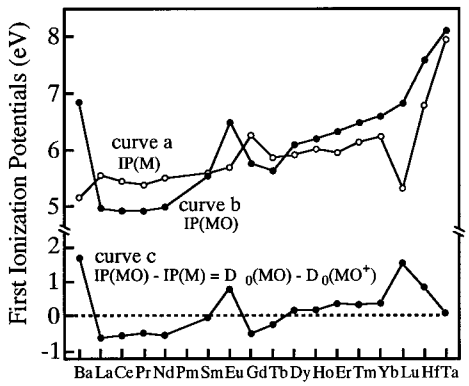

Figure 33. The first ionization potentials of the gaseous atoms and monoxides for elements 56−73; curve a, M(g); curve b, MO(g); and curve c, the systematic behavior across the lanthanoid sequence relating the difference in ionization potentials of the monoxides and metals with the dissociation energies of MO(g) and MO^+(g). The electronic configurations beyond $5p^6$ are shown for the neutral gaseous atoms. (Reproduced with permission from ref 225. Copyright 1976 American Institute of Physics.)

Oxygen-exchange reactions of this type are described as follows:

$$\mathrm{R_a(g) + R_bO(g) = R_aO(g) + R_b(g)}$$

where R_a and R_b are the two rare earth metals, studied.

The dissociation energies, $D_0°$, of the gaseous rare earth monoxides derived from this experiment are summarized in Table 14.[223]

Values obtained from third-law treatment of the Knudsen effusion data are shown first. The average of the determinations of $D_0°$ for each monoxide is given in the same table. The dissociation energies of the gaseous rare earth monoxides change consider-

Table 14. Dissociation Energies ($D_0°$) of Gaseous Rare Earth Monoxides (in eV) and Heats of Formation ($\Delta H_0°$, kJ/mol) (Reprinted with permission from ref 223. Copyright 1967 American Chemical Society)

	source				
		isomolecular reaction			$-\Delta H_{f0}$
monoxide	effusion	2nd law	3rd law	average	(kJ mol^{-1})
ScO	7.10	7.17	7.20	7.16	66.1
YO	7.43	7.39	7.53	7.45	48.1
LaO	8.33	–	–	8.38	131.0
CeO	–	8.36	8.40	8.38	93.3
PrO	–	7.75	8.01	7.88	139.3
NdO	7.43	7.45	7.55	7.48	154.4
SmO	5.94	6.24	6.31	6.16	144.3
EuO	5.84	–	5.75	5.80	136.8
GdO	7.39	7.62	7.49	7.50	74.5
TbO	–	7.61	7.43	7.52	83.7
DyO	6.52	–	–	6.52	84.1
HoO	6.54	–	6.71	6.62	99.6
ErO	6.58	–	–	6.58	71.5
TmO	6.04	–	–	6.04	87.0
YbO	≤3.83	–	–	≤3.83	≥−30.1
LuO	7.07	7.33	7.28	7.23	23.0

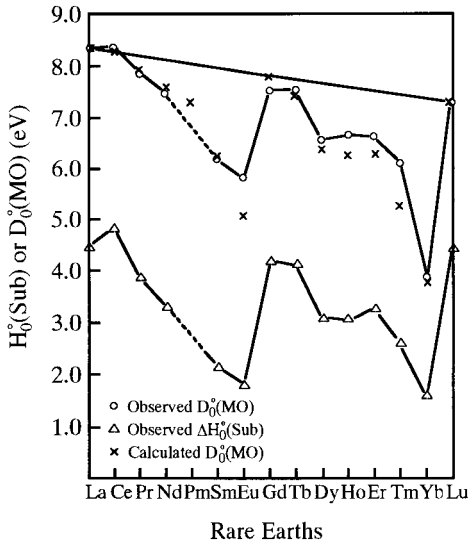

Figure 34. Variation of dissociation energy of the gaseous monoxides and heat of sublimation of the lanthanoid metals with atomic number. (Reprinted with permission from ref 223. Copyright 1967 American Chemical Society.)

ably with atomic number. This variation shows a typical double periodicity in going from lanthanum to lutetium as shown in Figure 34.[223]

A striking correlation is observed when the variation in dissociation energies is compared with the heats of sublimation of the metals, which are also shown in the same figure. The dissociation energies and the heats of sublimation correlate in an identical manner with atomic number. There is some similarity between these two processes, of the rare earth atom changing from the bound states, solid metal, and gaseous monoxide, to the free atom. An explanation for the variation of the monoxide dissociation energies should be in accord with that for the heats of sublimation of the metals.

There seems to be two factors contributing to the variation of dissociation energies of the lanthanide monoxides. The first is a relatively minor effect, such as lanthanide contraction and is shown by the small variation in the heats of formation. The more important second contribution, which results in the large periodic fluctuations in both the dissociation energies of the monoxides and the heats of sublimation of the metals, is likely to be related to the filling of the 4f orbitals of the lanthanides.

Only rare earths of La, Ce, Gd, and Lu, whose lanthanoids show the largest dissociation energies and heats of sublimation possess a 5d electron in the ground electronic state of the free atoms. When any rare earth metal with a 5d electron in the metallic conduction, but not in the ground electronic configuration of the free atom band vaporizes, the electron would drop from the 5d level to the lower 4f orbital. As the dissociation energies of the monoxides and the heats of sublimation of the metals show the same trends with atomic number increase, the change in the electronic structure of the atoms is proposed to be identical in the dissociation and sublimation processes. The periodic changes in dissociation energies are thus explained by changes in the relative energies of the 4f and 5d levels with atomic number.[223]

Table 15. Atomization Energies of the Rare Earth $R_2O(g)$, $RO_2(g)$, and $R_2O_2(g)$ Molecules (Reprinted with permission from ref 217. Copyright 1977 American Institute of Physics)

	$\Delta H_0°$ (kJ/mol)			
rare earths	R(s) = R(g)	$R_2O(g) = 2R(g) + O(g)$	$RO_2(g) = R(g) + 2O(g)$	$R_2O_2(g) = 2R(g) + 2O(g)$
Sc	376.1 ± 4.2	987.4 ± 66.9	(1280.3 ± 92.0)	(1736.4 ± 117.2)
Y	423.8 ± 2.1	1041.8 ± 54.4	(1351.4 ± 92.0)	1832.6 ± 117.2
La	431.4 ± 4.2	1108.8 ± 54.4	(1518.8 ± 92.0)	1920.5 ± 117.2
Ce	423.0 ± 12.6	(1167.3 ± 75.3)	1439.3 ± 20.9	1974.8 ± 62.8
Pr	356.9 ± 2.1	(1092.0 ± 75.3)	(1414.2 ± 92.0)	(1920.5 ± 117.2)
Nd	328.4 ± 2.1	(1020.9 ± 75.3)	1330.5 ± 83.7	(1790.8 ± 117.2)
Pm	(267.8 ± 8.4)	(945.6 ± 104.6)	(1230.1 ± 133.9)	(1661.0 ± 167.4)
Sm	206.3 ± 2.1	(866.1 ± 87.9)	(1121.3 ± 104.6)	(1523.0 ± 129.7)
Eu	177.0 ± 0.8	728.0 ± 50.2	(891.2 ± 96.2)	1355.6 ± 71.1
Gd	398.7 ± 2.1	987.4 ± 41.8	1313.8 ± 71.1	1786.6 ± 71.1
Tb	390.4 ± 2.1	1016.7 ± 50.2	(1351.4 ± 104.6)	1807.5 ± 87.9
Dy	292.9 ± 4.2	(924.7 ± 96.2)	(1192.4 ± 113.0)	(1619.2 ± 138.1)
Ho	302.5 ± 1.3	903.7 ± 58.6	1284.5 ± 104.6	1702.9 ± 108.8
Er	318.4 ± 4.2	(945.6 ± 96.2)	(1225.9 ± 113.0)	(1661.0 ± 138.1)
Tm	233.5 ± 4.2	(828.4 ± 117.2)	(1075.3 ± 133.9)	(1456.0 ± 159.0)
Yb	152.7 ± 0.8	(615.1 ± 117.2)	(795.0 ± 133.9)	(1079.5 ± 159.0)
Lu	427.6 ± 1.7	1112.9 ± 58.6	(1288.7 ± 104.6)	(1748.9 ± 129.7)

B. Polyatomic Oxides

In addition, other gaseous species of the formulas, R_2O, RO_2, and R_2O_2 have appeared at high temperatures but as minor species in the rare earth−oxygen systems. They are ~2 or 3 orders less abundant compared to either the monoxide or the metal atom species. The reports of thermodynamic data for these polyatomic oxides are very limited. The investigation of these polyatomic oxides has been done by Kordis and Gingerich.[217]

The suboxides of the formula, R_2O, have been identified by mass spectrometer in a number of cases. Quantitative data for the following reaction have been drawn:

$$R(g) + RO(g) = R_2O(g)$$

The atomization energies for the $R_2O(g)$ species in addition to $RO_2(g)$ and $R_2O_2(g)$ are shown in Table 15[217] together with data for the heat of sublimation of the rare earth metals.

The dimers of $(RO)_2$ have been identified in a few cases. The enthalpy of formation of the dimers was calculated from the mass spectrometrically determined equilibria of the following reaction:

$$2RO(g) = R_2O_2(g)$$

Most of the rare earth oxides which congruently vaporize are R_2O_3 and evaporation at high temperatures produces other species as shown in the following equation:

$$R_2O_3(s) \rightarrow 2RO(g) + O(g)$$

Under suitable circumstances gaseous species of CeO_2*,[226] PrO_2*, and TbO_2* can be found. (Here, * indicates the same meaning appeared before.) The enthalpy of formation of dioxides, such as CeO_2*, PrO_2*, and TbO_2*, were estimated from vaporization studies of the oxides. The atomization energies are also calculated by the combination of equilibrium data with the corresponding dissociation energy of the monoxide. The gaseous suboxides Y_2O and La_2O and the dimers Y_2O_2 and La_2O_2 appear in the vapor of the metals when contaminated by oxide impurities. The values of the free-energy function are listed in Table 16.[227] The Sc_2O molecule was identified in the system $Sc + Sc_2O_3$.[217]

In addition, Figure 35[228] and Table 17[228] present the standard Gibbs energy of formation of oxides. The data of CaO is also shown in the same figure as a reference. They can be divided into two groups (see Figure 35). The values of $\Delta G°$ is high and negative, and this indicates that the rare earth has a strong affinity to oxygen.[228]

The 5s and 5p orbitals in trivalent rare earth ions are occupied completely by electrons, electrons start to ocuupy 4f orbital with the increase of atomic number of rare earths. The 4f orbital does not affect the chemical bonding because the 4f orbital is highly shielded from 5s and 5d cores. Therefore, lattice energy increases with the decrease of ionic radius of rare earths (Table 18[229]). The characteristics that the hygroscopic properties of yttrium oxide are much less than those of lanthanum oxide are explained by the fact that the lattice energy of Y_2O_3 is considerably

Table 16. Free-Energy Function (in J/mol) (Reprinted with permission from ref 227. Copyright 1965 American Institute of Physics)

T (K)	1700	1900	2100	2300	2500
ScO	250.3	254.1	257.6	260.8	263.9
YO	260.0	263.8	267.3	270.6	273.8
LaO	266.3	270.0	273.5	276.7	280.0
Sc_2O	309.2	315.1	320.5	325.1	329.3
Y_2O	329.7	335.6	341.0	346.0	350.6
La_2O	360.2	366.9	373.2	379.1	384.5
Y_2O_2	366.1	373.6	380.7	387.4	393.7
La_2O_2	379.9	387.4	394.6	401.3	407.5

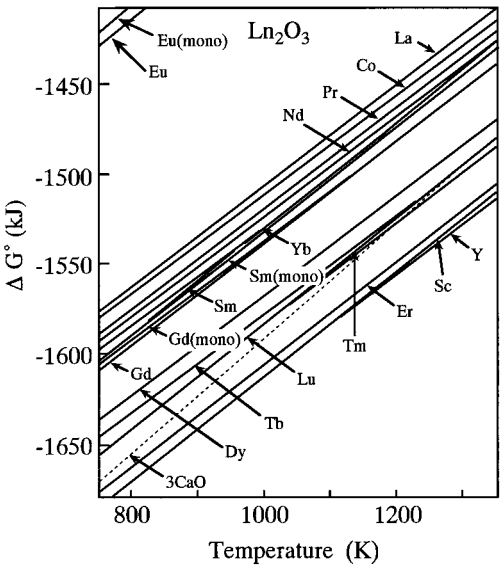

Figure 35. Standard Gibbs energy of formation of oxides. R_2O_3 (R = Sc, Y, and La−Sm) is the hexagonal phase. R_2O_3 (R = Gd−Lu) is in the cubic form. R_2O_3 of R(mono) is in the monoclinic phase. (Reproduced with permission from ref 228. Copyright 1994 The Rare Earth Society of Japan.)

Table 17. Standard Gibbs Energy of Formation of Oxides (kJ/mol) ($2R + {}^3/_2O_2 = R_2O_3$)[a] (Reprinted with permission from ref 228. Copyright 1994 The Rare Earth Society of Japan)

R_2O_3	$\Delta G°$
Sc_2O_3	$-1900.682 + (0.286980)T$
Y_2O_3	$-1895.364 + (0.280708)T$
La_2O_3	$-1784.833 + (0.277235)T$
Ce_2O_3*	$-1784.039 + (0.271337)T$
Pr_2O_3*	$-1798.608 + (0.277618)T$
Nd_2O_3	$-1798.769 + (0273770)T$
Sm_2O_3	$-1822.276 + (0.291154)T$
Sm_2O_3 (mono)	
(800−1195 K)	$-1819.144 + (0.286101)T$
(1195−1300 K)	$-1823.361 + (0.289615)T$
Gd_2O_3 (mono)	$-1811.372 + (0.273474)T$
Gd_2O_3	$-1817.050 + (0.27451)T$
Tb_2O_3*	$-1850.179 + (0.271433)T$
Dy_2O_3	$-1842.268 + (0.273484)T$
Er_2O_3	$-1886.931 + (0.279982)T$
Tm_2O_3	$-1873.275 + (0.288950)T$
Yb_2O_3	$-1807.859 + (0.277997)T$
Lu_2O_3	$-1867.169 + (0.281631)T$

[a] In Ln_2O_3*, the O/Ln ratio is thought to be almost equal to 1.5.

Table 18. Lattice Energy of Rare Earth Sesquioxides (Reprinted with permission from ref 229. Copyright 1976 American Chemical Society)

rare earths	lattice energy (kJ/mol)
Y	−13428
La	−12687
Ce	−12901
Pr	−12938
Nd	−13008
Pm	−13114
Sm	−13181
Eu	−13271
Gd	−13330
Tb	−13434
Dy	−13514
Ho	−13588
Er	−13665
Tm	−13744
Yb	−13814
Lu	−13871

large and form a rigid crystal to exhibit less reactivity with water.

VIII. Concluding Remarks

The binary rare earth oxides have refractory characteristics and have been utilized in various fields. As a result of the presence of impurities in the oxides studied in some earlier work, this has led to erroneous determinations of structure and polymorphism. However, due to technological advances, high-purity rare earth oxides can now be easily obtained for higher reliability studies. In addition to the study of phase stability of the rare earth oxides by elemental analyses and conventional methods such as electrical, magnetic, and optical techniques, high-resolution electron microscopy (HREM) has increasingly become a useful in situ tool to identify phenomena occurring with these materials. Also, progress has been made in the successful calculation of band structure, and the development of preparation techniques for ultrafine particles. With the aid of HREM and of calculation from the experimental and theoretical viewpoints, respectively, the understanding of the unique characteristics of binary rare earth oxides can now proceed further. From a practical aspect, the application of the properties of ultrafine particles opens up promising areas which could not be addressed previously with the use of conventional particles of the type obtained during that earlier period. The review presented here will contribute not only to a further understanding of the recently reported characteristics of the binary rare earth oxides but also to providing an additional basis to the comprehensive chemistry of the rare earth oxides.

IX. Acknowledgments

Authors thank Dr. M. Post, Institute for Environmental Science, National Research Council of Canada for prereviewing the article. We would like to express our thanks to Professor L. Eyring, Department of Chemistry, and Center for Solid State Science, Arizona State University for providing us papers and review articles which contributed greatly to the preparation of this review.

X. References

(1) Eyring, L. *Synthesis of Lanthanide and Actinide Compound*; Kluwer Academic Publisher: Netherland, 1991; p 187.
(2) Schweda, E. *Diffusionless phase transition and Related Structures in Oxide*; Trans Tech Publication: Switzerland, 1992; Vol. 68, p 187.
(3) Morss, L. R. *Handbook on the Physics and Chemistry of Rare Earths*; North-Holland: Amsterdam, 1994; Vol. 18, p 239.
(4) *Gmelin Handbuch der Anorganischen Chemie, Seltenerdelemente*; Springer-Verlag: Berlin, 1974; Teil C1, p 85.
(5) Eyring, L. *Science and Technology of Rare Earth Materials*; Academic Press Inc: New York, 1980; p 99.
(6) Eyring, L. *Handbook on the Physics and Chemistry of Rare Earths*; North-Holland: Amsterdam, 1979; Vol.3, p 337.
(7) Haschke, J. M.; Eick, H. A. *J. Phys. Chem.* **1968**, *72*, 4235.
(8) Bedford, R. G.; Catalano, E. *J. Solid State Chem.* **1971**, *3*, 112.
(9) Brauer, G. *Progress in the Science and Technology of the Rare Earths*; Pergamon Press: Oxford, 1966; Vol. 2, p 312.
(10) Bernal, S.; Botana, F. J.; García, R.; Rodríguez-Izquierdo, J. M. *React. Solids* **1987**, *4*, 23.
(11) Brauer, G.; Pfeiffer, B. *J. Less-Common Met.* **1963**, *5*, 171.
(12) Clifford, A. F. *Rare Earth Research II*; Gordon and Breach: New York 1964; p 45.
(13) Sastry, R. L. N.; Mehrotra, P. N.; Rao, C. N. R. *J. Inorg. Nucl. Chem.* **1966**, *28*, 2167.
(14) Coutures, J.-P.; Verges, R.; Foëx, M. *Rev. Int. Hautes Temp. Réfract.* **1975**, *12*, 181.
(15) Haire, R. G.; Eyring, L. *Handbook on the Physics and Chemistry of Rare Earths*; North-Holland: Amsterdam, 1994; Vol. 18, p 413.
(16) Eyring, L.; Holmberg, B. *Advances in Chemistry Series*; American Chemical Society: Washington, DC, 1963; Vol. 39, p 46.
(17) Templeton, D. H.; Dauben, C. H. *J. Am. Chem. Soc.* **1954**, *76*, 5237.
(18) Barbezat, S.; Loriers, J. *C. R. Acad. Sci.* **1952**, *245*, 1978.
(19) Stecura, S.; Campbell, W. J. *Bur. Mines Rep. Invest.* **1961**, No. 5847.
(20) Caro, P. E. *J. Less-Common Met.* **1968**, *16*, 367.
(21) Sanderson, R. T. *Chemical Bonds and Bond Energy*; Academic Press: New York, 1971; p 120.
(22) Van Vleck, J. H. *Rare Earth Research III*; Gordon and Breach: New York, 1965; p 3.
(23) Van Vleck, J. H. *Progress in the Science and Technology of the Rare Earths*; Pergamon Press: Oxford, 1966; Vol. 2, p 1.
(24) Haschke, J. M.; Eick, H. A. *Inorg. Chem.* **1970**, *9*, 851.
(25) Fishel, N. A.; Haschke, J. M.; Eick, H. A. *Inorg. Chem.* **1970**, *9*, 413.
(26) Leger, J. M.; Yacoubi, N.; Loriers, J. *J. Solid State Chem.* **1981**, *36*, 261.
(27) Shafer, M. W.; Torrance, J. B.; Penney, T. *J. Phys. Chem. Solids* **1972**, *33*, 2251.
(28) Wachter, P. *Handbook on the Physics and Chemistry of Rare Earths*; North-Holland: Amsterdam, 1979; Vol. 2, 507.
(29) Bärnighausen, H.; Brauer, G. *Acta Crystallogr.* **1962**, *15*, 1059.
(30) Rau, R. C. *Acta Crystallogr.* **1966**, *20*, 716.
(31) McCarthy, G. J.; White, W. B. *J. Less-Common Met.* **1970**, *22*, 409.
(32) Felmlee, T. L.; Eyring, L. *Inorg. Chem.* **1968**, *7*, 660.
(33) Soloveva, A. E. *Izv. Akad. Nauk. SSSR, Neorg. Mater.* **1985**, *21*, 808.
(34) Husson, E.; Proust, C. *Mater. Res. Bull.* **1995**, *30*, 135.
(35) Foëx, M.; Traverse, J. P. *Rev. Int. Hautes Temp. Réfract.* **1966**, *3*, 429.
(36) Chikalla, T. D.; McNeilly, C. E.; Roberts, F. P. *J. Am. Ceram. Soc.* **1972**, *55*, 428.
(37) Goldschmidt, V. M.; Ulrich, F.; Barth, T. *Mater. Naturv.* **1925**, *Kl*, 5.
(38) Ross, W. A.; Gibby, R. L. *J. Am. Ceram. Soc.* **1974**, *57*, 46.
(39) Weigel, V. F.; Scherer, V. *Radiochim. Acta* **1965**, *4*, 197.
(40) Pauling, L. *Z. Krystallogr.* **1928**, *69*, 415.
(41) Koehler, W. C.; Wollan, E. O. *Acta Crystallogr.* **1953**, *6*, 741.
(42) Müller-Buschbaum, H.; Schnering, H. G. *Z. Anorg. Allg. Chem.* **1965**, *340*, 232.
(43) Müller-Buschbaum, H. *Z. Anorg. Allg. Chem.* **1966**, *343*, 6.
(44) Douglass, R. M.; Staritzky, E. *Anal. Chem.* **1956**, *28*, 552.
(45) Cromer, D. T. *J. Phys. Chem.* **1957**, *61*, 753.
(46) Pauling, L.; Shappell, M. D. *Z. Kristallogr.* **1930**, *75*, 128.
(47) Boulesteix, C. *Handbook on the Physics and Chemistry of Rare Earths*; North-Holland: Amsterdam, 1982; Vol. 5, p 321.
(48) Miller, A. E.; Daane, A. H. *J. Inorg. Nucl. Chem.* **1965**, *27*, 1955.
(49) Sata, T.; Yoshimura, M. *Bull. Tokyo Inst. Technol.* **1968**, *84*, 13.
(50) Sata, T.; Yoshimura, M. *J. Ceram. Assoc. Jpn.* **1968**, *76*, 116.
(51) Brauer, G.; Holtschmidt, U. *Z. Anog. Allg. Chem.* **1951**, *265*, 105.
(52) Ray, S. P.; Cox, D. E. *J. Solid State Chem.* **1975**, *15*, 333.
(53) Ricken, M.; Nölting, J.; Riess, I. *J. Solid State Chem.* **1984**, *54*, 89.

(54) Riess, I.; Ricken, M.; Nölting, J. *J. Solid State Chem.* **1985**, *57*, 314.
(55) Körner, R.; Ricken, M.; Nölting, J.; Riess, I. *J. Solid State Chem.* **1989**, *78*, 136.
(56) Knappe, P.; Eyring, L. *J. Solid State Chem.* **1985**, *58*, 312.
(57) Kang, Z. C.; Zhang, J.; Eyring, L. *Aust. J. Chem.* **1992**, *45*, 1499.
(58) Eyring, L.; Kang, Z. C. *Eur. J. Solid State Inorg. Chem.* **1991**, *28*, 459.
(59) Sawyer, J. O.; Hyde, B. G.; Eyring, L. *Inorg. Chem.* **1965**, *4*, 426.
(60) Hoekstra, H. R.; Gingerich, K. A. *Science* **1964**, *146*, 1163.
(61) Hoekstra, H. R. *Inorg. Chem.* **1966**, *5*, 754.
(62) Ainscough, J. B.; Moore, D. A.; Osborn, S. C. *J. Nucl. Mater.* **1975**, *55*, 229.
(63) Kang, Z. C.; Eyring, L. *J. Alloys Compd.* **1997**, *249*, 206.
(64) Kang, Z. C., Zhang, J.; Eyring, L. *Z. Anorg. Allg. Chem.* **1966**, *622*, 465.
(65) Kang, Z. C.; Eyring, L. *Aust. J. Chem.* **1997**, *49*, 981.
(66) Kang, Z. C.; Eyring, L. *J. Alloys Compd.* **1998**, in press.
(67) Hoskins, B. F.; Martin, R. L. *Aust. J. Chem.* **1995**, *48*, 709.
(68) Zhang, J.; Kang, Z. C.; Eyring, L. *J. Alloys Compd.* **1993**, *192*, 57.
(69) Eyring, L. *Advances in Chemistry Series*; American Chemical Society: Washington, DC, 1967; p 67.
(70) Turcotte, R. P.; Warmkessel, J. M.; Tilley, R. J. D.; Eyring, L. *J. Solid State Chem.* **1971**, *3*, 265.
(71) Hyde, B. G.; Bevan, D. J. M.; Eyring, L. *Philos. Trans. R. Soc. London Ser. A* **1966**, No1106, *259*, 583.
(72) Sawyer, J. O.; Hyde, B. G.; Eyring, L. *Bull. Soc. Chim. France* **1965**, 1190.
(73) Zhang, J.; Von Dreele, R. B.; Eyring, L. *J. Solid State Chem.* **1995**, *118*, 133.
(74) Zhang, J.; Von Dreele, R. B.; Eyring, L. *J. Solid State Chem.* **1995**, *118*, 141.
(75) Zhang, J.; Von Dreele, R. B.; Eyring, L. *J. Solid State Chem.* **1996**, *122*, 53.
(76) Haschke, J. M.; Eyring, L. *Inorg. Chem.* **1971**, *10*, 2267.
(77) Von Dreele, R. B.; Eyring, L.; Bowman, A. L.; Yarnell, J. L. *Acta Crystallogr.* **1975**, *B31*, 971.
(78) Eyring, L. *Nonstoichiometric Oxides*; Academic Press: New York, 1981; p 337.
(79) Kang, Z. C.; Eyring, L. *J. Solid State Chem.* **1988**, *75*, 52.
(80) Bartram, S. F. *Inorg. Chem.* **1966**, *5*, 749.
(81) Jenkins, M. S.; Turcotte, R. P.; Eyring, L. *The chemistry of extended defects in nonmetallic solids*; North-Holland Publishing Company: Amsterdam, 1970; p 36.
(82) Lincoln, F. J.; Sellar, J. R.; Hyde, B. G. *J. Solid State Chem.* **1988**, *74*, 268.
(83) Guth, E. D.; Eyring, L. *J. Am. Chem. Soc.* **1954**, *76*, 5242.
(84) Simon, W.; Eyring, L. *J. Am. Chem. Soc.* **1954**, *76*, 5872.
(85) Baenziger, N. C.; Eick, H. A.; Schuldt, H. S.; Eying, L. *J. Am. Chem. Soc.* **1961**, *83*, 2219.
(86) Hyde, B. G.; Eyring, L. *Rare Earth Research III*; Gordon and Breach: New York, 1965; p 623.
(87) Kordis, J.; Eyring, L. *J. Phys. Chem.* **1968**, *72*, 2044.
(88) Burnham, D. A.; Eyring, L.; Kordis, J. *J. Phys. Chem.* **1968**, *72*, 4424.
(89) Wilbert, Y.; Marion, F. *C. R. Acad. Sci.* **1970**, *C271*, 736.
(90) Zhang, J.; Von Dreele, R. B.; Eyring, L. *J. Solid State Chem.* **1993**, *104*, 21.
(91) Foex, M. *Z. Anorg. Allg. Chem.* **1965**, *337*, 313.
(92) Aldebert, P.; Traverse, J. P. *Mater. Res. Bull.* **1979**,*14*, 303.
(93) Eyring, L. *Progress in the Science and Technology of the Rare Earths*; Pergamon Press: Oxford, 1968; Vol.3, p 434.
(94) Inaba, H.; Pack, S. P.; Lin, S. H.; Eyring, L. *J. Solid State Chem.* **1980**, *33*, 295.
(95) Inaba, H.; Lin, S. H.; Eyring, L. *J. Solid State Chem.* **1981**, *37*, 58.
(96) Sugihara, T.; Lin, S. H.; Eyring, L. *J. Solid State Chem.* **1981**, *40*, 226.
(97) Sugihara, T.; Lin, S. H.; Eyring, L. *J. Solid State Chem.* **1981**, *40*, 189.
(98) Inaba, H.; Navrotsky, A.; Eyring, L. *J. Solid State Chem.* **1981**, *37*, 67.
(99) Inaba, H.; Navrotsky, A.; Eyring, L. *J. Solid State Chem.* **1981**, *37*, 77.
(100) Knittel, D. R.; Pack, S. P.; Lin, S. H.; Eyring, L. *J. Chem. Phys.* **1977**, *67*, 134.
(101) Eyring, L. *Advances in Chemistry Series*; American Chemical Society: Washington, DC, 1980; p 27.
(102) Eyring, L. *High-resolution transmission electron microscopy & assoc. Techniques*; Oxford University Press: New York, 1988; p 378.
(103) Kang, Z. C.; Eyring, L. *J. Solid State Chem.* **1988**, *75*, 60.
(104) Schweda, E.; Kang, Z. C.; Eyring, L. *J. Microsc.* **1987**, *145*, 45.
(105) Kang, Z. C.; Eyring, L.; Smith, D. J. *Ultramicroscopy* **1987**, *22*, 71.
(106) Kang, Z. C.; Eyring, L. *J. Alloys Compd.* **1992**, *181*, 483.
(107) Eyring, L. *High Temp. Sci.* **1985**, *20*, 183.
(108) Eyring, L. *J. Chem. Educ.* **1980**, *57*, 565.
(109) Gasgnier, M.; Schiffmacher, G.; Eyring, L.; Caro, P. *J. Less-Common Met.* **1987**, *127* 167.
(110) Eick, H. A.; Eyring, L.; Summerville, E.; Tuenge, R. T. *J. Solid State Chem.* **1982**, *42*, 47.
(111) Eyring, L. *J. Alloys Compd.* **1994**, *207/208*, 1.
(112) Kang, Z. C.; Smith, D. J.; Eyring, L. *Surf. Sci.* **1986**, *175*, 684.
(113) Kang, Z. C.; Boulesteix, C.; Eyring, L. *J. Solid State Chem.* **1989**, *81*, 96.
(114) Tong, J.; Eyring, L. *J. Alloys Compd.* **1995**, *225*, 139.
(115) Kang, Z. C.; Eyring, L. *J. Alloys Compd.* **1995**, *225*, 190.
(116) Kang, Z. C.; Eyring, L. *J. Solid State Chem.* **1990**, *88*, 303.
(117) Pyykkö, P. *Inorg. Chim. Acta* **1987**, *139*, 243.
(118) Dolg, M.; Stoll, H. *Handbook on the Physics and Chemistry of Rare Earths*; North-Holland: Amsterdam, 1996; Vol. 22, p 607.
(119) Balasubramanian, K. *Handbook on the Physics and Chemistry of Rare Earths*; North-Holland: Amsterdam, 1994; Vol. 18, p 29.
(120) Carette, P.; Hocquet, A. *J. Mol. Spectrosc.* **1988**, *131*, 301.
(121) Field, R. W. *Ber. Bunsen-Ges. Phys. Chem.* **1982**, *86*, 771.
(122) Wang, S. G.; Schwarz, W. H. E. *J. Phys. Chem.* **1995**, *99*, 11687.
(123) Wang, S. G.; Pan, D. K.; Schwarz, W. H. E. *J. Chem. Phys.* **1995**, *102*, 9296.
(124) Dolg, M.; Stoll, H.; Flad, H.-J.; Preuss, H. *J. Chem. Phys.* **1992**, *97*, 1162.
(125) Evarestov, R. A.; Leko, A. V.; Murin, I. V.; Petrov, A. V.; Veryazov, V. A. *Phys. Status Solidi B* **1992**, *170*, 145.
(126) Nakano, T.; Kotani, A.; Parlebas, J. C. *J. Phys. Soc. Jpn.* **1987**, *56*, 2201.
(127) Kotani, A.; Ogasawara, H. *J. Electron Spectrosc. Related Phenom.* **1992**, *60*, 257.
(128) Hill, S. E.; Catlow, C. R. A. *J. Phys. Chem. Solids* **1993**, *54*, 411.
(129) López-Aguilar, F.; Costa-Quintana, J. *Phys. Status Solidi B* **1983**, *118*, 779.
(130) De, S. K.; Chatterjee, S. *J. Phys.: Condens. Matter* **1989**, *1*, 1169.
(131) Nakamatsu, H.; Mukoyama, T.; Adachi, H. *Chem. Phys. Lett.* **1995**, *247*, 168.
(132) Prokofiev, A. V.; Shelykh, A. I.; Melekh, B. T. *J. Alloys Compd.* **1996**, *242*, 41.
(133) Rao, G. V. S.; Ramdas, S.; Mehrotra, P. N.; Rao, C. N. R. *J. Solid State Chem.* **1970**, *2*, 377.
(134) Lau, K. H.; Fox, D. L.; Lin, S. H.; Eyring, L. *High Temp. Sci.* **1976**, *8*, 129.
(135) Honig, J. M.; Cella, A. A.; Cornwell, J. C. *Rare Earth Research*; Gordon and Breach: New York, 1964; p 555.
(136) Chandrashekhar, G. V.; Mehrotra, P. N.; Rao, G. V. S.; Subbarao, E. C.; Rao, C. N. R. *Trans. Faraday Soc.* **1967**, *63*, 1295.
(137) Arakawa, T.; Kabumoto, A.; Shiokawa, J. *J. Less-Common Met.* **1986**, *115*, 281.
(138) Pike, G. E. *Phys. Rev. B* **1972**, *6*, 1572.
(139) Gasgnier, M. *Phys. Status Solidi A* **1980**, *57*, 11.
(140) Dakhel, A. A. *Phys. Status Solidi A* **1995**, *147*, K79.
(141) Koleshko, V. M.; Babushkina, N. V. *Thin Solid Films* **1979**, *62*, 1.
(142) Dutta, C. R.; Barua, K. *Thin Solid Films* **1983**, *104*, L69.
(143) Tare, V. B.; Schmalzried, H. *Z. Phys. Chem. (NF)* **1964**, *43*, 30.
(144) Eyring, L. *High Temp. Oxides* **1970**, *2*, 41.
(145) Goswami, A.; Varma, R. R. *Thin Solid Films* **1975**, *28*, 157.
(146) Mitra, N. C.; Bhattacharyya, A. L. *Phys. Status Solidi A* **1985**, *90*, 301.
(147) Mitra, N. C.; Bhattacharyya, A. L. *Phys. Status Solidi A* **1985**, *88*, 175.
(148) Wiktorczyk, T.; Wesolowska, C. *Thin Solid Films* **1980**, *71*, 15.
(149) Wiktorczyk, T.; Wesolowska, C. *Vacuum* **1987**, *37*, 107.
(150) Dutta, C. R.; Barua, K. *Thin Solid Films* **1983**, *100*, 149.
(151) Dharmadhikari, V. S.; Goswami, A. *Thin Solid Films* **1982**, *87*, 119.
(152) Krill, G.; Ravet, M. F.; Kappler, J. P.; Abadli, L.; Leger, J. M.; Yacoubi, N.; Loriers, C. *Solid State Commun.* **1980**, *33*, 351.
(153) Matthias, B. T.; Bozorth, R. M. *Phys. Rev. Lett.* **1961**, *7*, 160.
(154) Wang, F. F. Y. *Phys. Status Solidi* **1966**, *14*, 189.
(155) Kern, S. *J. Chem. Phys.* **1964**, *40*, 208.
(156) MacChesney, J. B.; Williams, H. J.; Sherwood, R. C.; Potter, J. F. *J. Chem. Phys.* **1964**, *41*, 3177.
(157) MacChesney, J. B.; Williams, H. J.; Sherwood, R. C.; Potter, J. F. *J. Chem. Phys.* **1966**, *44*, 596.
(158) Bertaut, E. F.; Chevalier, R. *C. R. Acad. Sci., Paris, Ser. B* **1966**, *262*, 1707.
(159) Moon, R. M.; Koehler, W. C.; Child, H. R.; Raubenheimer, L. J. *Phys. Rev.* **1968**, *176*, 722.
(160) Röhler, J. *Handbook on the Physics and Chemistry of Rare Earths*; North-Holland: Amsterdam, 1987; Vol. 10, p 453.
(161) Warmkessel, J. M.; Lin, S. H.; Eyring. L. *Inorg. Chem.* **1969**, *8*, 875.
(162) White, W. B. *Appl. Spectrosc.* **1967**, *21*, 167.
(163) Haensel, R.; Rabe, P.; Sonntag, B. *Solid State Commun.* **1970**, *8*, 1845.
(164) Goswami, A.; Goswami, A. P. *Thin Solid Films* **1975**, *27*, 123.
(165) Schoonover, J. R.; Lee, Y.-L.; Su, S. N.; Lin, S. H.; Eyring, L. *Appl. Spectrosc.* **1984**, *38*, 154.

(166) Tucker, L. A.; Carney, Jr. F. J.; McMillan, P.; Lin, S. H.; Eyring, L. *Appl. Spectrosc.* **1984**, *38*, 857.
(167) Millot, F.; Mierry, P. de. *J. Phys. Chem. Solids* **1985**, *46*, 797.
(168) Eyring, L. *Heterogeneous Kinetics at Elevated Temperatures*; Plenum Press: 1970; p 343.
(169) Eyring, L. *Solid State Chemistry*; Maicell Dekku: New York, 1974; p 565.
(170) McKelvy, M.: Eyring, L. *J. Crystal Growth* **1983**, *62*, 635.
(171) Lowenstein, M. Z.; Kihlborg, L.; Lau, K. H.; Haschke, J. M.; Eyring, L. *NBS Spec. Publ. (U.S.)* **1972**, *364*, 343.
(172) Finch, C. B.; Clark, G. W. *J. Appl. Phys.* **1966**, *37*, 3910.
(173) Linares, R. C. *J. Phys. Chem. Solids* **1967**, *28*, 1285.
(174) MacChesney, J. B.; Williams, H. J.; Sherwood, R. C.; Potter, J. F. *J. Chem. Phys.* **1966**, *44*, 596.
(175) Guerci, C. F.; Shafer, M. W. *J. Appl. Phys.* **1966**, *37*, 1406.
(176) Brissette, L. A.; Burnett, P. L.; Spriggs, R. M.; Vasilos, T. *J. Am. Ceram. Soc.* **1966**, *49*, 165.
(177) Lefever, R. A.; Matsko, J. *Mater. Res. Bull.* **1967**, *2*, 865.
(178) Gazza, G. E.; Roderick, D.; Levine, B. *J. Mater. Sci. Lett.* **1971**, *6*, 1137.
(179) Dutta, S. K.; Gazza, G. E. *Mater. Res. Bull.* **1969**, *4*, 791.
(180) Ploetz, G. L.; Krystyniak, C. W.; Dumas, H. E. *J. Am. Ceram. Soc.* **1958**, *41*, 551.
(181) Matijevic, E.; Hsu, W. P. *J. Colloid Interface Sci.* **1987**, *118*, 506.
(182) Minagawa, Y.; Yajima, F. *Bull. Chem. Soc. Jpn.* **1990**, *63*, 378.
(183) Minagawa, Y.; Yajima, F. *Bull. Chem. Soc. Jpn.* **1990**, *63*, 2115.
(184) Hsu, W. P.; Ronnquist, L.; Matijevic, E. *Langmuir* **1988**, *4*, 31.
(185) Aiken, B.; Hsu, W. P.; Matijevic, E. *J. Am. Ceram. Soc.* **1988**, *71*, 845.
(186) Skandan, G.; Hahn, H.; Parker, J. C. *Scr. Metall. Mater.* **1991**, *25*, 2389.
(187) Chang, W.; Cosandey, F.; Hahn, H. *Nanostruct. Mater.* **1993**, *2*, 29.
(188) Skandan, G.; Foster, C. M.; Frase, H.; Ali, M. N.; Parker, J. C.; Hahn, H. *Nanostruct. Mater.* **1992**, *1*, 313.
(189) Zhang, Z. K.; Cui, Z. L. *Nanostruct. Mater.* **1994**, *4*, 823.
(190) Tschöpe, A.; Ying, J. Y. *NATO, ASI. Ser. E.* **1994**, *260*, 781.
(191) Mani, T. V.; Varma, H. K.; Damodaran, A. D.; Warrier, K. G. K. *Ceram. Int.* **1993**, *19*, 125.
(192) Chu, X.; Chung, W.; Schmidt, L. D. *J. Am. Ceram. Soc.* **1993**, *76*, 2115.
(193) Varma, H. K.; Mukundan, P.; Warrier, K. G. K.; Damodaran, A. D. *J. Mater. Sci. Lett.* **1990**, *9*, 377.
(194) Varma, H. K.; Mukundan, P.; Warrier, K. G. K.; Damodaran, A. D. *J. Mater. Sci. Lett.* **1991**, *10*, 666.
(195) Sekar, M. M. A.; Manoharan, S. S.; Patil, K. C. *J. Mater. Sci. Lett.* **1990**, *9*, 1205.
(196) Suzuki, M.; Kagawa, M.; Syono, Y.; Hirai, T. *Ceram. Trans.* **1991**, *22*, 147.
(197) Suzuki, M.; Kagawa, M.; Syono, Y.; Hirai, T. *J. Mater. Sci.* **1992**, *27*, 679.
(198) Chen, P.-L.; Chen, I.-W. *J. Am. Ceram. Soc.* **1993**, *76*, 1577.
(199) Nabavi, M.; Spalla, O.; Cabane, B. *J. Colloid Interface Sci.* **1993**, *160*, 459.
(200) Zhou, Y. C.; Rahaman, M. N. *J. Mater. Res.* **1993**, *8*, 1680.
(201) Imoto, F.; Nanataki, T.; Kaneko, S. *Ceram. Trans.* **1988**, *1*, 204.
(202) Xie, C. Y.; Li, S. Z.; Li, J. *Chin. Chem. Lett.* **1992**, *3*, 951.
(203) Kobayashi, M. *J. Mater. Sci. Lett.* **1992**, *11*, 767.
(204) Lequitte, M.; Autissier, D. *Nanostruct. Mater.* **1995**, *6*, 333.
(205) Masui, T.; Machida, K.; Sakata, T.; Mori, H.; Adachi, G. *Chem. Lett.* **1996**, 75.
(206) Masui, T.; Machida, K.; Sakata, T.; Mori, H.; Adachi, G. *J. Alloys Compd.* **1997**, *256*, 97.
(207) Eicke, H. F.; Shepherd, J. C. W.; Sternemann, A. *J. Colloid Interface Sci.* **1976**, *56*, 168.
(208) Atic, S. S.; Thomas, J. K. *J. Am. Chem. Soc.* **1981**, *103*, 3543.
(209) Fletcher, P. D. I.; Howe, A. M.; Robinson, B. H. *J. Chem. Soc., Faraday Trans. 1* **1987**, *83*, 985.
(210) Lang, J.; Jada, A.; Malliaris, A. *J. Phys. Chem.* **1988**, *92*, 1946.
(211) López-Quintela, M. A.; Rivas, J. *J. Colloid Interface Sci.* **1993**, *158*, 446.
(212) Masui, T.; Fujiwara, K.; Machida, K.; Sakata, T.; Mori, H.; Adachi, G. *Chem. Mater.* **1997**, *9*, 2197.
(213) Chandrasekharaiah, M. S.; Gingerich, K. A. *Handbook on the Physics and Chemistry of Rare Earths*; North-Holland: Amsterdam, 1989; Vol. 12, p 409.
(214) Pedley, J. B.; Marshall, E. M. *J. Phys., Chem. Ref. Data* **1983**, *12*, 967.
(215) Gingerich, K. A. *Current Topics in Materials Science*; North-Holland: Amsterdam, 1980; Vol. 6, Chapter 5, p 345.
(216) White, D.; Walsh, P. N.; Ames, L. L.; Goldstein, H. W. *Thermodyn. Nucl. Mater. Proc. Symp. 1962 (Vienna)* **1962**, 417.
(217) Kordis, J.; Gingerich, K. A. *J. Chem. Phys.* **1977**, *66*, 483.
(218) Gschneidner, K. A., Jr.; Kippenhan, N. A.; McMasters, O. D. *Report IS-RIC-6*; Rare Earth Information Center: Ames, 1973; p 1.
(219) Morss, L. R. *J. Less-Common Met.* **1983**, *93*, 301.
(220) Rard, J. A. *Chem. Rev.* **1985**, *85*, 555.
(221) Lavut, E. G.; Chelovskaya, N. V. *J. Chem. Thermodyn.* **1990**, *22*, 817.
(222) Murad, E.; Hildenbrand, D. L. *J. Chem. Phys.* **1980**, *73*, 4005.
(223) Ames, L. L.; Walsh, P. N.; White, D. *J. Phys. Chem.* **1967**, *71*, 2707.
(224) Ackermann, R. J.; Chandrasekharaiah, M. S. *Thermodyn. Nucl. Mater.* **1974**, *2*, 3.
(225) Ackermann, R. J.; Rauh, E. G.; Thorn, R. J. *J. Chem. Phys.* **1976**, *65*, 1027.
(226) Ackermann, R. J.; Rauh, E. G. *J. Chem. Thermodyn.* **1971**, *3*, 609.
(227) Smoes, S.; Drowart, J.; Verhaegen, G. *J. Chem. Phys.* **1965**, *43*, 732.
(228) Katayama, I.; Maki, K.; Iida, T. *Kidorui* **1994**, *25*, 19.
(229) Morss, L. S. *Chem. Rev.* **1976**, *76*, 827.

CR940055H